2017

Direct Numerical Simulation of Rayleigh-Bénard Convection of Two Immiscible Fluids-Level Set Method

Haolin Ma
Lehigh University

Recommended Citation

Ma, Haolin, "Direct Numerical Simulation of Rayleigh-Bénard Convection of Two Immiscible Fluids-Level Set Method" (2017). *Theses and Dissertations*. 2954.
https://preserve.lehigh.edu/etd/2954

Direct Numerical Simulation of Rayleigh-Bénard Convection of Two Immiscible Fluids-Level Set Method

by

Haolin Ma

A Dissertation

Presented to the Graduate and Research Committee

of Lehigh University

in Candidacy for the Degree of

Doctor of Philosophy

in

Mechanical Engineering

Lehigh University

August 2017

Approved and recommended for acceptance as a dissertation in partial fulfillment of the requirements for the degree of Doctor of Philosophy

Haolin Ma

Direct Numerical Simulation of Rayleigh-Bénard Convection of Two Immiscible Fluids-Level Set Method

Defense Date

Dissertation Director
(**Must Sign with Blue Ink**)

Approved Date

Committee Members:

Alparslan Oztekin

Jacob Kazakia

Yaling Liu

Yue Yu

ACKNOWLEDGMENTS

There are many people whom I would like to acknowledge for their help and support as I made my way through this thesis work. Dr. Alparslan Oztekin, my advisor, deserves much credit for the genesis of my research project. Alp's extraordinary research experience helped me broaden my academic horizon. Alp has always given me the ultimate freedom to let me choose the project I am interested in most. This has proved to be an invaluable experience to me in developing my research interest. Alp was also very generous with his time and helpful comments about this thesis. I also wish to thank Dr. Jacob Kazakia, Dr. Yaling Liu and Dr. Yue Yu for serving as committee members for this dissertation and Dr. Yue Yu also for her help in part of the mathematical modelling.

Many of the friends I made at Lehigh were helpful in getting through some of the emotional moments. Guosong was a close friend as well as a good roommate. I-Han, Yang and Wei also became good friends and made showing up at the office each day a little more fun. Also, these friends were a great help when it came to discussing research issues.

Although unsure of what I was really doing, my parents back home, Mr. Jianwei Ma and Mrs. Dongying Ma were always very supportive. A special thanks to my wife, Ms. Tingting Li, who quit her job in China and moved to Lehigh accompanying me and the birth and growing up of Catharine made the life splendid. My time of living in Lehigh has been full of memorable experiences.

TABLE OF CONTENTS

LIST OF TABLES

LIST OF FIGURES

ABSTRACT

A finite volume numerical method is introduced to perform the direct numerical simulation for two-phase immiscible and incompressible fluids. The Navier-Stokes equation is discretized by the staggered mesh spatially and advected temporally with the 4th order Runge-Kutta scheme. CFL conditions involving the effect from the convective term, viscous term, stiff source term and heat transfer are applied to meet the stringent limitation on the time step. Energy equation is coupled with the Navier-Stokes equation when the study of heat transfer is included. The interface separating the fluids is treated implicitly using a finite thickness, which constrained the numerical instabilities within the interface, by the level set method. The topology change and location of the interface are captured by advecting the smooth level set function with the 5th order WENO algorithm. Re-initialization of the signed distance function is executed at the designated time steps to ensure the mass conservation. The surface tension effect is modelled with the Continuum Surface Force (CSF) model and the numerical spurious error is corrected by the modified curvature calculation. The validated method is used to study the dynamics of single and multiple bubble/droplet movements influenced by different viscosity, density ratio and surface tension effect. The application of this method is further extended to investigate the binary Rayleigh-Bénard convection in two-dimensional and three-dimensional geometries. The complex nonequilibrium of the system is well captured and compared with the linear stability analysis. Discussion and explanation for the driving mechanism and pattern of energy transportation of the two-phase Rayleigh-Bénard convection are presented with the predicted results.

Chapter 1

Introduction

1.1 Motivation

In nature, flows of multiple components or multiple phases are very common. Rayleigh-Bénard convection of layered multiple fluids occurs often in vitally important systems. The earth mantel movement and the cloud formation are two significant examples of Rayleigh-Bénard system. The major feature of the dynamics in the system is the convective flow induced by density stratification and the quest for the understanding of this flow pattern has motivated a large body of experimental, numerical and theoretical investigations. When a sufficiently large temperature gradient is applied cross a fluid layer at rest, the onset of the convective motion can occur. After Bénard's first quantitative experiment [1] and Lord Rayleigh's linear stability analysis[2] studying this phenomenon, several investigators have focused on the study of a single layer Rayleigh-Bénard system. Numerical studies of Rayleigh-Bénard convection in the system with the boundary of stress free surface ignore the presence of air layer. Although most of the researches achieved good agreements between the numerical studies and experimental studies of Rayleigh Benard problem with a free surface, the dynamics and characteristics in the ignored air layer are not explored. In this study Rayleigh-Bénard convection of air and liquid is considered. For the binary system with an air layer, large ratios in density and viscosity across the interface would lead to a numerical instability. A numerical method, which can deal with steep gradients in the physical properties, is needed.

1.2 Literature review

For multiphase flows of immiscible fluids, fluids are separated by a sharp interface where discontinuity on material properties occurs. For multiphase Rayleigh-Bénard convection problems, we consider two immiscible fluids and hence density, viscosity, thermal conductivity across the interface become discontinuous. Discontinuities cannot be handled with numerical methods so a practical approach is that there exists a region with a very small thickness across which properties vary with a very steep gradient. The interface representation can be achieved by various methods, implicitly and explicitly. The most popular choices are reviewed and discussed as the following. In 1976, Noh & Woodward introduced the Volume of Fraction (VOF) method, which is based on earlier Marker-and-Cell (MAC) methods[3]. The scalar fraction function C is used to construct the interface by tracking through each cell in the computational grid. A Piecewise-Linear Interface Calculation (PLIC) scheme was introduced to remedy of the imperfect interface description of VOF [4]. As pointed in [5], conventional conservative schemes cannot guarantee the sharpness of the front, due the excessive numerical diffusion. And the higher order schemes can incur numerical oscillations near the front. Unverdi & Tryggavason introduced the front tracking method [5], where the interface is constructed by adding or subtracting points to the front. However, this complication is amplified when the algorithm is used to solve a three-dimensional problem. Both the two general explicit frameworks for the interface representation lack the accuracy for calculation of the related geometric terms inherently.

Osher and Sethian introduced a method based on a level set formulation for the interface representation [6]. This method eliminated the numerical oscillations in the conventional schemes and the complication of adding or subtracting points to the front. The merging and breaking of the interface can be taken care of automatically by this implicit smooth function. Furthermore, the geometric terms can be accurately calculated based on the method's own characteristics, where the curve or surface separating the fluids never need to be interpolated.

The numerical investigations are further extended when coupled with the energy equation. The single-phase Rayleigh-Bénard convection has been studied analytically and numerically. Bénard first conducted the quantitative experiments and studied the stability of a thin layer fluid imposed to a vertical temperature gradient with a free upper surface [1]. Lord Rayleigh proposed his linear stability analysis [2] and was accepted as explanation for the Bénard's results until Pearson pointed out the role of surface tension, which is referred as the thermal Marangoni effect [7]. Based on the thickness of the fluid layer, the effect of buoyancy and surface tension are in competition for dominating the flow and there exists a compensation thickness where the two effects balance each other [8]. Recent experimental results on multiphase convection showed a dramatic increase in the heat transfer properties by introducing a dispersed phase interacting the primary phase thermally and mechanically[9]. Similar numerical simulations with the presence of a second phase in a cylindrical cell has a profound effect on the flow behavior and heat transfer[10]. The numerical simulation of the two-layer convection system was used to prove a thermal Lattice Boltzmann model [11]. A linear stability analysis for the double-layer system was presented and the results were compared with CFD simulation [12]. However, it is not entirely clarified for the critical Rayleigh number and wave number for the onset of convection in the multiphase flow regime. Therefore, further numerical investigations must be carried out that could help to understand the temporal and the spatial characteristics of flow structures in the multiphase Rayleigh-Benard convections.

1.2 Dissertation structure

In this study, we combine the level set method with a projection algorithm to solve the Navier-Stokes equation for multiphase flow. The energy equation shall be coupled and solved for investigating the multiphase Rayleigh-Bénard convections. The dissertation is structured as follows. The numerical techniques are detailed in Chapter 2. A brief summary is also included for the numerical algorithm employed. In Chapter 3 the spatial and temporal discretization schemes are presented for the governing equations and related terms. The results of numerical investigations are presented in Chapter 4. A short conclusion and outlook for future investigations are presented in Chapter 5.

Chapter 2

Mathematical Model

Fluid flows are encountered in nature and many critically important industrial applications. The recent development of semiconductor industry now allows the numerical simulations to expand into a finer resolution with significantly decreased computational time. In this chapter, we present a robust numerical algorithm to solve complex flow problems of multiple fluids.

2.1 Governing equation

Equations governing the fluid motion are Navier-Stokes equations presented below

$$\frac{\partial u}{\partial t} + \nabla(u \cdot u) = -\frac{1}{\rho}\nabla p + \nabla(\nabla \cdot u + \nabla^{T} \cdot u) + f \qquad (1)$$

where μ is the dynamic viscosity of the fluid and f is the external force.

The fluid density is considered as a function of temperature. The density of fluid particle is to remain constant, hence the following equation represent the change of density in the flow domain

$$\frac{D\rho}{Dt} = \frac{\partial \rho}{\partial t} + u \cdot \nabla \rho = 0 \qquad (2)$$

where $\mathrm{D}()/\mathrm{Dt}$ is the material derivative. For the conservation of mass equation of incompressible flow, this equation reduces to

$$\nabla \cdot u = 0 \tag{3}$$

For multiple fluids, one fluid is separated from another by a sharp interface and the density of particles in each fluid is constant. Instead of solving equation (2) every time step, the density can be reconstructed from the location of the interface.

For flows in multiple dimensions, the momentum equation (1) can be written in each direction. In a two dimensional geometry:

$$\rho\left(\frac{\partial u}{\partial t}+\frac{\partial uu}{\partial x}+\frac{\partial uv}{\partial y}\right)=-\frac{\partial p}{\partial x}+\rho g_x+\frac{\partial}{\partial x}2\mu\frac{\partial u}{\partial x}+\frac{\partial}{\partial y}\mu\left(\frac{\partial u}{\partial y}+\frac{\partial v}{\partial x}\right)+f_x \tag{4}$$

$$\rho\left(\frac{\partial v}{\partial t}+\frac{\partial uv}{\partial x}+\frac{\partial vv}{\partial y}\right)=-\frac{\partial p}{\partial y}+\rho g_y+\frac{\partial}{\partial x}\mu\left(\frac{\partial u}{\partial y}+\frac{\partial v}{\partial x}\right)+\frac{\partial}{\partial y}2\mu\frac{\partial v}{\partial y}+f_y \tag{5}$$

the continuity equation (1.3) is expanded,

$$\frac{\partial u}{\partial x}+\frac{\partial v}{\partial y}=0 \tag{6}$$

And this can be easily expanded into the third dimension for the Navier-Stokes equation and continuity equation.

For incompressible flow, the advection term can be shown in the following manners

$$\rho\left(\frac{\partial u}{\partial t}+\nabla\cdot uu\right)=\rho\left(\frac{\partial u}{\partial t}+u\nabla\cdot u\right)=\frac{\partial \rho u}{\partial t}+\nabla\cdot\rho uu \tag{7}$$

For constant viscosity ($\mu=\mu_o$), the diffusion terms can be written as:

$$\nabla\cdot\mu_o(\nabla u+\nabla^T u)=\mu_o\nabla^2 u \tag{8}$$

2.2 Fractional projection

Projection Method" which was introduced by Chorin[13] in 1967 can be used to integrate the Navier-Stokes equations. The solution is obtained in a fractional step manner. First, the velocity is advanced in time without the influence of the pressure term in the momentum equation and a non-divergence free velocity is obtained. The predicted velocity field is used to calculate and update the pressure field under certain convergence criterion. Then the velocity field is corrected by the updated pressure to ensure the incompressibility of the flow.

To illustrate how this works, we shall first use a simple first-order explicit time marching scheme and higher order schemes can be employed at the later stage.

$$\frac{u^{n+1} - u^{n}}{\Delta t} + A(u^{n}) = -\frac{1}{\rho}\nabla p + \nu D(u^{n}) + f^{n} \tag{9}$$

$$\nabla \cdot u^{n+1} = 0 \tag{10}$$

The superscript n and $n+1$ denotes the corresponding values at current and future time steps, respectively. Function *A()* and *D()* are numerical approximations for the advection and the diffusion terms, ν is the kinematic viscosity and f is the numerical approximation for body forces acting on the fluid.

Following the theory of the projection method, a temporary velocity u^{*} is introduced,

$$u^{n+1} = u^{n+1} - u^{*} + u^{*} - u^{n} \tag{11}$$

and the momentum equation is split into two parts as follow.

$$\frac{u^{*} - u^{n}}{\Delta t} + A(u^{n}) = \nu D(u^{n}) + f^{n} \tag{12}$$

$$\frac{u^{n+1} - u^*}{\Delta t} = -\frac{1}{\rho}\nabla p^{n+1} \tag{13}$$

Adding the two equations (12,13) together yields the exactly equation (9).

The pressure Poisson's equation can be obtained by taking gradient of equation (13) and u^{n+1} is eliminated based on the incompressibility and reduces to

$$\frac{1}{\Delta t}\nabla \cdot u^* = \frac{1}{\rho}\nabla^2 p^{n+1} \tag{14}$$

After the Poisson's equation is solved, the projected velocity at time step *n+1* can be found by using equation (13).

2.3 Level set method

Back to 1988, the level set method was introduced by Osher and Sethian for tracking the propagating the front of flame[6]. In 1994,Sussman, Smereka and Osher further extended this method for multiphase flow simulations [14] and this method has become the main alternative of the volume fraction method in direct advection of the marker function. The level set method does not make any assumption about the connectivity of the interface, based on its mathematical characteristic. When the interface between fluids undergoes topological changes, like burble coalescing or breaking up, no interpolation or intervention is needed to continue the computation by using the level set function, as of its own smoothness. Also, the geometric terms, like normal and curvature, can be easily discretized and accurately calculated.

By using an implicit function ϕ, the interface separating the different phases is represented by the zero-level set of the function.

$$\Gamma = \{x|\phi(x,t) = 0\} \tag{15}$$

Here, the lighter fluid or gas resides in the region where $\phi < 0$ and the heavier fluid or liquid takes the region where $\phi > 0$. Hence, we have

$$\phi(x,t) \begin{cases} > 0, & if\ x \in liquid \\ = 0, & if\ x \in \Gamma \\ < 0, & if\ x \in gas \end{cases} \tag{16}$$

We set the normal direction always as pointing from gas to liquid. The unit normal and curvature terms of the interface are calculated by

$$n = \frac{\nabla\phi}{|\nabla\phi|}\bigg|_{\phi=0} \text{and } \kappa = \nabla \cdot (\frac{\nabla\phi}{|\nabla\phi|}\bigg|_{\phi=0} \tag{17}$$

The evolution of the interface, which moves with the fluid particles, is given by

$$\frac{\partial\phi}{\partial t} + u \cdot \nabla\phi = 0 \tag{18}$$

where u is the fluid velocity. The above equation is guaranteed by the nature of the level set function that should be constant along the particle path. That yields

$$\frac{d\phi(x(t),t)}{dt} = 0 \tag{19}$$

And with $dx(t)/dt \equiv u$,

$$\frac{dx(t)}{dt} \cdot \nabla\phi(x,t) + \frac{\partial\phi(x,t)}{dt} = 0 \tag{20}$$

yields equation (18).

As we treat the density and the viscosity as constant in each phase, the values of these two properties are separated by the sing of ϕ

$$\rho(\phi) = \rho_g + \left(\rho_l - \rho_g\right)H(\phi) \tag{21}$$

$$\mu(\phi) = \mu_g + \left(\mu_l - \mu_g\right)H(\phi) \tag{22}$$

The subscripts g an l denote the gas and the liquid phase, respectively. And $H(\phi)$ is the Heaviside function, which is

$$H(\phi) = \begin{cases} 0 \\ 1/2 \\ 1 \end{cases} \tag{23}$$

2.4 Surface tension model

Due to the discontinuous change of fluid properties, which lead to the abrupt changes in molecular forces, the surface tension becomes an inherent material property at the interface to balance the jump of stress and pressure. Brackbill et al. introduced a continuum surface force (CSF) model, which can handle the complex interface topology[15]. The CSF model treats the surface tension as a continuous volume effect across the interface instead of a boundary value condition. Chang et al. further adapted the CSF model with the level set method[16]. The effect of a surface tension is described as a singularized forced term localized on the fluid interface, which is corresponding to the zero level set of ϕ.

$$f_s \equiv \sigma \kappa n = \sigma \kappa(\phi) \delta(\phi) \nabla \phi \tag{24}$$

where $\delta(\phi)$ is the Dirac delta function.

2.5 Smoothing

Setting a small but a finite thickness for the interface can alleviate the numerical difficulties in the first step of Chorin’s projection method raised by the sharp changes in density across the interface. A constant thickness of the interface can also help resolving the discontinuity in calculation of $\delta(\phi)$ for the surface tension. Hence, we set the smoothed Heaviside function as

$$H_\epsilon(\phi) = \begin{cases} 0 & \text{if } \phi < \epsilon \\ \frac{1}{2}\left[1 + \frac{\phi}{\epsilon} - \frac{1}{\pi}\sin(\pi\phi/\epsilon)\right] & \text{if } |\phi| \leqslant \epsilon \\ 1 & \text{if } \phi > \epsilon \end{cases} \tag{25}$$

Equivalently, the modified delta function is

$$\delta_\epsilon(\phi) = \frac{dH}{d\phi} \tag{26}$$

Now, the thickness of the interface is set to $\frac{2\epsilon}{|\nabla\phi|}$. in order to have a uniform thickness across the interface, it is favorable to make the term in the dominator, $|\nabla\phi|$, as a constant value within $|\phi| \leq \epsilon$. The common way to accomplish that is to initialize the level set function as a distance function,

$$|\nabla\phi| = 1. \tag{27}$$

2.6 Re-initialization of the level set function

When moving the zero level set using equation (18) under the correct velocity, the level set function will not remain as a distance function after a short period of time. Since preserving this feature is important to ensure the accurate calculation for the gradient of the level set function, $|\nabla\phi|$, a reinitialization algorithm is needed to keep the level set function as a distance function. Several algorithms are introduced [17–19] and one introduced by Sussman, Smereka and Osher in 1994 gained a lot of interests[14]. This iterative approach introduced by Sussmann et al. has an advantage of cutting down the number of required iterations when the level set function ϕ is close to a distance function. This is achieved by solving the partial differential equation,

$$\frac{\partial \phi_d}{\partial \tau} = sgn(\phi)(1 - |\nabla \phi|) \tag{28}$$

with initial condition,

$$\phi_d(x, 0) = \phi(x) \tag{29}$$

where

$$sign(\phi) = \begin{cases} -1, & \phi < 0 \\ 0, & \phi = 0 \\ 1, & \phi > 0 \end{cases} \tag{30}$$

and τ is an artificial time. Since the sign function equals zero at the zero level set, the solution of equation (28) has the same zero level set as $\phi(x)$.

Rewriting equation (28) shows

$$\frac{\partial \phi_d}{\partial \tau} + sgn(\phi)\frac{\nabla \phi_d}{|\nabla \phi_d|} \cdot \nabla \phi_d \ = sgn(\phi) \tag{31}$$

Equation (31) is a nonlinear hyperbolic equation whose characteristic velocities pointing outwards from the interface in the direction of the normal. This makes ϕ_d to be reinitialized to the distance function near the interface first. As we only have the interest near the interface area, we can stop the iteration steps once the level set function is properly reinitialized near the interface.

2.7 Rayleigh-Bénard Convection

For a fluid at rest is heated from below and cooled from above, the onset of fluid motion can occur when the critical condition is reached. The organized periodic counter-rotating vorticity rolls will appear in the flow. The principal of the instability is buoyancy driven effects.. Most studies in this field considered single phase flows but a little attention has been given to multiphase flows.

In Rayleigh-Bénard convection, the fluid motion induced by the density stratification which is causedby Velocity, temperature and pressure fields are determined by solving equations derived from conservation laws: conservation of mass, momentum and energy.. The Navier-Stokes equations are presented in the previous sections. The energy equation for the temperature field is.

$$\frac{\partial T}{\partial t} + u \cdot \nabla T = \chi \nabla^2 T \tag{32}$$

where χ is the thermal diffusivity of the fluid. The equation of state is

$$\rho = \rho_0 (1 + \alpha \Delta T) \tag{33}$$

where α is the volume expansion coefficient of the fluid and is usually negative, ρ_0 is the density of fluid at the reference temperature T_0. Hence the density will decrease when the fluids is heated. Based on the Boussinesq approximation, the density is treated as constant except in the buoyancy term in the momentum equation. Material properties such as the viscosity, the thermal diffusivity and the volume expansion coefficient are assumed to be constant.. With this assumption, the Navier-Stokes equation becomes

$$\frac{\partial u}{\partial t} + \nabla(u \cdot u) = -\frac{1}{\rho_0} \nabla p + \frac{\mu}{\rho_0} \nabla(\nabla \cdot u + \nabla^T \cdot u) + \frac{\rho}{\rho_o} g + f \tag{34}$$

2.8 Summary

Summary of the algorithm is as follows:

Step 1. Initialize the level set function to be signed as a distance function.

Step 2. Solve the Navier-Stokes equation with Chorin’s projection method. For each time step, the physical properties, such as density, viscosity, thermal diffusivity are constructed based on the interface location which is represented as the zero-level set of level set function.

The level set function is advected under the updated velocity field obtained above.

Solve the energy equation.

Step 3. Re-initialize the level set function back to a signed distance function by solving the PDE below to obtain the steady state solution.

Step 4. Repeat step 2 and 3 until desired the set flow time is reached.

Chapter 3

Numerical Algortihm

3.1 Temporal discretization

In the previous chapter, the first order time integration scheme was used for the illustration of the Chorin's projection method. However, this simple explicit forward-in-time algorithm only provides first-order accuracy. For most problems, it is desirable to have a second-order or higher order time integration method to ensure the numerical stability.

The Runge-Kutta method, which is generally referred to as "RK4", is implemented in our current numerical method. The RK4 approximates the value at t_{n+1} with the current value at t_n plus the weighted average of four increments, k_1, k_2, k_3, k_4. A quick comparison for the accuracy between RK4 and first order Euler methods is made by solving a simple ODE. The following equation is solved

$$x' = f(t,x) = dx/dt \ = xsint \tag{35}$$

with initial condition $x(0) = -1$.

$$x_{n+1} = x_n + \frac{h}{6}(k_1 + 2k_2 + 2k_3 + k_4) \tag{36}$$

$$t_{n+1} = t_n + h \tag{37}$$

for *n = 0, 1, 2, 3, …*, using

$$
\begin{aligned}
k_1 &= f(t_n, x_n), \\
k_2 &= f\left(t_n + \frac{h}{2}, x_n + \frac{h}{2}k_1\right), \\
k_3 &= f\left(t_n + \frac{h}{2}, x_n + \frac{h}{2}k_2\right), \\
k_4 &= f(t_n + h, x_n + hk_3).
\end{aligned}
\tag{38}
$$

In Figure 1, the data points of blue circle and green star are obtained by using RK4 and first order Euler methods, respectively. The solid line represents the analytical solution. The solution obtained by the forward Euler method quickly drift away from the analytical solution after certain time steps. In comparison, the RK4 maintained a good convergence behavior at all times. Similar patterns can also be observed in Figure 2. Deviation between the analytical solution and solution obtained by RK4 is nearly zero at all times while there is a large deviation between the analytical solution and the solution obtained by forward Euler schemes.

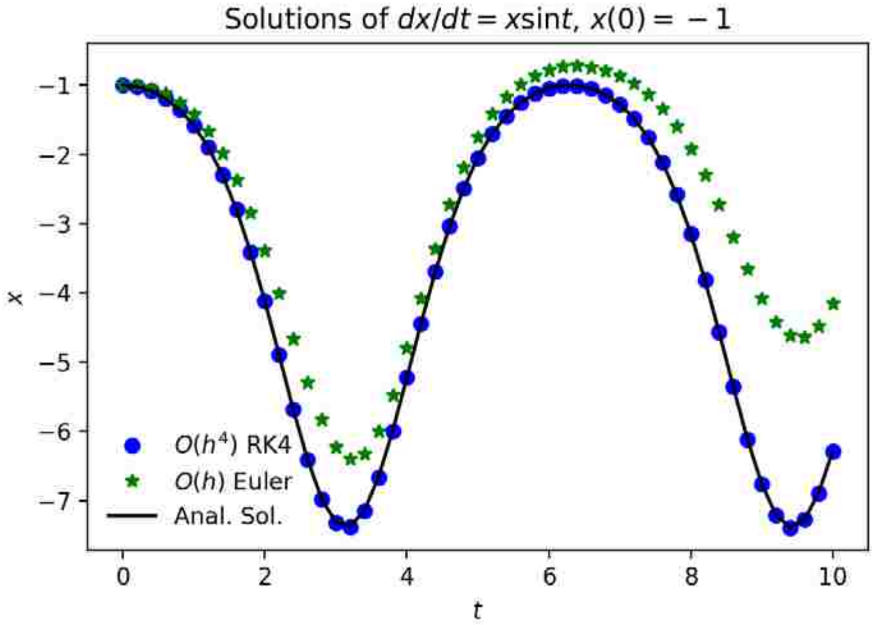

Figure 1 Solutions of dx/dt =xsint, x(0) = -1 with RK4 and first order Euler

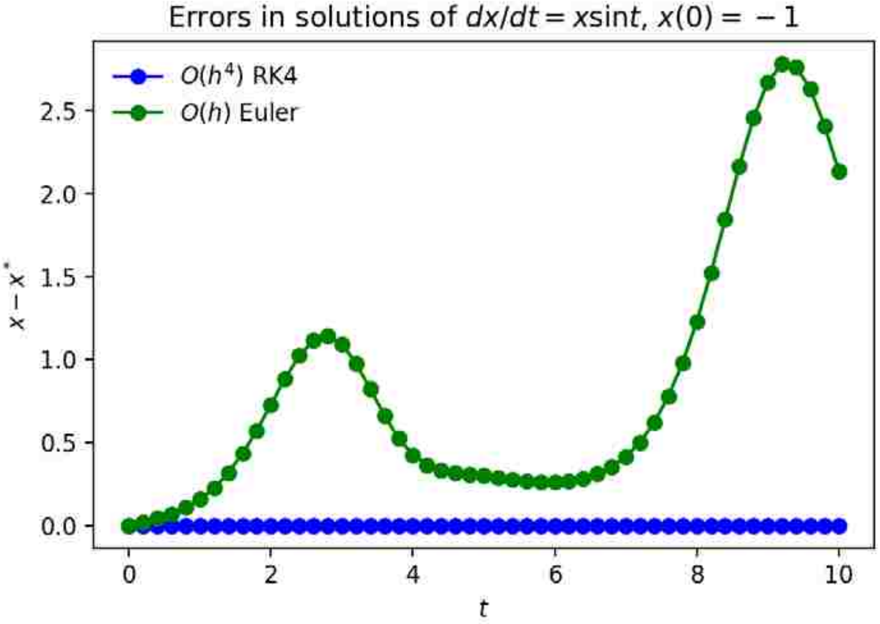

Figure 2 Errors in solutions with RK4 and first order Euler

3.2 Spatial discretization

To discretize the governing equation, the Finite-Volume approach is used and conservation principals are applied to small control volumes. For the shape of the control volume, we choose the structured Cartesian grids for our work. Regular structured grid is relatively simple and efficient for numerical code development, as the various variables are stored at the points on the intersection of orthogonal grid lines. Instead of using a collocated structured grid, which stores all the variables on the same grid point for each control volume, we put the u velocity components on the vertical boundaries and v velocity components on the horizontal boundaries in a two dimensional space. And the scalars, like pressure, density, level set function etc. are stored in the cell centers. In a three dimensional space, the vector variables, u, v, w, are placed on the faces of the volume. The scalars are put in the center of the volume. A simple illustration is showed in Figure 3 and Figure 4.

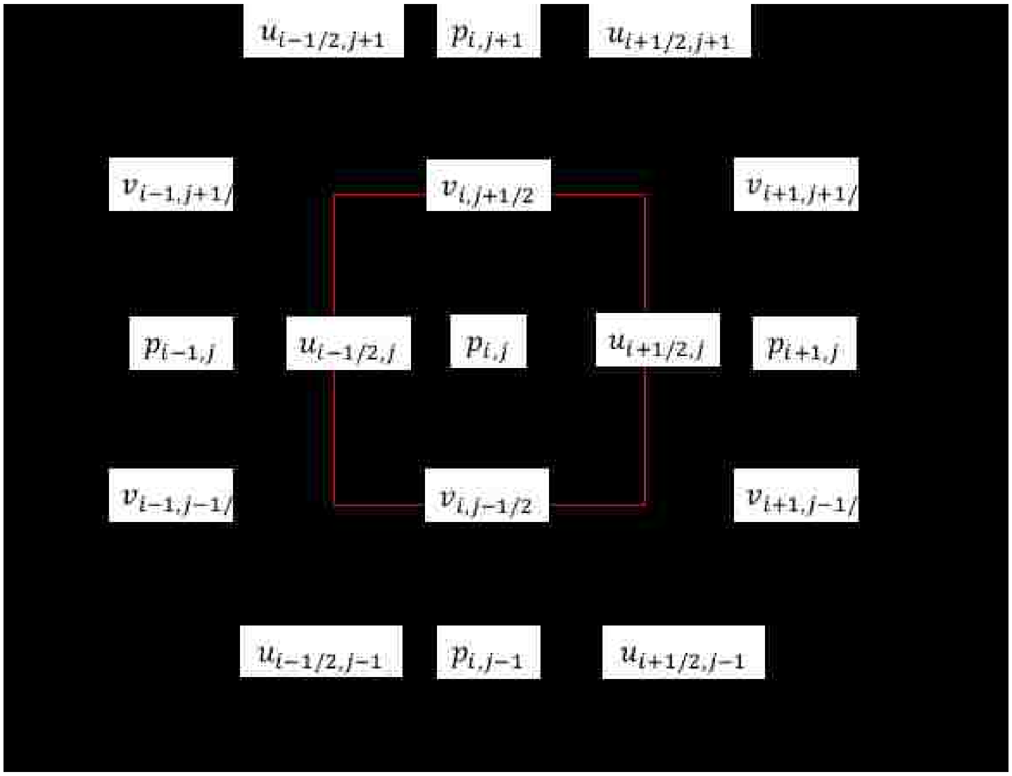

Figure *3 Staggered mesh decomposition for control volumes in 2D*

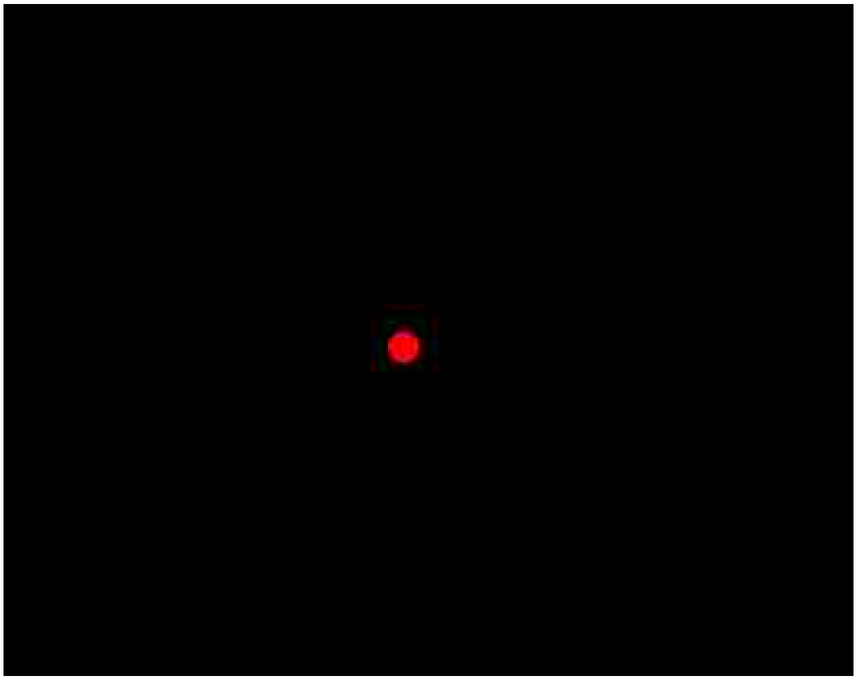

Figure 4 Staggered mesh decomposition for control volumes in 3D

This kind of discretization is usually referred as a staggered mesh. The chief benefit from the staggered mesh is eliminating the odd-even decoupling problem on the collocated mesh, which is generated by the result of when variables entering the equation only in the first order derivatives.

Based on the setup of the staggered mesh, setting the boundary value of the normal velocity for each boundary is trivial. It is directly set as what it should be as the center of the control volume coincides with the boundary. The tangential velocity is determined by a linear interpolation between the velocity of ghost node and the node next to the boundary. To illustrate this, we take the y-velocity component on the left boundary

$$v_{wall} = 1/2(v_{i,j} + v_{2,j}) \tag{39}$$

where $v_{1,j}$ is the value on the ghost node. For a no-slip boundary, v_{wal} is equal to zero, which means the value of $v_{1,j}$ is just the reflection of $v_{2,j}$.

For a finite-volume method, the average velocity is used in each control volume. For each term in the Navier-Stokes equation, it is approximated by the average value over the control volume. The averages for the advection and the viscous terms over each control volume are:

$$A(u^n) = \frac{1}{\Delta V}\int_V \nabla \cdot (u^n u^n) dv = \frac{1}{\Delta V}\oint_S u^n (u^n \cdot n) ds \tag{40}$$

and

$$D(u^n) = \frac{\mu_0}{\Delta V}\int_V \nabla^2 u^n dv = \frac{\mu_0}{\Delta V}\int_V \nabla \cdot \nabla u^n dv = \frac{\mu_0}{V}\oint_S \nabla u \cdot n \, ds \tag{41}$$

where we converted the volume of the control volume, ΔV, into the surface, S, by applying the divergence theorem.

A simple square or cubic control volume scheme is selected to show how the surface and volume integrals are approximated. Here we assume a two-dimensional flow and the extension into the third dimensional space is easy and straightforward. The control volume bounded by red lines in Figure 3 is selected and identified as (i, j). The neighbor control volumes are indexed by $(i \pm 1, j)$ and $(i, j \pm 1)$, respectively. The edges are identified half-indices away from the center of each control volume. The incompressibility condition is evaluated at the pressure control volume centered at (i, j) and discretized as

$$u^{n+1}_{i+1/2,j} - u^{n+1}_{i-1/2,j} + v^{n+1}_{i,j+1/2} - v^{n+1}_{i-1/2,j} = 0 \tag{42}$$

where the integrals along the edges are approximated by the mid-point rule.

Similarly, the approximation for the predictor step and projection step can be discretized at the u- and v-velocity control volumes.

For the predictor step,

$$u^{*}_{i+1/2,j} = u^{n}_{i+1/2,j} + \Delta t(-(A_x)^{n}_{i+1/2,j} + \nu(D_x)^{n}_{i+1/2,j} + (f_x)_{i+1/2,j} \tag{43}$$

$$v^{*}_{i,j+1/2} = v^{n}_{i,j+1/2} + \Delta t(-\left(A_y\right)^{n}_{i,j+1/2} + \nu\left(D_y\right)^{n}_{i,j+1/2} + \left(f_y\right)_{i,j+1/2} \tag{44}$$

And for the projection step

$$u^{n+1}_{i+1/2,j} = u^{*}_{i+1/2,j} - \frac{1}{\rho}\frac{\Delta t}{h}(p^{n+1}_{i+1,j} - p^{n+1}_{i,j}) \tag{45}$$

$$v^{n+1}_{i,j+1/2} = v^{*}_{i,j+1/2} - \frac{1}{\rho}\frac{\Delta t}{h}(p^{n+1}_{i,j+1} - p^{n+1}_{i,j}) \tag{46}$$

The pressure Poisson equation is derived by substituting equations (42) and (43) into the discretized continuity equation (39) and taking the divergence on both sides of the obtained equation. As the velocity is assumed to be divergence free at $t = n + 1$, the u^{n+1} and v^{n+1} are eliminated. For multiphase flow, the density and viscosity across the whole computational domain are not constant for each cell. Hence the discretized Poisson equation is

$$\frac{1}{h^2}\left(\frac{p_{i+1,j}-p_{i,j}}{\rho^n_{i+1,j}+\rho^n_{i,j}}-\frac{p_{i,j}-p_{i-1,j}}{\rho^n_{i,j}+\rho^n_{i-1,j}}+\frac{p_{i,j+1}-p_{i,j}}{\rho^n_{i,j+1}+\rho^n_{i,j}}-\frac{p_{i,j}-p_{i,j-1}}{\rho^n_{i,j}+\rho^n_{i,j-1}}\right)$$

$$=\frac{1}{2h\Delta t}\left(u^*_{i,j+1/2}-u^*_{i,j-1/2}+v^*_{i,j+1/2}-v^*_{i,j-1/2}\right) \qquad (47)$$

on an equal spaced uniform grid. To solve equation (44), we employ iteration method, where $p_{i,j}$ is isolated on the left-hand side and computed by the estimated values from the surrounding pressures. This Jacobi iteration will be ended by the prescribed convergence criteria. Comparing to Jacobi iteration's robust but slow scheme, a variation of the Gauss-Seidel, called successive over-relaxation (SOR), is implemented to help reduce the computational cost of solving the Poisson equation. For the SOR method, the weighted average of the updated value and the one from last iteration are also considered when computing for the new iteration step:

$$p^{\alpha+1}_{i,j}=\beta\left[\frac{1}{\Delta x^2}\left(\frac{1}{\rho^n_{i+1,j}+\rho^n_{i,j}}+\frac{1}{\rho^n_{i,j}+\rho^n_{i-1,j}}\right)+\frac{1}{\Delta y^2}\left(\frac{1}{\rho^n_{i,j+1}+\rho^n_{i,j}}+\frac{1}{\rho^n_{i,j}+\rho^n_{i,j-1}}\right)\right]^{-1}$$

$$\left[\frac{1}{\Delta x^2}\left(\frac{p^{\alpha}_{i+1,j}}{\rho^n_{i+1,j}+\rho^n_{i,j}}+\frac{p^{\alpha+1}_{i-1,j}}{\rho^n_{i,j}+\rho^n_{i-1,j}}\right)+\frac{1}{\Delta y^2}\left(\frac{p^{\alpha}_{i,j+1}}{\rho^n_{i,j+1}+\rho^n_{i,j}}+\frac{p^{\alpha+1}_{i,j-1}}{\rho^n_{i,j}+\rho^n_{i,j-1}}\right)\right.$$

$$\left.-\frac{1}{2\Delta t}\left(\frac{u^*_{i+1/2,j}-u^*_{i-1/2,j}}{\Delta x}+\frac{v^*_{i,j+1/2}-v^*_{i,j-1/2}}{\Delta y}\right)\right]+(1-\beta)p^{\alpha}_{i,j} \qquad (48)$$

β is the relaxation parameter and must be greater than 1 for an over-relaxation and smaller than 2 for a stability reasons. A balanced range of β for the compromise between the stability and an accelerated convergence is between 1.2 and 1.5.

With the illustrated layout for the control volumes in Figure 3, midpoint rule is used for the approximation of the integral over each edge and a linear interpolation is used for velocities at undefined locations. And the explicit formulas for the advection terms are:

$$(A_x)_{i+1/2,j}^n = \frac{1}{h}\left\{\begin{array}{l} \left(\frac{u_{i+3/2,j}^n + u_{i+1/2,j}^n}{2}\right)^2 - \left(\frac{u_{i+1/2,j}^n + u_{i-1/2,j}^n}{2}\right)^2 \\ + \left(\frac{u_{i+1/2,j+1}^n + u_{i+1/2,j}^n}{2}\right)\left(\frac{v_{i+1,j+1/2}^n + v_{i,j+1/2}^n}{2}\right) \\ - \left(\frac{u_{i+1/2,j}^n + u_{i+1/2,j-1}^n}{2}\right)\left(\frac{v_{i+1,j-1/2}^n + v_{i,j-1/2}^n}{2}\right) \end{array}\right\} \tag{49}$$

$$\left(A_y\right)_{i,j+1/2}^n = \frac{1}{h}\left\{\begin{array}{l} \left(\frac{v_{i,j+3/2}^n + v_{i,j+1/2}^n}{2}\right)^2 - \left(\frac{v_{i,j+1/2}^n + v_{i,j-1/2}^n}{2}\right)^2 \\ + \left(\frac{u_{i+1/2,j}^n + u_{i+1/2,j+1}^n}{2}\right)\left(\frac{v_{i,j+1/2}^n + v_{i+1,j+1/2}^n}{2}\right) \\ - \left(\frac{u_{i-1/2,j+1}^n + u_{i-1/2,j}^n}{2}\right)\left(\frac{v_{i,j+1/2}^n + v_{i-1,j+1/2}^n}{2}\right) \end{array}\right\} \tag{50}$$

The explicit discretization formulas for the diffusion terms with non-constant viscosities are:

$$(D_x)_{i+1/2,j}^n =$$

$$\frac{1}{h^2}\left\{\begin{array}{c} 2\mu_{i+1,j}^n\left(u_{i+3/2,j}^n - u_{i+1/2,j}^n\right) - 2\mu_{i,j}^n\left(u_{i+1/2,j}^n - u_{i-1/2,j}^n\right) \\ +\mu_{i+1/2,j+1/2}^n\left(u_{i+1/2,j+1}^n - u_{i+1/2,j}^n + v_{i+1,j+1/2}^n - v_{i,j+1/2}^n\right) \\ -\mu_{i+1/2,j-1/2}^n\left(u_{i+1/2,j}^n - u_{i+1/2,j-1}^n + v_{i+1,j-1/2}^n - v_{i,j-1/2}^n\right) \end{array}\right\} \tag{51}$$

and

$$\left(D_y\right)_{i+1/2,j}^n =$$

$$\frac{1}{h^2}\left\{\begin{array}{c} 2\mu_{i,j+1}^n\left(v_{i,j+3/2}^n - v_{i,j+1/2}^n\right) - 2\mu_{i,j}^n\left(v_{i,j+1/2}^n - v_{i,j-1/2}^n\right) \\ +\mu_{i+1/2,j+1/2}^n\left(u_{i-1/2,j+1}^n - u_{i-1/2,j}^n + v_{i,j+1/2}^n - v_{i-1,j+1/2}^n\right) \\ -\mu_{i-1/2,j+1/2}^n\left(u_{i+1/2,j}^n - u_{i+1/2,j-1}^n + v_{i+1,j-1/2}^n - v_{i,j-1/2}^n\right) \end{array}\right\} \tag{52}$$

As the viscosity is stored at the center of the control volume, the viscosities at the points where it is not defined are calculated by the geometric mean.

$$\mu_{i+1/2,j+1/2}^{n} = \sqrt[4]{\mu_{i+1,j}^{n} \times \mu_{i+1,j+1}^{n} \times \mu_{i,j+1}^{n} \times \mu_{i,j}^{n}} \tag{53}$$

3.3 Level set function advection and re-initialization

First we employed a simpler monotone upwind scheme, such as Godunov's scheme, to determine the evolution of the level set function. However, this scheme quickly became unstable. In order to have a stable and accurate advection of the level set function, we looked into the essentially non-oscillatory (ENO) and the weighted essentially non-oscillatory (WENO) scheme[20–22]. The WENO method provides a higher order accuracy in smooth regions and maintains a stable, non-oscillatory, and sharp discontinuous transition.

For the advection of the level set function, the following hyperbolic conservation law and the initial condition are used:

$$\begin{cases} \phi_t + \nabla \cdot f(\phi) = 0 \\ \phi(x,0) = \phi_0(x) \end{cases} \tag{54}$$

Let

$$\overline{\phi_\iota}(t) = \frac{1}{\Delta x_i} \int_{I_i} \phi(x,t)\, dx \tag{55}$$

After integration, the hyperbolic equation on a cell I_i

$$\frac{d}{dt}\overline{\phi_\iota}(t) + \frac{1}{\Delta x_i}\left(f\left(\phi\left(x_{i+1/2}, t\right)\right) - f\left(\phi\left(x_{i-1/2}, t\right)\right)\right) = 0 \tag{56}$$

The flux $f\left(\phi\left(x_{i+1/2}, t\right)\right)$ is replaced with a monotone numerical flux $\hat{f}(\phi_{i+1/2}^{-}, \phi_{i+1/2}^{+})$. Hence, the monotone numerical flux is reconstructed.

The basic idea behind the WENO, the same as the ENO, is an approximation procedure. For the ENO, a polynomial of degree at most two, $p_1(x)$, is used to interpolate the function $\phi(x)$ with a stencil $\hat{f}(\phi^-_{i+1/2}, \phi^+_{i+1/2})$. Hereinafter, the $\phi^{(1)}_{i+\frac{1}{2}} \equiv p_1(x_{i+\frac{1}{2}})$ is used as the approximation of $\phi\left(x_{i+1/2}\right)$, which is explicitly given as

$$\begin{aligned} \phi^{(1)}_{i+1/2} &= \frac{1}{3}\phi_{i-2} - \frac{7}{6}\phi_{i-1} + \frac{11}{6}\phi_i \\ \phi^{(2)}_{i+1/2} &= -\frac{1}{6}\phi_{i-1} + \frac{5}{6}\phi_i + \frac{1}{6}\phi_{i+1} \\ \phi^{(3)}_{i+1/2} &= \frac{1}{3}\phi_i + \frac{5}{6}\phi_{i+1} - \frac{1}{6}\phi_{i+2} \end{aligned} \tag{57}$$

This approximation is a linear combination of three third order approximation.

$$\phi_{i+\frac{1}{2}} = \gamma_1\phi^{(1)}_{i+\frac{1}{2}} + \gamma_3\phi^{(2)}_{i+\frac{1}{2}} + \gamma_3\phi^{(3)}_{i+\frac{1}{2}} \tag{58}$$

where $\gamma_1 = \frac{1}{10}, \gamma_2 = \frac{3}{5}, \gamma_3 = \frac{3}{10}$.

This method is usually referred to as the linear weighted ENO with the smooth function in stencil *S*. If there is any discontinuity for the function in S_1, S_2, S_3, the approximation will not be good. To alleviate this, a nonlinear combination of weight is used with the introduction of the smoothness indicator, β. The nonlinear weights with smoothness indicator are

$$w_j = \frac{\widetilde{w_j}}{\widetilde{w_1} + \widetilde{w_2} + \widetilde{w_3}}, \qquad with \quad \widetilde{w_j} = \frac{\gamma_j}{\left(\epsilon + \beta_j\right)^2} \tag{59}$$

3.4 Time step restrictions

With the explicit algorithm described above, a relatively stringent limitation should apply to the time step. For the convective terms, the Courant-Friedrichs-Lewy condition limits the time step to

$$\Delta t_c \equiv \min(\frac{h}{|\vec{u}|})$$

The viscous term, the stiff source term, the gravity, the surface tension, and the heat diffusion influence the choice of time steps; leading to following restriction:

$$\Delta t_v \equiv \frac{C_v h^2}{\nu}, \qquad \Delta t_s \equiv \sqrt{\frac{(\rho_l+\rho_g)B}{8\pi}}\,h^{3/2}, \qquad \Delta t_T \equiv \frac{1}{4}\frac{h^2}{K}$$

$$\Delta t = \frac{1}{2}\min(\Delta t_c, \Delta t_v, \Delta t_s, \Delta t_T)$$

Chapter 4

Results

Numerical simulations are carried out in two and three dimensional geometries. Two-dimensional lid-driven cavity flows of a single phase fluid are used for the algorithm validation. For multiphase flows in a two-dimensional domain, a rising gas bubble and rising multiple bubbles are used for validation and testing solver's capability for multiphase flows. Later, analysis for 2D multiphase flow is presented by benchmarking with ANSYS Fluent for a quantitative comparison on the ellipticity of the gas bubble. With added energy equation and Boussinesq approximation, the 2D and 3D Rayleigh-Bénard convections are studied.

4.1 Single Phase-Lid driven cavity flow

The lid-driven cavity flow is often used as a benchmark for code verification and validation, due to its simple geometry and complicated flow behavior. The motion of a fluid inside a rectangular cavity is created by a constant translational velocity of one of the boundary while others are at rest. The computational domain with boundary conditions imposed on the velocity field is shown in the figure below.

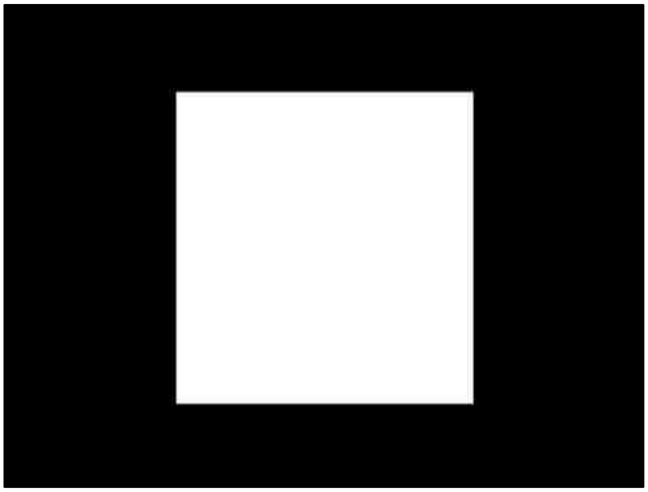

Figure 5 Lid driven cavity flow with Dirichlet boundary condition.

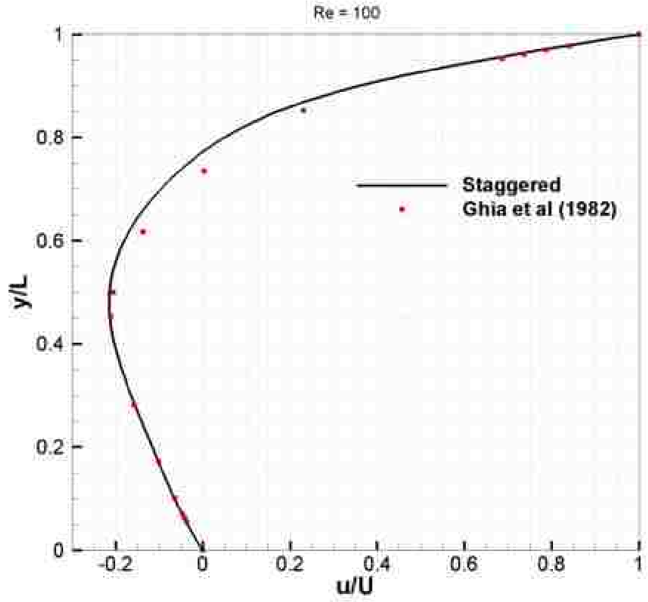

Figure 6 x-component of the velocity at center line of the domain for Re = 100. The line denotes results predicted by the present study and red symbols denote experimental results documented by Ghia et al.

In 1982 Ghia et al reported a set of data by using a non-primitive variable approach. The result generated by using our staggered discretization method is compared against Ghia's data for Reynolds number of 100. In Figure 6, profile of x-component of the velocity at x/L = 0.5is plotted in the y-direction. The velocity is normalized by the lid-speed. A maximum 3% difference in the velocity profile between our prediction and Ghia reported data is obtained; demonstrating a reasonably good agreement with previous results. This validates our mathematical model and numerical methods employed to solve flows of a single phase fluid..

4.2 Multiphase-Bubble rising & droplet

4.2.1 Validation with ANSYS Fluent

Next we compare our algorithm for the two-phase flows quantitatively against results obtained using the ANSYS Fluent commercial package. Fluent provides a wide range of well-established and validated CFD solvers. The semi-implicit SIMPLEC algorithm is selected for solving the N-S equations. The under-relaxation factor for pressure correction in SIMPLEC is generally chosen to be 1 for an accelerated convergence. The phase interface is modelled with the VOF method by solving the transport equation. With the determined the volume of fraction in each cell, the interface is interpolated by the geometric reconstruction (piecewise linear) scheme.

A numerical experiment of tracking the evolution of a single 2D gas bubble in a liquid column is proposed. The topological change on the interface and other quantities such as the velocity and the center of mass, are presented in this experiment. Initially, a gas bubble with radius $r_0 = 0.25$ resides at the lower part of the liquid column. At the top and the bottom wall, the no-slip boundary condition is used. The vertical walls are imposed with the free slip condition. The dimensions and configurations are detailed in Figure 7. The table below list the physical properties for the two fluids and the dimensionless numbers.

Table 1 Physical properties used in the algorithm validation.

Fluid	ρ	μ	g	σ	Re	Eo	ρ_1/ρ_2	μ_1/μ_2
1	1000	10	0.98	24.5	35	10	10	10
2	100	1						

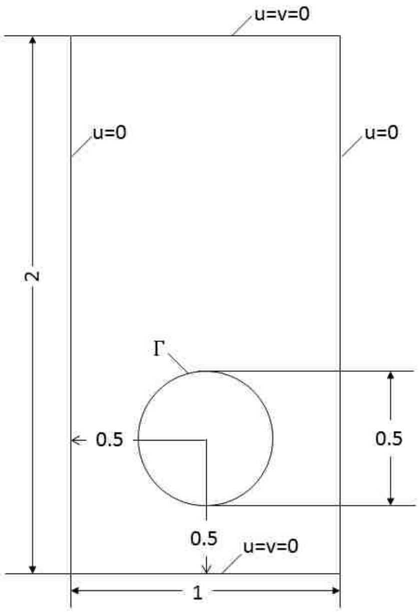

Figure 7 Initial configuration and boundary conditions for the benchmark problem.

The evolution of the bubble is tracked for three time steps and the benchmark quantities are measured during the simulation. We test a case for a bubble rising with a finite Reynolds number $Re = 35$, and both density and viscosity ratios are set to 10. A visual verification of the bubble shapes obtained by the level set method and the Fluent simulations are shown in Figure 8. Most challenging part for this comparison is from the sides at the lower part of the bubble, where significant deformations occurred. From the visual examination of the shapes, we have a good match between predictions by our numerical algorithm and Fluent.

Furthermore, the circularity of the bubble and the rise velocity are defined and compared. For a perfectly circular bubble, the circularity is equal to 1 and will decrease as the bubble is deformed. The circularity is defined as

$$\mathbb{C} = \frac{P_a}{P_b} = \frac{perimeter\ of\ area - equivalentcircle}{perimeter\ of\ bubble} = \frac{\pi d_a}{P_b} \tag{60}$$

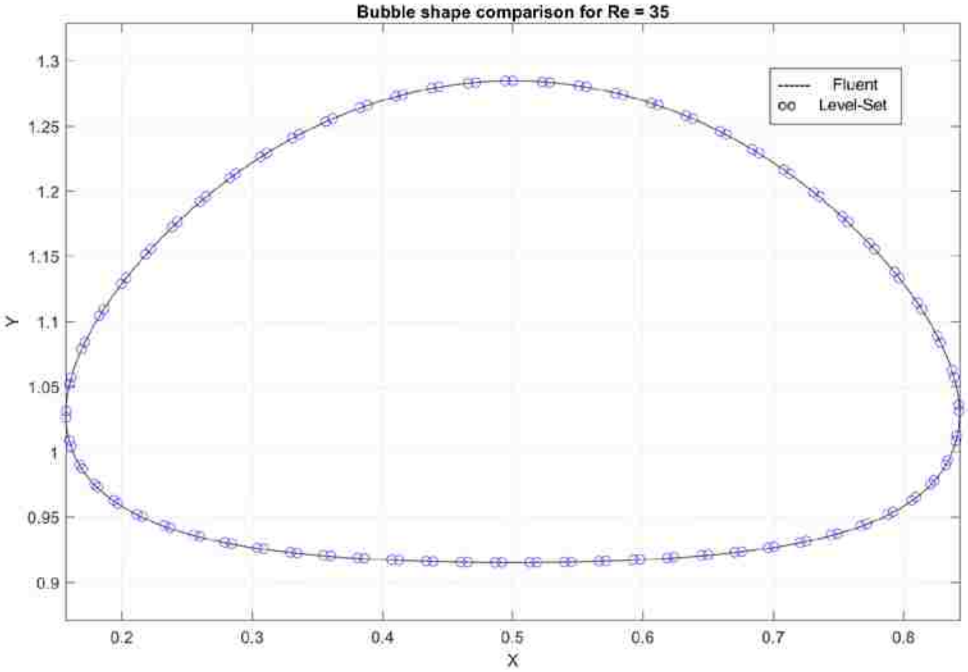

Figure 8 Bubble shape comparison at t = 3

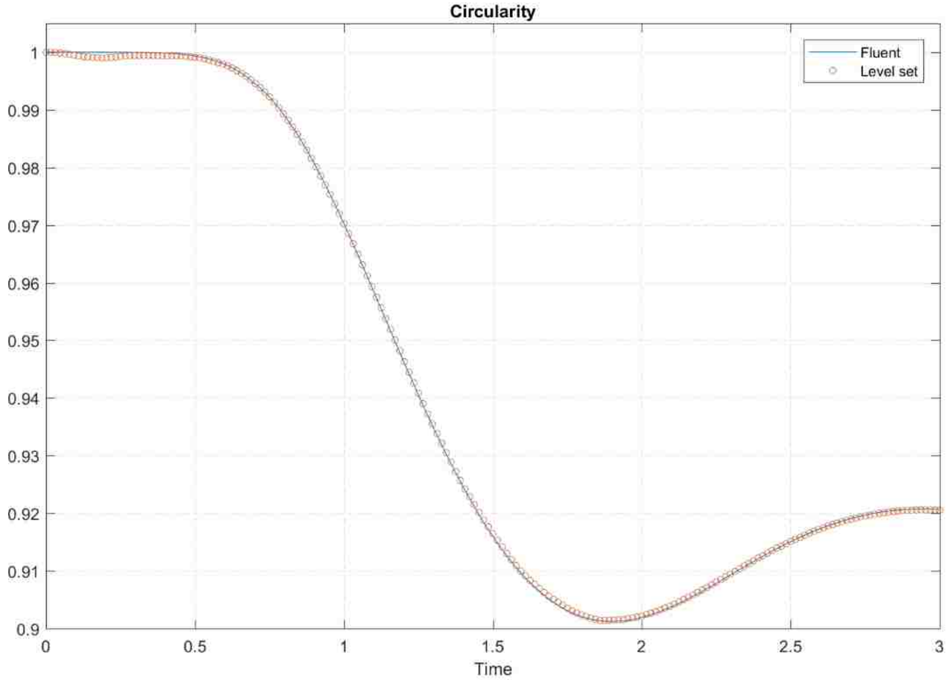

Figure 9 Circularity comparison for Re=35

Another good quantity to compare is the rise velocity, which does not only show how well of the performance of the tracking algorithm but also represent the convergence of the overall solution. The mean rising velocity is defined as

$$U_c = \frac{\int_{\Omega_g} u\,dx}{\int_{\Omega_g} 1\,dx} \tag{61}$$

where Ω_g denotes the regionoccupied by the bubble.

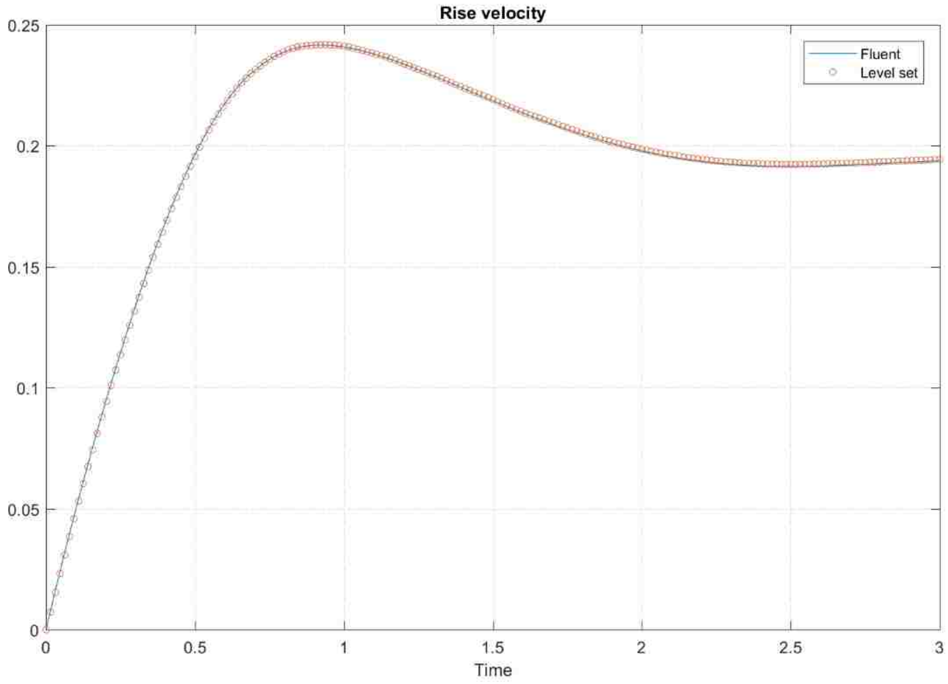

Figure 10 Mean rise velocity comparison for Re=35

With the two quantities comparison shown in Figure 9 and Figure 10, our numerical algorithm achieved a good accuracy and consistently matched with the validated CFD package. Now we can expand this method for more challenging problems.

4.2.2 Gas bubble

A small spherical gas bubble starts to rise in the heavy surrounding liquid from a stationary state. The motion of the gas bubble is influenced by buoyancy, surface tension and viscous effects. For the dynamics of the interfacial flow, the numerical stability problem may arise from the diffusion across the interface, due to the density ratio. The higher order discretization scheme and accurate interface representation would be needed to ensure the mass conservation of the gas bubble if a numerical instability occurs. Simulations for a gas bubble with a low & high density ratio to the surrounding liquid are performed. The influence of the density ratio on the motion and the deformation of the bubble is discussed. The physical properties and dimensionless number for simulating gas bubble in a low-density ratio environment are listed in Table 2 below.

Table 2 Physical properties for low density ratio gas bubble.

Fluid	ρ	μ	g	σ	Re	Eo	ρ_1/ρ_2	μ_1/μ_2
1	998.2	1e-3	9.8	0.078	8838	45	10	10
2	99.82	1e-4						

As the bubble starts to rise due the buoyancy, the formation of a jet starts to emerge at the bottom of the bubble, which pushes the bubble upwards, and the flow is circulating around the bubble, as depicted in Figure 11. When the bubble ascends with time, the velocity of the upper surface decreases. With the difference in velocity between the upper and lower surface, the bubble is deformed. The shape of the gas bubble at various time steps are shown in Figure 12**.** As time progresses the skirt of the bubble shrinks and eventually two smaller bubbles are separated from the skirt. The larger size bubble continues to move upwards, and the two smaller ones are slowed and trapped in the wake generated by the larger bubble, as shown in Figure 12.

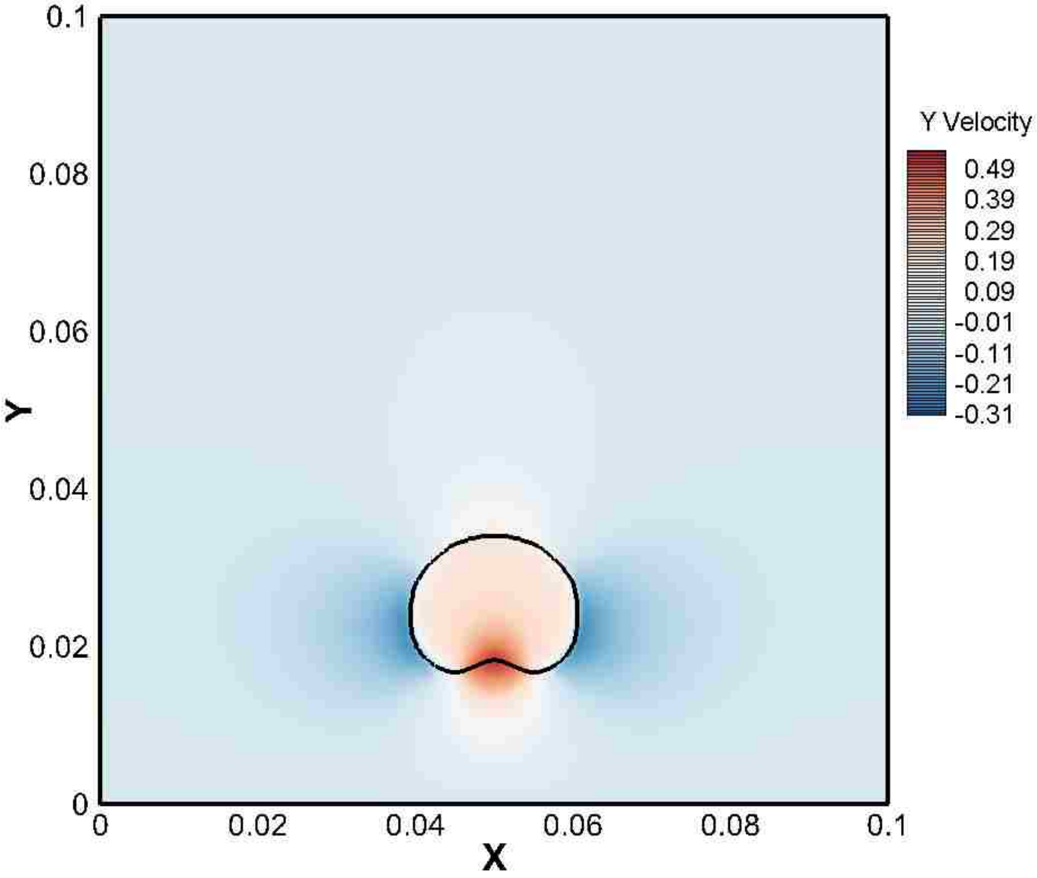

Figure 11 Bubble shape and the streamwise component of the velocity of gas bubble at t = 0.04 second for low ρ ratio.

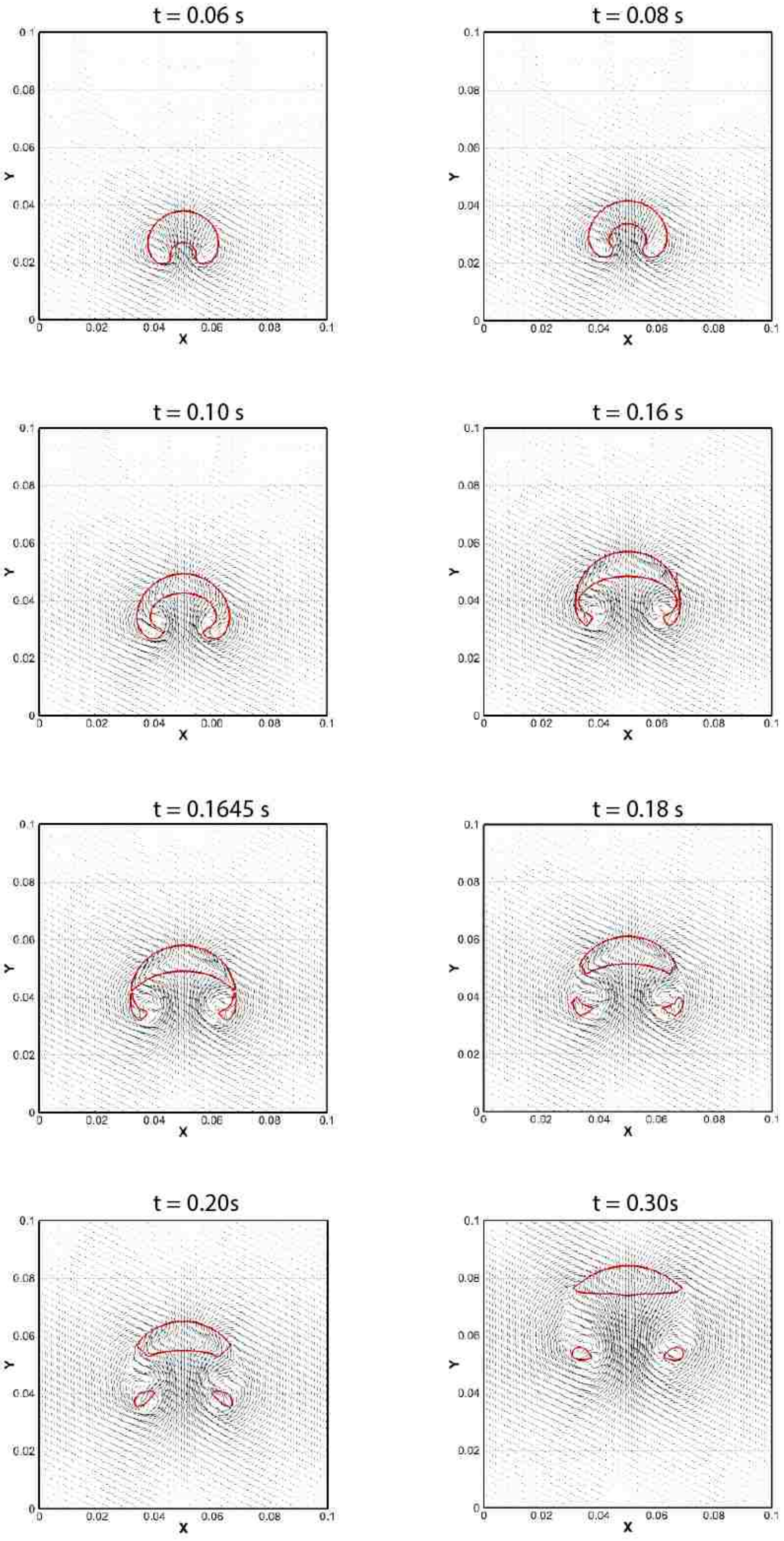
t = 0.06 s

t = 0.08 s

t = 0.10 s

t = 0.16 s

t = 0.1645 s

t = 0.18 s

t = 0.20s

t = 0.30s

Figure 12 Gas bubble shape at various time steps for ρ ratio = 10. The instantaneous velocity vector field is shown at various times.

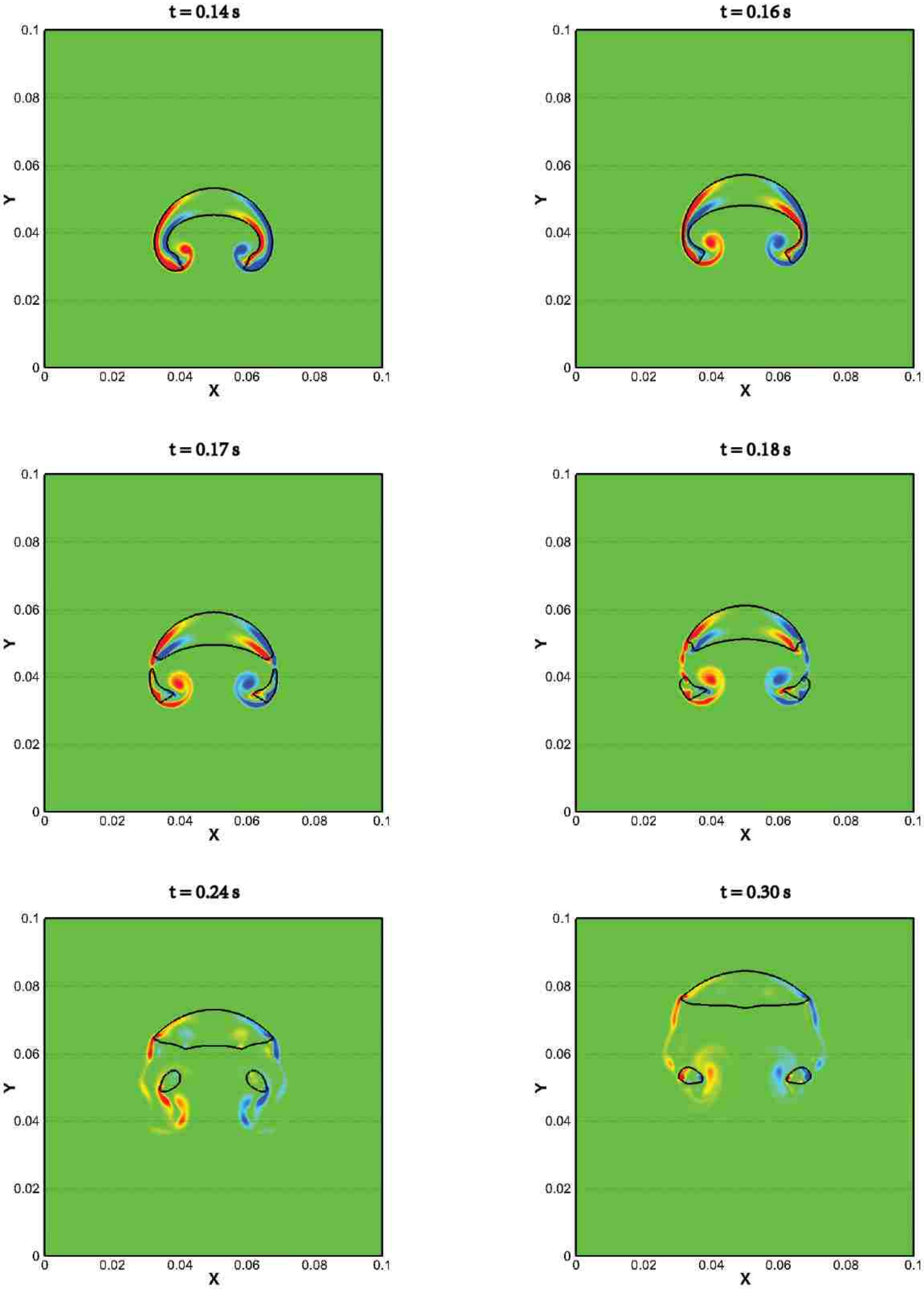

Figure 13 Vorticity contour at various time steps for ρ ratio = 10.

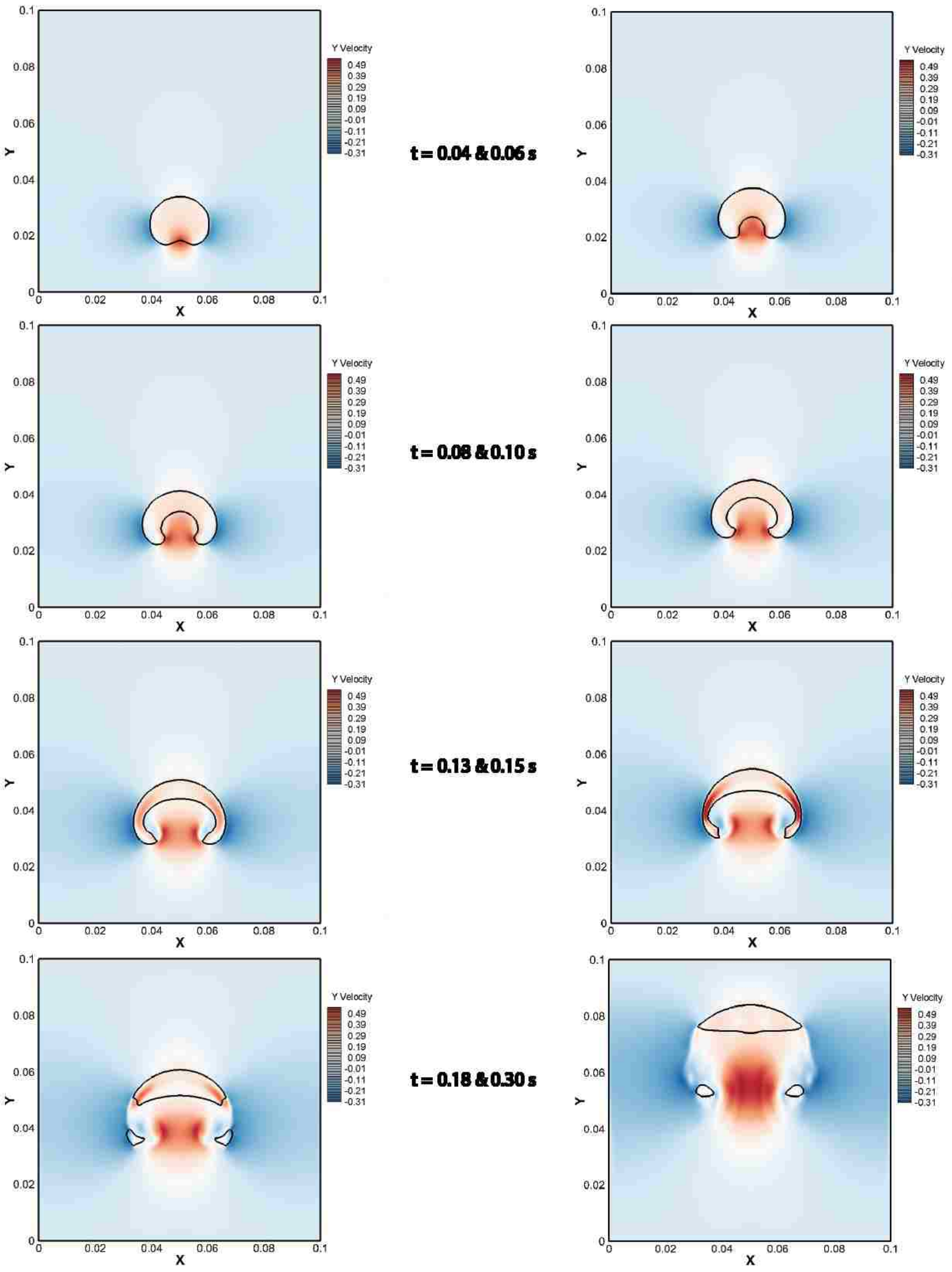

Figure 14 Streamwise velocity contour at various time steps for ρ ratio = 10.

If the density ratio is changed to 1000, the gas bubble starts to lose volume after limited time steps. The mass of the bubble diffused into the denser surrounding liquid due to the high diffusion across the interface. A finer mesh is used to reduce the interface thickness and the diffusion is constrained within the thinner interface. Instead of using the second order upwind scheme, the 5th order WENO method is implemented to reconstruct the velocity field and ensures an accurate advection of the level set function. Also, the level set function is reinitialized at a higher frequency, from every 10 time steps to 5. Figure 15 shows the comparison for a conserved and non-conserved gas bubble at different time.

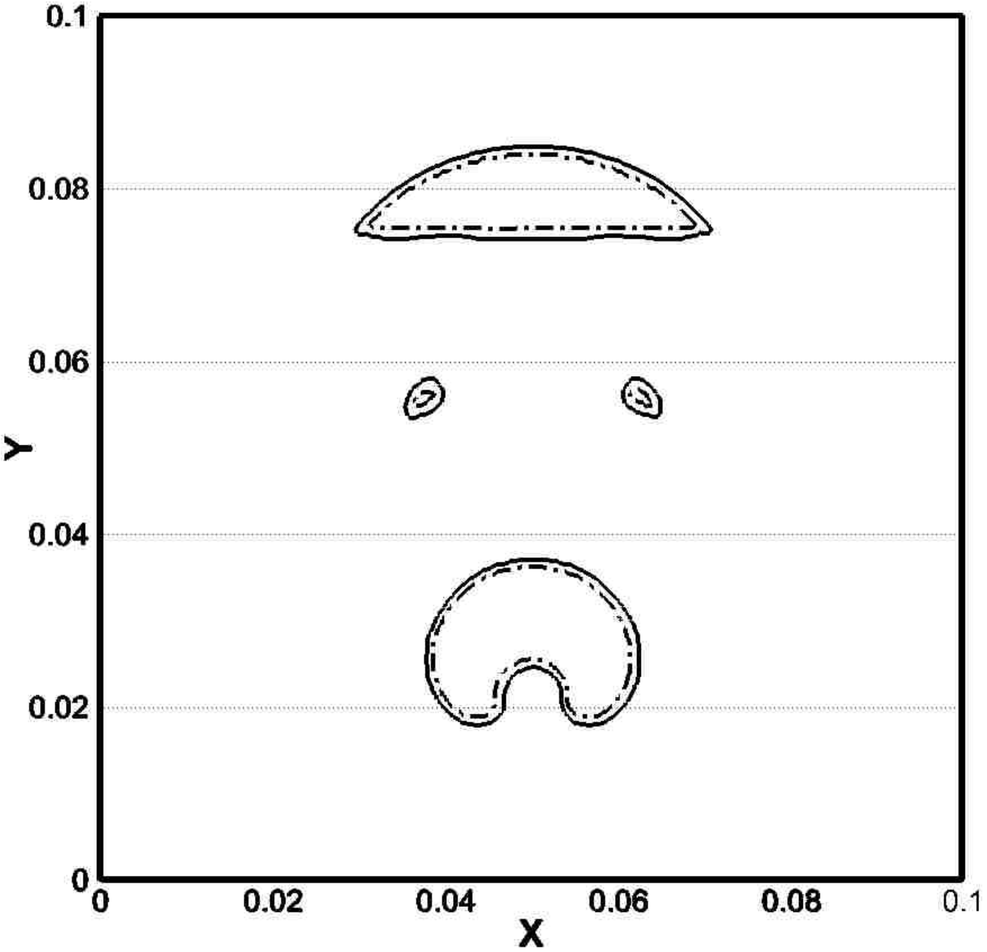

Figure 15 Conserved and non-conserved gas bubble for high density ratio at t = 0.05 s and t = 0.29 s

The dashed dot lines in Figure 15 represent the shapes and locations of non-conserved gas bubble. During the simulation, the bubble lost about 10 percent of the volume, which diffused into the surrounding fluid. The mass conserved bubble is portrayed by the solid lines. Figure 16 shows the history of the mass for conserved and non-conserved gas bubble.

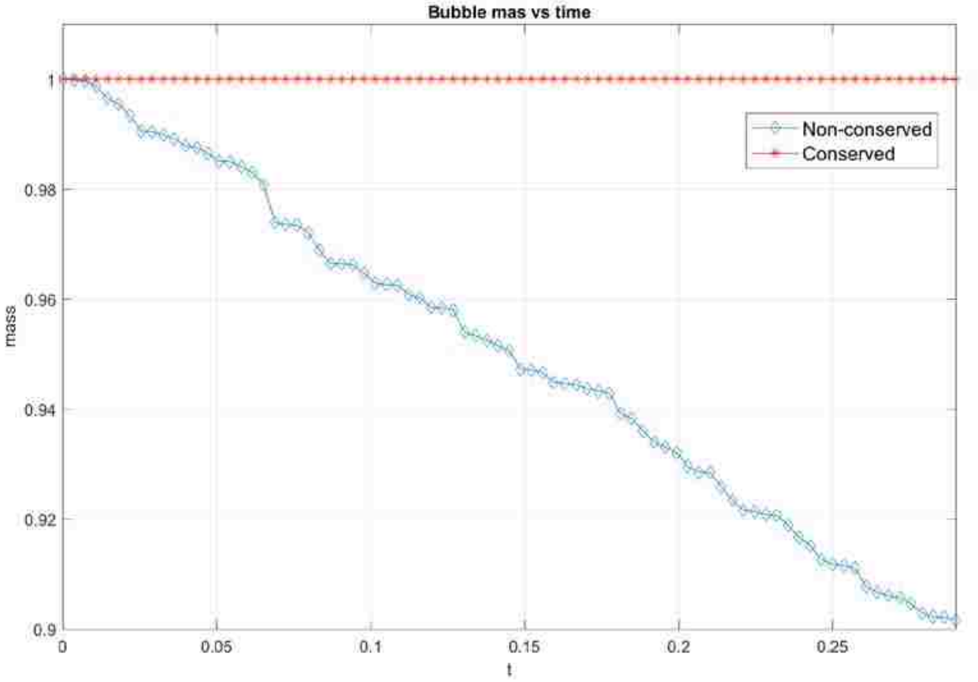

Figure 16 Mass conservation for bubble vs time

A slightly different sequence of shapes is observed when the bubble ascends in a denser fluid. A higher density does not significantly affect the shape of the bubble. However, with a stronger jet flow from the lower surface the bubble, the bubble moves faster and the smaller bubble separated from the larger one at an earlier time. The bubble shape and position history are shown in the right column of Figure 17.

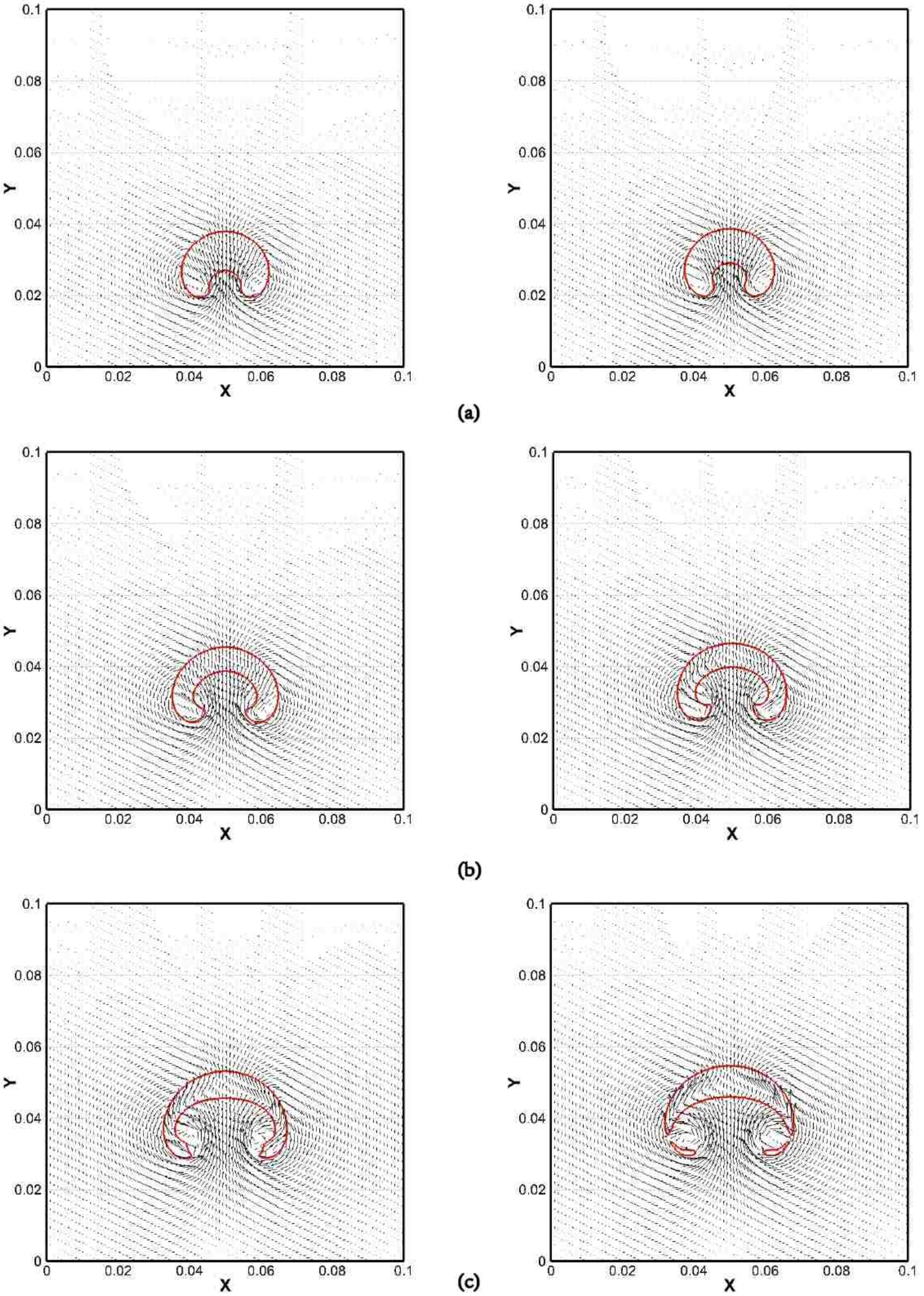

Figure 17 Bubble shape history comparison between the density ratio = 10 (left column) and the density ratio = 1000 (right column). (a) t = 0.06 s, (b) t =0.10 s, (c) t = 0.14 s

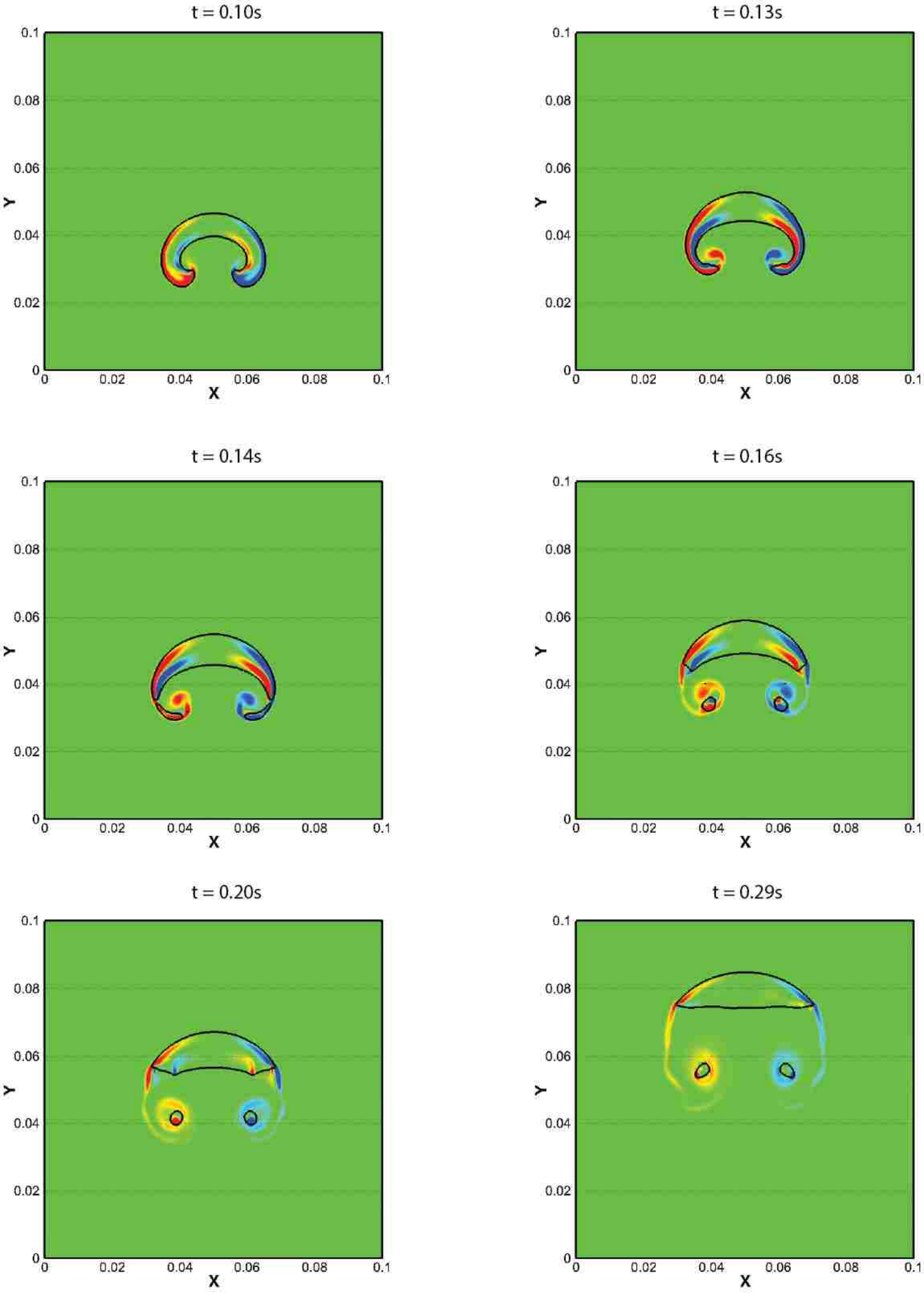
t = 0.10s
t = 0.13s
t = 0.14s
t = 0.16s
t = 0.20s
t = 0.29s

Figure 18 Vorticity contour at various time for the density ratio = 1000.

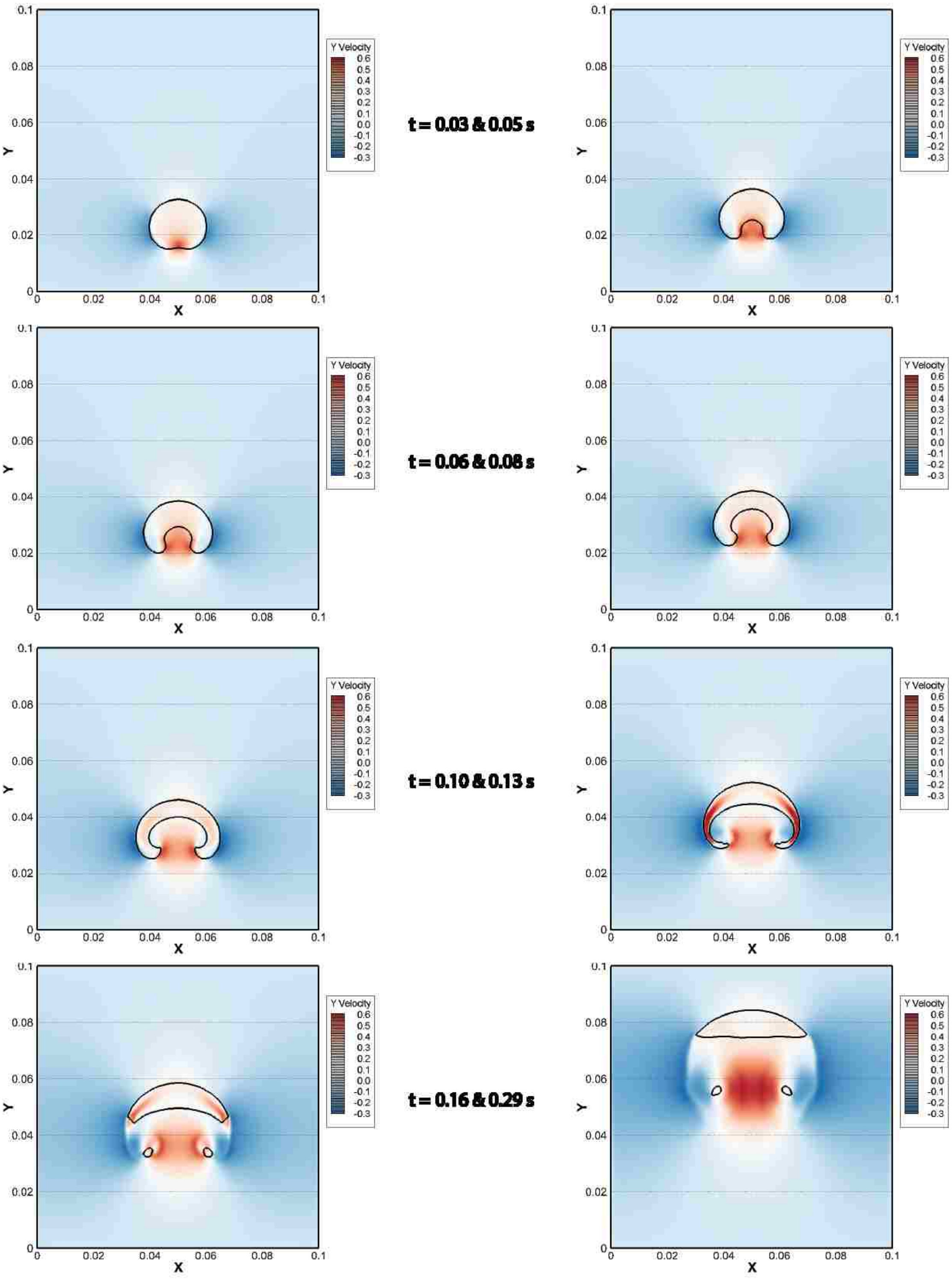

Figure 19 Streamwise velocity contour at various time for the density ratio = 1000.

In Figure 17 (a), a larger deformation is observed for the lighter bubble in the right column for t = 0.06 second. As the bubble rising upwards, the skirt of the lighter bubble is curling rapidly inside and separated from the bubble about 0.03 seconds earlier than the denser bubble shown in the right column. The denser bubble could maintain the skirt for a longer time before it was pierced.

4.2.3 Liquid droplet

When the fluid inside the circular region is heavier, the motion is reversed and driven by the gravitational field. Hence, a liquid droplet is formed under this situation. For each density ratio setup, the liquid droplet and gas bubble exhibit totally different dynamics, comparing to the gas bubble. In the same confined region, the droplets reached to the upstream boundary faster than the bubbles did. Contrary to what have been observed for the deformation of gas bubbles, the liquid droplets will easily deform at a low-density ratio environment.

The droplet shape history shown in Figure 22 and Figure 25 demonstrated the influence of the density onto the droplet deformation. In comparison, the droplet density is maintained same as the liquid water and the fluid surrounding the water droplet are set to 10 and 0.1 percent of the water density. In Figure 22, the water droplet is descending in a heavier fluid, comparing to the fluid in Figure 25. Combined with the streamwise component of the velocity in Figure 24, the deformation of the droplet started from its upper surface, where a jet flow is observed. The jet stream grows wider and stronger as time progresses. If the water droplet presents in a much lighter fluid, where the density ratio is dramatically increased from 10 to 1000, the droplet shows a different behavior in shape evolution, as well as the flow dynamics in Figure 25 and Figure 27. Instead of being depressed and expanded laterally, the droplet is elongated streamwise direction by the gravity.

Figure 23 shows the evolution of vorticity field generated by the droplet movement. After the droplet is released and pulled downwards by the gravity, the lighter fluid surrounding the droplet is pushed away and starts to circulate at the back. As the droplet continued evolving, vortical structure is observed to be entrained downstream fluid and bring it upstream to impinge on the back of the droplet, as shown in Figure 23. The counter rotating vortex, as shown in Figure 20, is formed from the forehead of the droplet. Along the indented surface of the droplet, a vortex rotating the clock-wise direction is also generated. These two counter rotating vorticity interact to form the wake recirculation region, which is attached to the droplet. The wake recirculation region persists through the droplet deformation and appears to contribute to the lateral-stretching mechanism.

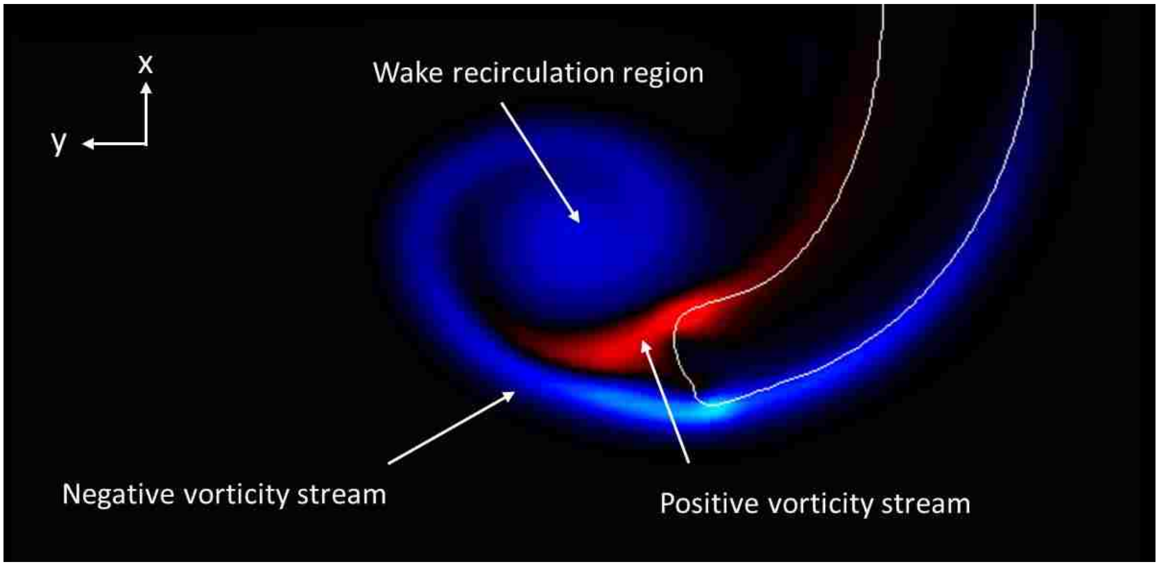

Figure 20 Vorticity contour near wake region for droplet at t = 0.13 second.

Similarly, the evolution vorticity field for the droplet descending in a lighter fluid is depicted in Figure 26. Two counter-rotating vorticity are also observed. The clock-wise rotating vortex is much weaker and not interacting with the counter clock-wise rotating vortex. The counter clockwise rotating vortex starting from the forehead of the droplet is extensively stretched further downstream.

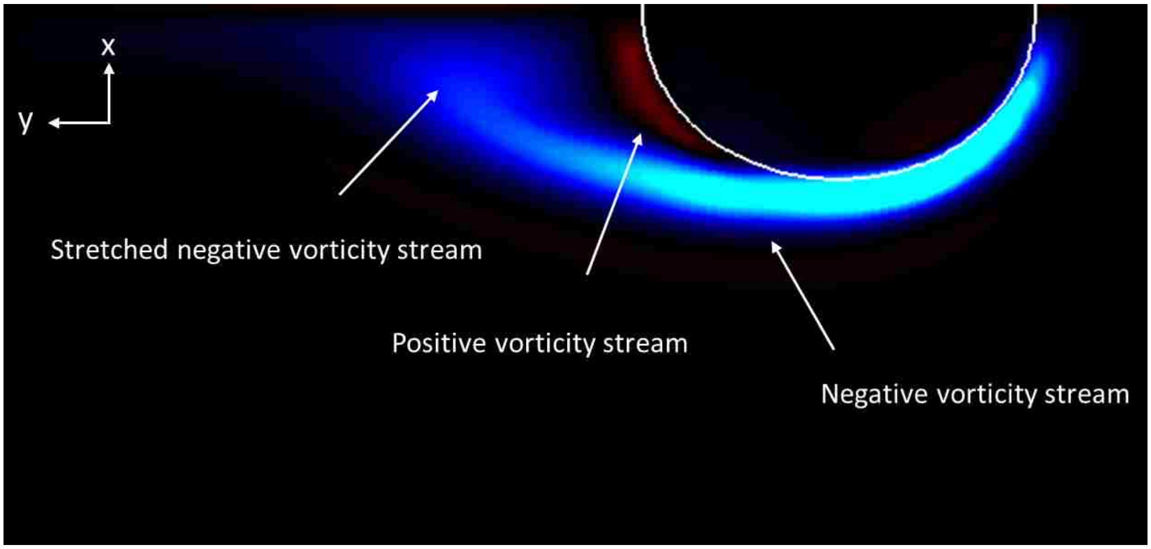

Figure 21 Vorticity contour near wake region for droplet at t = 0.10 second

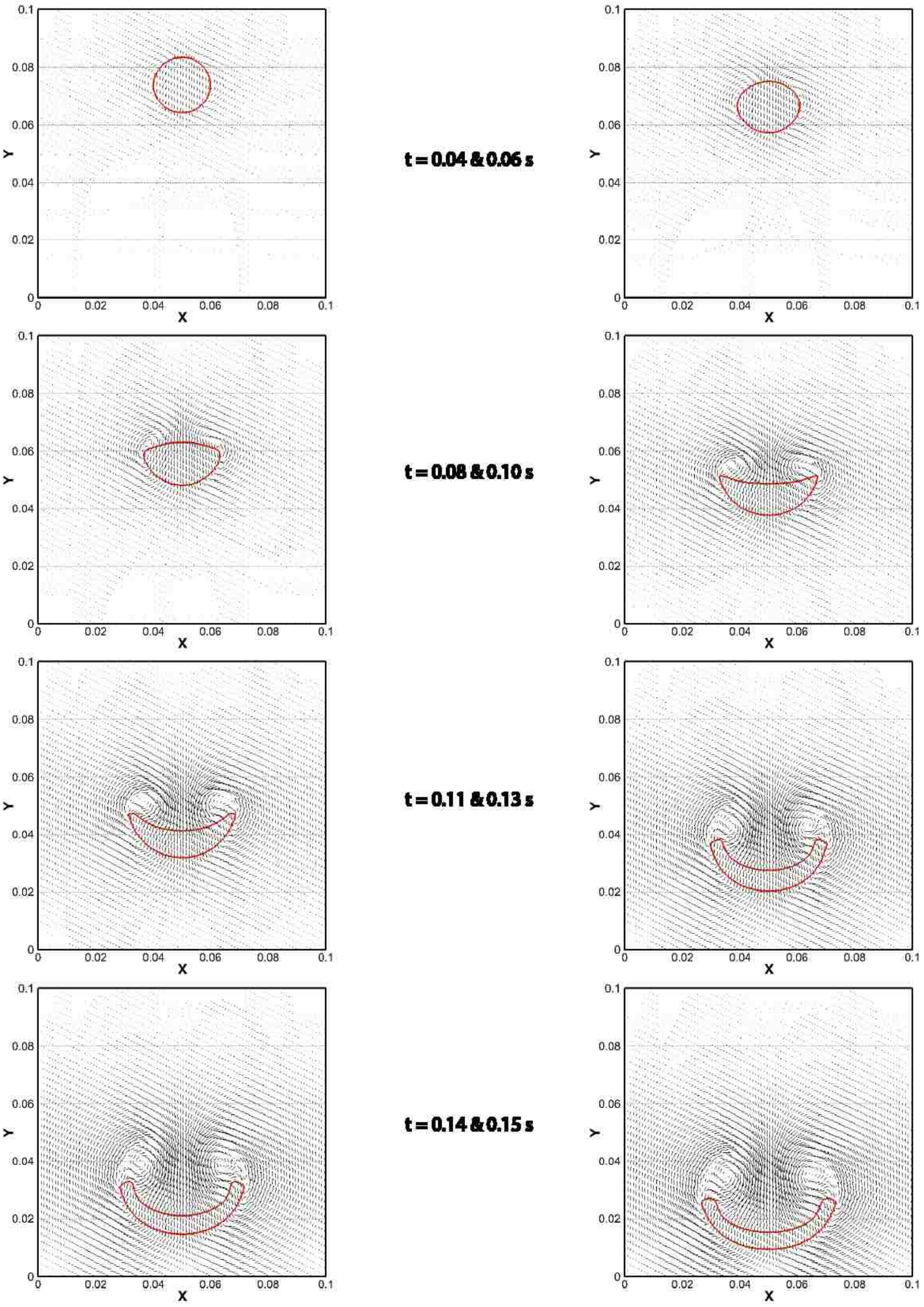

Figure 22 Droplet shape history for the density ratio = 10.

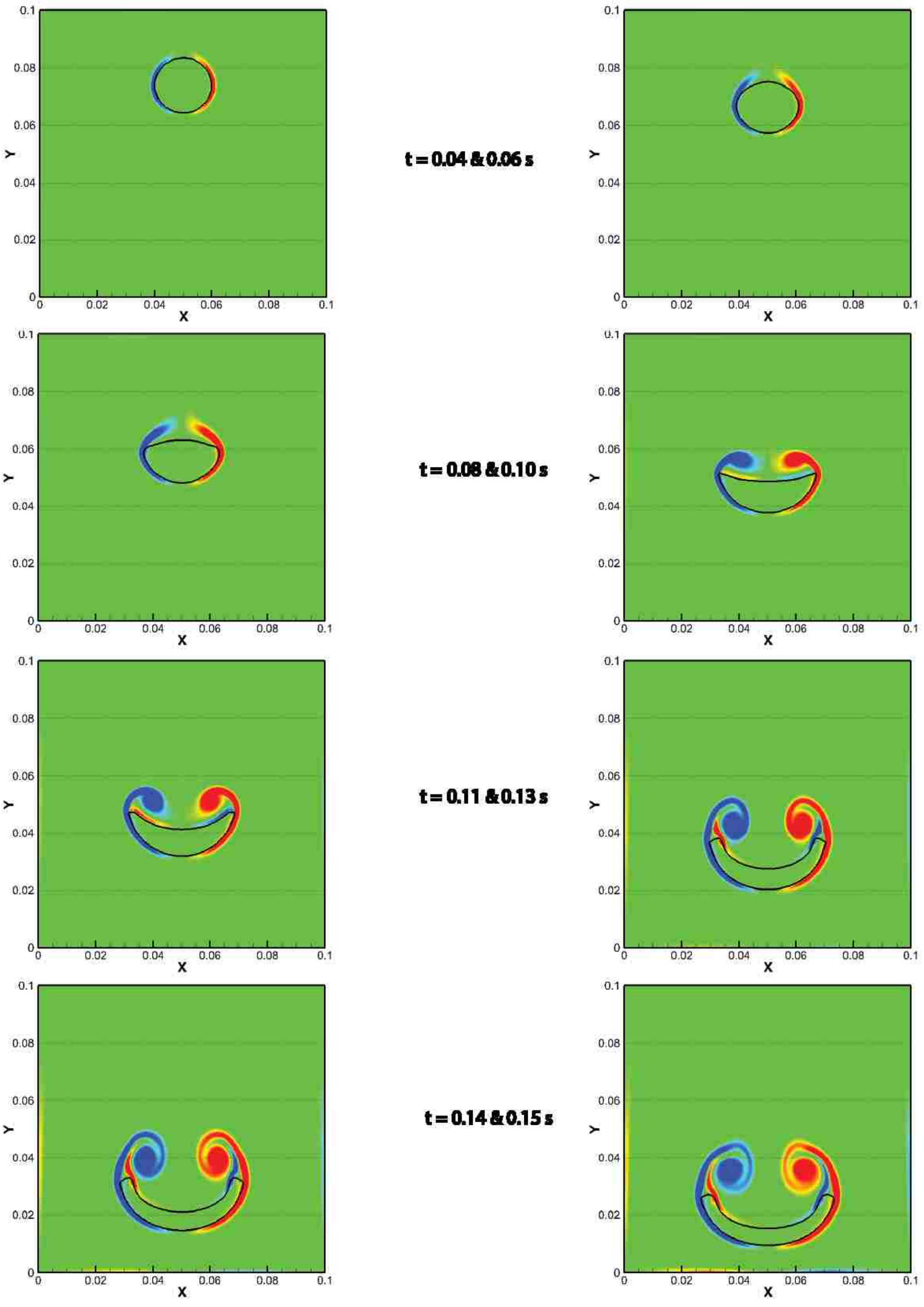

Figure 23 Vorticity contour of liquid droplet at various time for the density ratio = 10.

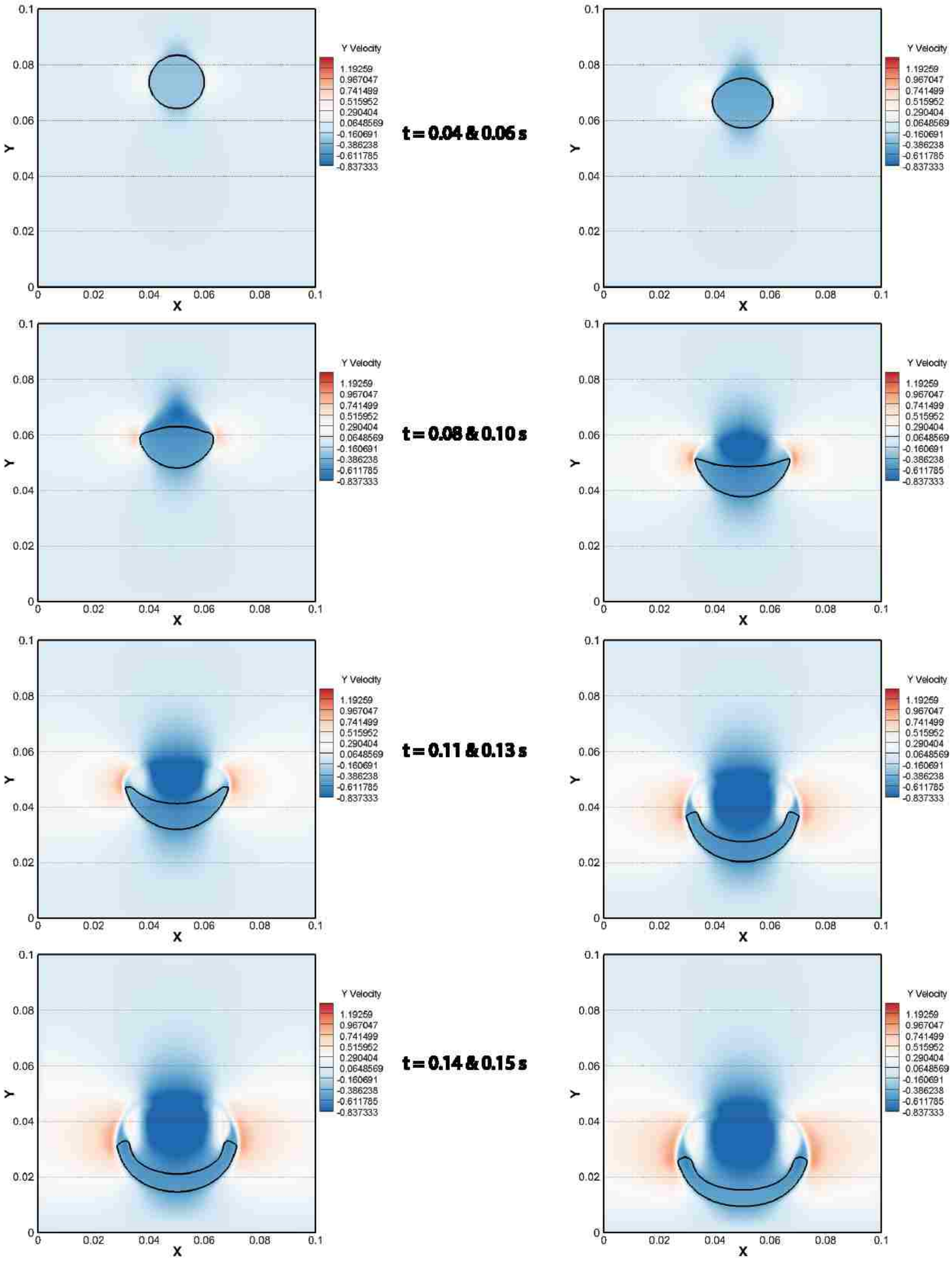

Figure 24 Streamwise velocity contour at various time steps for the density ratio = 10

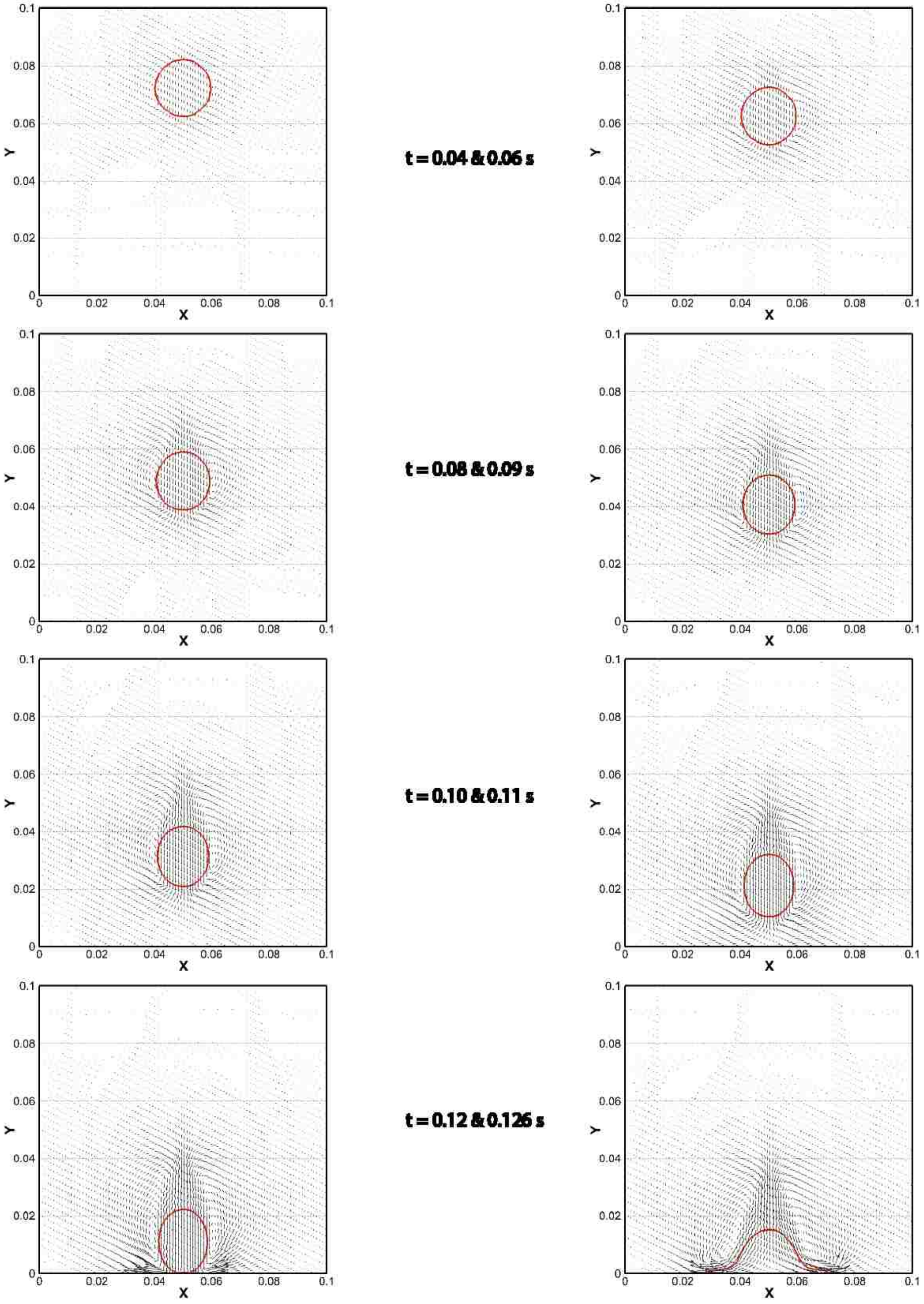

Figure 25 Droplet shape history for the density ratio = 1000.

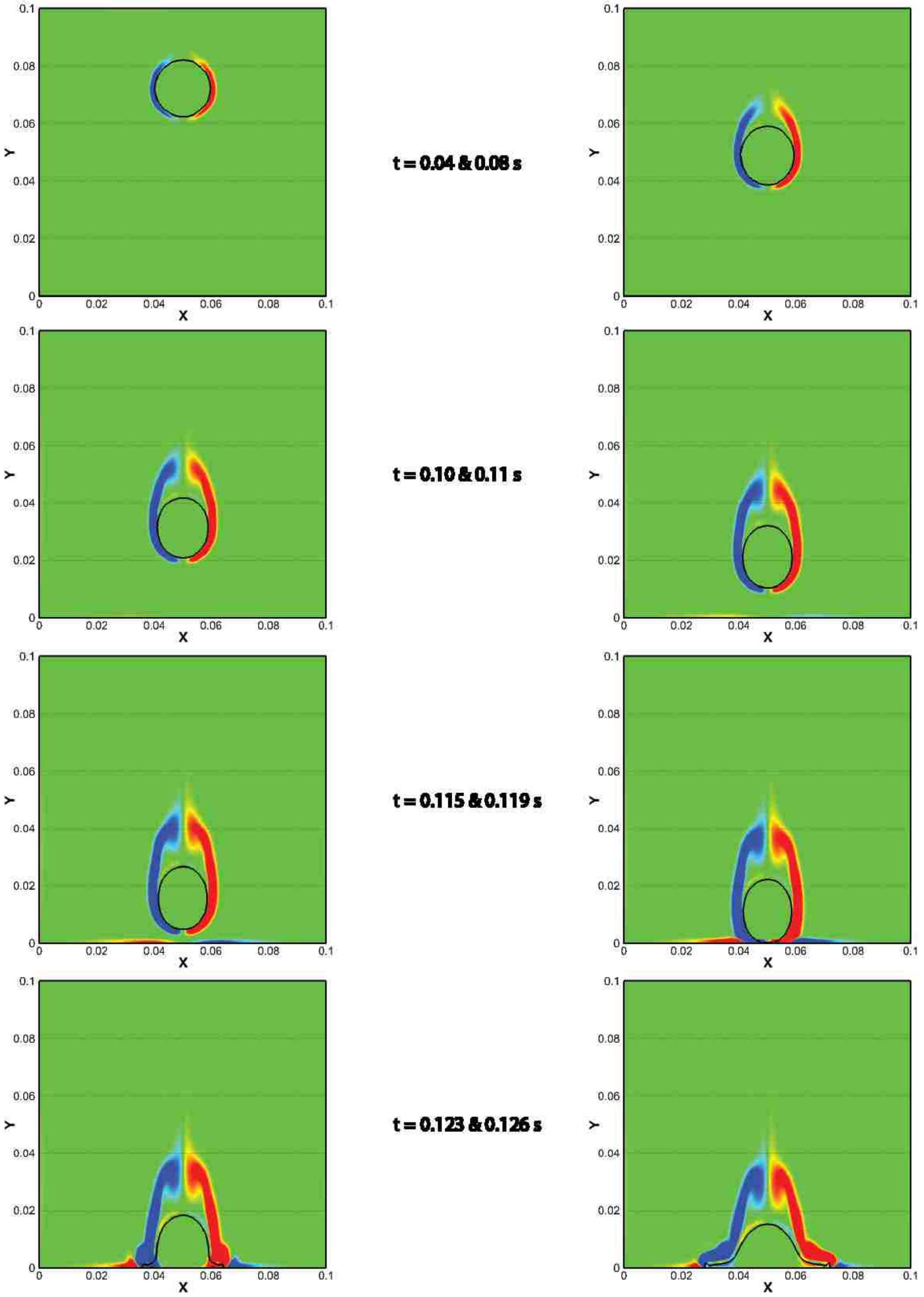

Figure 26 Vorticity contours around the droplet at various time for the density ratio = 1000.

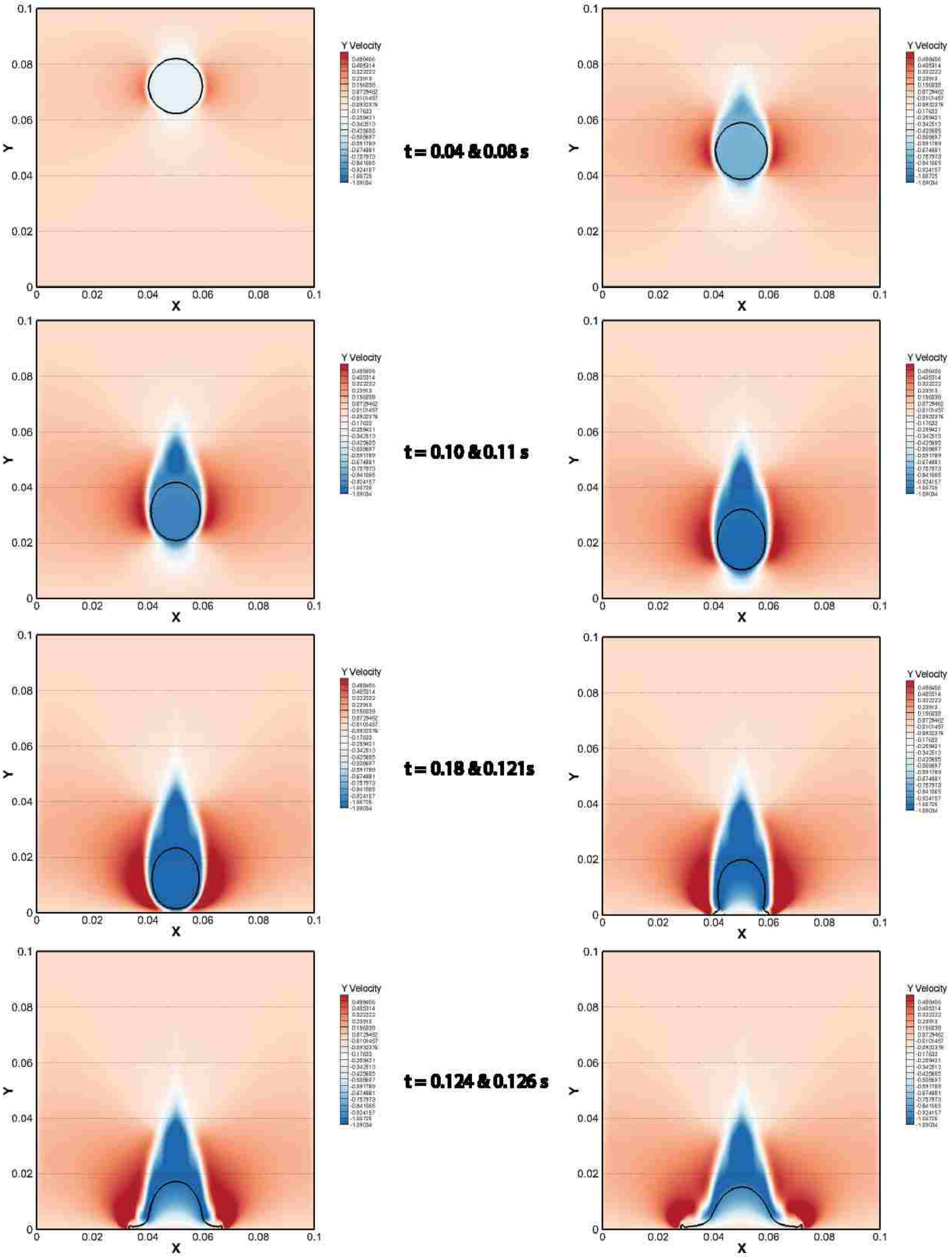

Figure 27 Streamwise velocity contour of droplet at various time for the density ratio = 1000

4.2.4 Effect of a surface tension

Studying interfacial flows, the surface tension needs to be modelled properly to represent the forces acting the interface for the Eulerian-based computational algorithm. Brackbill et at introduced the continuum surface force (CSF) model which incorporate the effect of the surface tension into the momentum equation[15]. The CSF model has successfully addressed a large variety of flow problems. However, when the surface tension strength increases to a magnitude, the CSF model will generate a parasitic current which may affect the flow field. Lafaurite et al carried out a series of numerical experiments and pointed out these spurious currents scale with the inverse of the capillary number[23]. Scardovelli and Zaleski proposed that the large currents may occur due to the dominance of surface tension over the inertial forces[24]. Harvie et al[25] presented a correlation to quantify the parasitic current in VOF simulations by using Vincent's method in implementing the CSF model[26]. When the Laplace number $La = \sigma \rho r / \mu^2$ is larger than 10^6, which is equivalent to a 1 cm water droplet in air, the spurious currents is needed to be addressed. Figure 28 represents a typical parasitic flow around a static water droplet[27] and the currents are clearly visible.

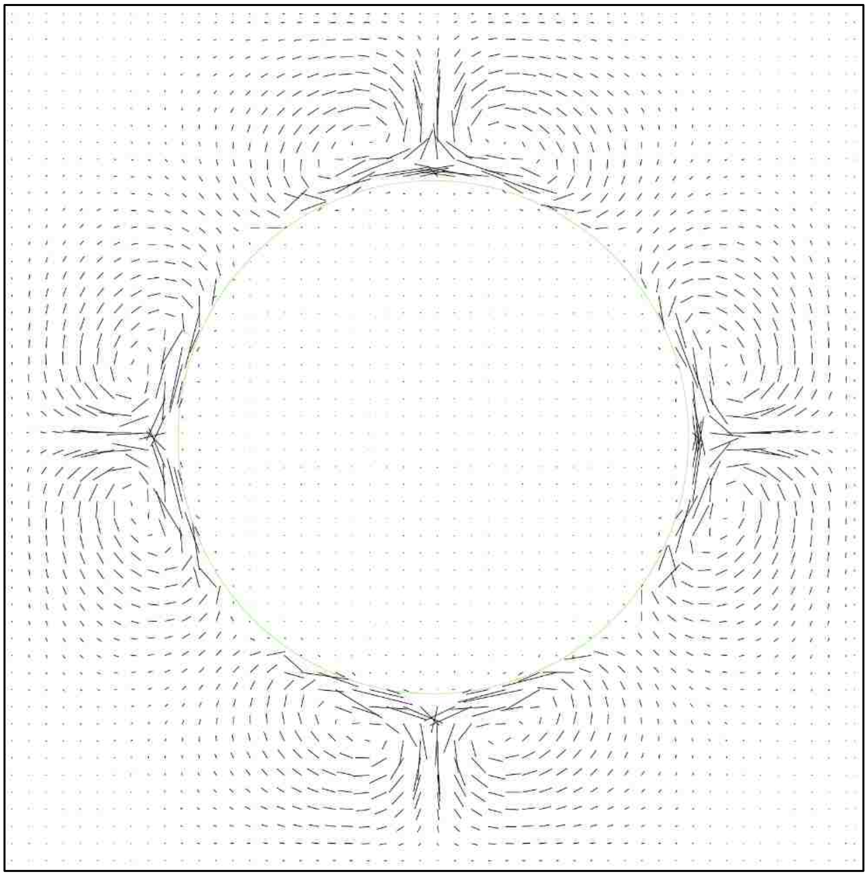

Figure 28 Illustration of parasitic flow surrounding a static bubble.

These spurious currents are mainly caused by two sources: inconsistent discretization of the surface tension force & the pressure gradient and inaccurate approximation of the curvature. Many researchers have presented various modifications on the CSF model to decrease the parasitic flow magnitude[28–31]. In our study, we implement the method proposed by Sussman et al [14] in conjunction with the balanced force discretization mentioned by Meland in [27]. Also, the approximation to the curvature is diverted by finding it at point of the interface corresponding to the discretization point, instead of the smeared region by regular CSF model implementation. In 2D, the curvature at the interface is given by

$$\kappa_0 \approx \frac{1}{1/\kappa - \phi} \tag{62}$$

where

$$\kappa = \frac{\phi_{yy}\phi_x^2 - 2\phi_x\phi_y\phi_{xy} + \phi_{xx}\phi_y^2}{\left(\phi_x^2 + \phi_y^2\right)^{3/2}}$$

as the level set curves can be treated locally as concentric circles. Since there are two independent principal radii of the curvature in 3D, the method in 2D will not work. Instead, the curvature is calculated in a narrow region of the interface by solving the following hyperbolic equation

$$\frac{\partial \kappa_{ex}}{\partial t} + sgn(\phi)\mathbf{n} \cdot \nabla \kappa_{ex} = 0 \tag{63}$$

with the initial condition $\kappa_{ex}(t = 0) = \kappa$ to the steady state. The solved κ_{ex} is used for the surface tension calculation. With the velocity vector fields in Figure 12, Figure 22 and Figure 25, the magnitude of the parasitic flow is minimized and no spurious current is captured.

The surface tension allows the fluid surface to acquire the least possible surface area and hold its shape at a static state if no other force is presented. In the dynamics of rising bubble or falling droplet, the presence of gravity field significantly deformed the fluid interface under the same surface tension coefficient. The surface tension is usually not strong enough to maintain the shape. However, with an increased surface tension strength, its effect can be captured obviously. The effects of surface tension are studied for the water droplet free falling in a fluid whose density is 10 times less dense than water. Two different surface tension coefficients are used in the numerical experiments.

Table 3 Physical properties for surface tension experiment

Case	ρ_1	μ_1	g	σ	Re	Eo	ρ_1/ρ_2	μ_1/μ_2
1	998.2	1E-3	9.8	0.078	8838	45	10	10
2	998.2	1E-3		0.78		5		

The shape of the droplets with different surface tension coefficient is compared at various instance. Figure 29 (a) and (b) depict the shape history for low and high surface tension, respectively. The time sequence shows that the droplet with high surface tension descends faster than the one with low surface tension. The cause is due to the larger drag acting on the stretched droplet with low surface tension.

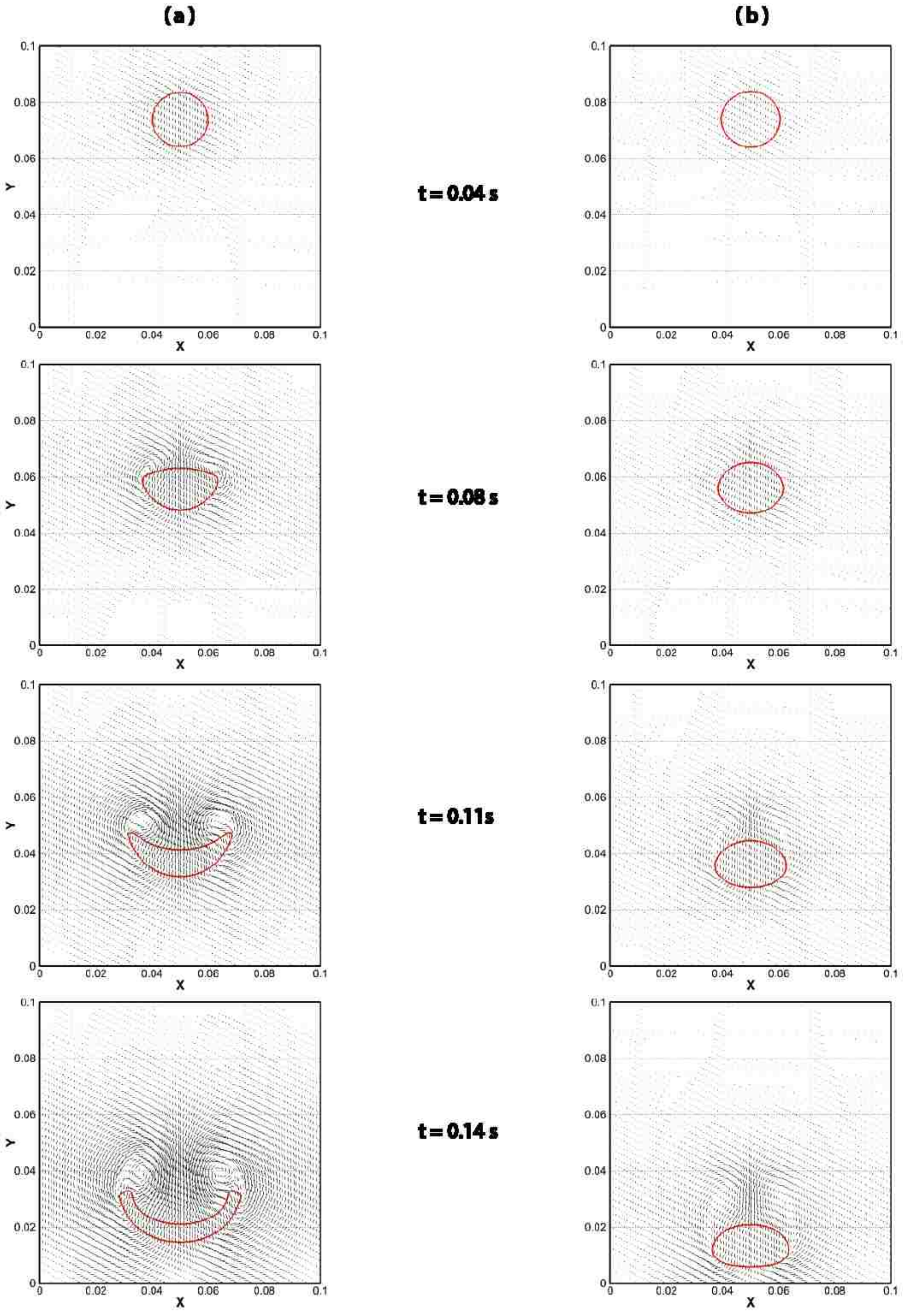

Figure 29 Droplet shape history comparison for different surface tension coefficient. Image on the left column is for low surface tension effect; image on the right is for high surface tension effect.

4.3 Multiphase-Merging

When multiple bubbles are in the same space, a more complicated dynamic is presented. As bubbles moving, they may collide and merge into a lager bubble. The collision and merging process involves two steps. Firstly, the interface is allowed to rupture on contact with another interface of the same fluid. Secondly, the two bubbles will merge together and new interface is formed. To accurately simulate the bubble merging process, the challenge to the numerical algorithm is to capture the interfacial structures during the topological transition. To ease the numerical simulation and have a better convergence of the solution, a finer mesh is applied. Also, the smoothing parameter, ϵ, is adjusted to 2.5 times of the gird size. For the following two examples, the interaction of two gas bubbles with the same density driven by the buoyancy is computed. The density inside the two bubbles is equal to 1 and the density for the enclosed fluid is set as equal to 10. In the first example, the surface tension is ignored and set to zero. The effect of surface tension is considered in the second example. Other physical properties used in the two simulations are listed in Table 4.

Table 4 Physical properties for two bubble merging test case

Case	ρ_1	ρ_2	μ_1	μ_2	g	σ	Re	Eo
1	5	1	0.05	0.01	9.8	0	51	44
2	5	1	0.05	0.01		0.08		20

Initially, the fluid is at rest and the initial positions of the two bubbles correspond to two circles, represented by the zero level set. The upper bubble is centered at (0.5, 0.57) with radius 0.15. The lower bubble is centered at (0.5, 0.3) with radius 0.1.

In figure, the evolution of the two bubbles are plotted at time t = 0.02, 0.08, 0.10, 0.16, 0.18, 0.20, 0.22, 0.26 second. The lower surface of the bubbles move faster than the upper part. As time evolves, the small bubble residing in the lower portion the domain produces a jet and pushes the smaller bubble moving upward. In the wake of the larger bubble, we observed the similar counter rotating vortices form which is also observed in the single rising bubble. In this lower pressure region, the smaller bubble is deformed and becomes narrower and sharper. For time t = 0.18 s, the elongated smaller bubble reaches to the lower surface of the larger bubble. At t = 0.2 s, the interface of the two bubbles makes a contact and ruptures. The two bubbles merge into a single bubble. A sharp cusp singularity is formed by the interface conjunction and smoothed out the viscosity in time. The skirt of the large bubble rolls upward due to the counter rotating vorticity field. The jet starting from the lower surface of the small bubble tried penetrating through the stem of the newly merged bubble.

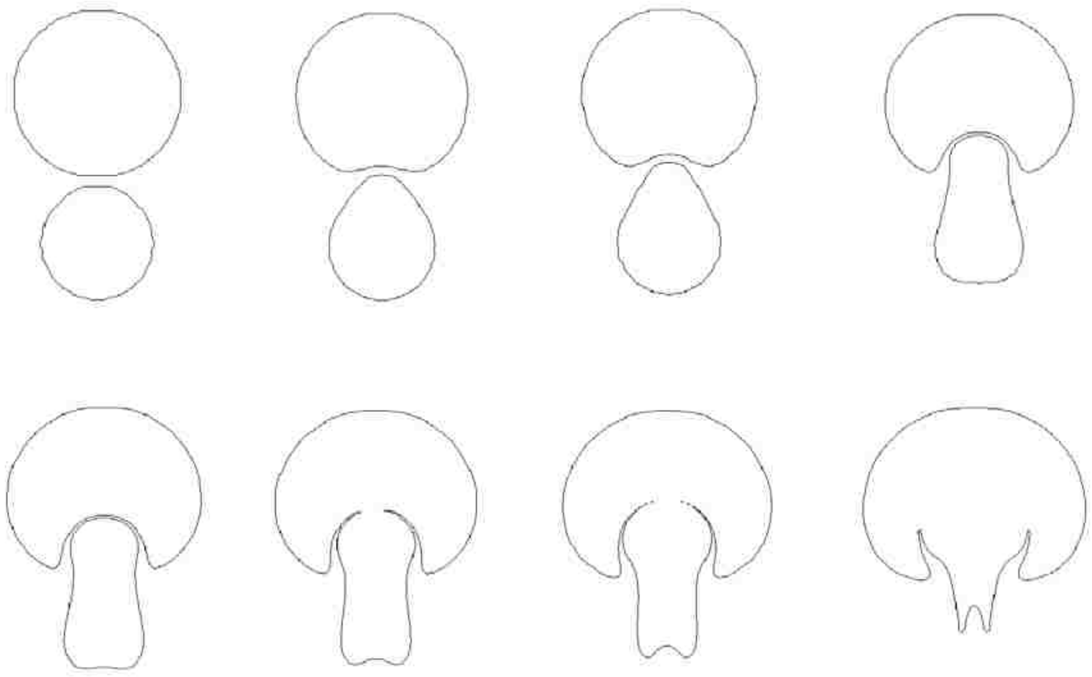

Figure 30 Shape evolution for gass bubble merging without surface tension.

Now, we include the surface tension into the simulation. The surface tension is set to be $\epsilon = 0.08$ and other parameters are remained the same. The results shown in Figure 31 indicates a longer time for the merging process when the surface tension presents. The two bubbles merge into a single bubble at time t = 0.22 s. The cusp singularity generated during the bubble merging is quickly smoothed out by the surface tension and the viscosity, shown at t = 0.26 s.

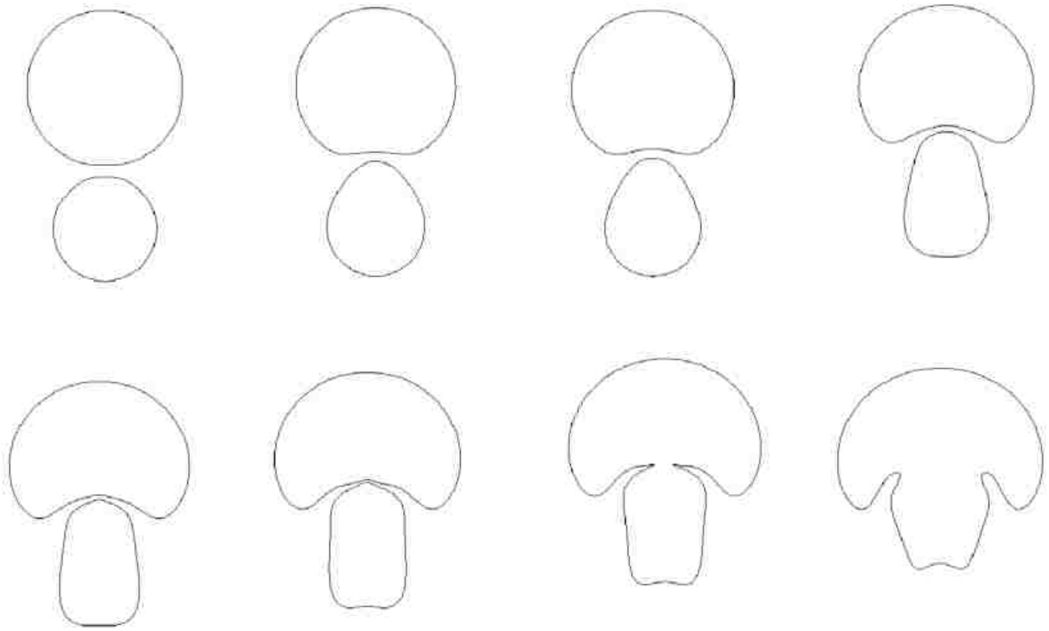

Figure 31 Shape evolution for gass bubble merging without surface tension.

We demonstrated that our proposed algorithm can handle complex phenomena such as coalesence, interface ruptures, interface contacts and resulting singulrities effectively.

4.4 Rayleigh-Bénard convection

Single layer Rayleigh-Bénard convection is one of the most studied transport system.. After Bénard's experimental results [1], the theoretical framework was presented by Lord Rayleigh in 1916 [2]. In Rayleigh's work, the system stability is characterized by a dimensionless number, Rayleigh number (Ra), which represents the ratio of buoyancy and viscous forces.

$$Ra = \frac{g\beta}{\nu\alpha}(T_s - T_\infty)d^3$$

where d is the characteristic length of the flow, g is the gravity acceleration, β is the thermal expansion coefficient, ν is the kinematic viscosity, α is the thermal diffusivity, and $T_s - T_\infty$ is the temperature gradient across the fluid in the direction of the gravitational acceleration. The heat is transported in the fluid by conduction when the Ra is below a certain critical value. The onset of the convection is set and the flow transition occurs when Rayleigh number exceeds the critical value. Above the critical value, the heat will be transported vby both conduction and convection. Many different methods emerged to investigate the onset of the flow transition and the secondary flows induced by the transition. Among those methods, the linear stability analysis is the most commonly used due to its simplicity. However, when the non-linear terms become strong in the system as the later stages of the flow transition are reached, the drawbacks of LSA studies will be emerged. For a single layer RB system, the critical Rayleigh number (Ra_c) and the associated critical wave number (α_c) can be defined through the linear stability analysis. According to Pellew and Southwell [32], the critical values for a single layer RB system are list in Table 5.

Table 5 Critical parameters for a single layer Rayleigh-Bénard convection

Boundary condition	Ra_c	α_c	λ_c
Rigid-rigid	1707.8	3.117	2.016
Rigid-free	1100.7	2.682	2.342
Free-free	657.5	2.221	2.828

When a second layer of fluid presents in the system, the complexity is drastically increased and influence of the second layer on the stability manifests itself so many different mechanisms, like the competition between convective modes in each layer and the dominance of the flow in one layer over in another. The problem of multiple layer convection is composed of density staratification as well as stratifications of other thermal properties. Many systems in nature are modeled with the multiple layers of convecting fluids. The earth mantle is modeled as a two-layer convecting system. There are several stable or unstable layers of air in atmosphere. These systems exhibit complex nonlinear dynamics involving competing instabilities and interfacial effects. From a basic science perspective, the multiple layer problems are more closely related to the behaviors in real world.

Instead of applying the linear instability analysis, which would only capture when the flow transition is onset, the direct numerical simulation is carried out to study the flow dynamics and heat transfer characteristics of the system. A schematic of the 2D system is shown in Figure 32. The 3D system can be established with a third dimension added into the space.

Figure 32 System schematic for two layer 2D Rayleigh Bénard convection system.

4.4.1 Critical Rayleigh number and wave number

As shown in Figure 32, the system is stratified by the two fluids with different physical properties, e.g. density, viscosity and thermal diffusivity. A constant vertical temperature gradient is applied to the system and our analysis is limited to the case $\Delta T > 0$. Like single layer system, the dominant heat transfer mechanism in the system with two immiscible fluid layers will change from the conduction to convection when the Rayleigh number is beyond the critical value. Although with a large number of theoretical studies and experiments on multiple layer convection [12,33–37], the critical Rayleigh number is not clearly defined as the single layer system for each layer. For the system in Figure 32, the interface between layers plays as a similar stress-free boundary in the single layer system. Therefore, a double layer convecting Rayleigh-Bénard system can be crudely treated as of two single layer systems with rigid-free boundary stitched together by the interface. For our numerical experiments, we can reference the critical Rayleigh number for the single layer system and setup the simulations beyond the critical value to observe the instabilities. Another fundamental feature of Rayleigh-Bénard convection is the critical wave number α_c, associated with the critical Rayleigh number. Experimental studies on wave number measurement is done by Luijkx and shows a decreased convective roll number with the increased temperature for the same aspect ratio [38]. The wave number selection for Rayleigh-Bénard convection in various aspect ratio is studied numerically [39,40]. Again, all these studies are performed with a single convecting layer setup. As stated above, we can reference the data for the single layer system by assuming the system being composed by two single convecting layers. The critical Rayleigh number, wave number and wave length obtained by linear stability analysis for different boundary conditions are listed in Table 5.

4.4.2 Air-Water double layer system

Historically, the free boundary in the Rayleigh-Bénard convection experiments is approximated by a thin air layer. However, air is has poor thermal conductivity, which made the theoretical boundary condition unrealistic. Our numerical experiments are inspired by this mismatch between the theoretical studies and real world experiments. Instead of eliminating the air layer, we extend the thickness of air and adjust the temperature difference imposed on the system. By manipulating the boundary conditions, the thin poorly conductive air layer is replaced by the convecting air layer. The bottom layer is filled with liquid water with the same height as air. The parameters used in the simulation is list in Table 6.

Table 6 Material properties fro air-water system.

Fluid	$\rho(kg/m^3)$	μ	g	$d(m)$	Ra	$L(m)$
1	1.225	1.789e-5	9.8	0.01	2205	0.06
2	998.2	1.002e-3		0.01	290877	

The whole domain is initialized by 293 K. The top non-slip boundary is constantly cooled at 293 K and bottom non-slip boundary is constantly heated at 313 K, with two isolated lateral walls. A sequence of contours for isotherm, u-velocity, v-velocity and streamline plots are depicted in *Figure 33*, Figure 34, Figure 35 and Figure 36. The isotherms in the first column of *Figure 33* show the interface temperature is maintained at 293 K and the Rayleigh number for the water is kept at 290877. The warmer water fluid starts to rise from the bottom boundary and forms the classic plume structures. Multiple small convection cells are observed in the water layer and the magnitude of velocity increases in time.. The interface temperature starts to increase when the first batch of plume structures reach the upper bound of water. The plume heads are spread laterally along the interface, which heat the contact area evenly. With more plume structures being generated, the rising warmer plumes merge with the falling cooler fluid and the movements of merged plumes quickly brings up the layer temperature. The smaller Bénard cells are being compressed and converted to larger cells together with the neighbor cells. The contours for u and v velocity components become much chaotic, following the merging process of the plumes structures. Although the Rayleigh number starts decreasing with the heated interface, it is still over the critical value and visible thin plume structures are captured. The Bénard cells are getting more regular following more orderly flow structures are observed. The cells are thought to be separated by path of rising warmer fluid and merged following the thermal diffusion effect.

In the air layer, the flow movement is balanced out by the diffusion term before the interface gets heated. The u and v velocity components show the flow is almost quiescent at early times. Contrary to the water layer, the Rayleigh number increases after the interface getting heated by the warmer water flow from below. Gradually, the buoyancy driven flow in the air layer overcomes the thermal diffusion effect when the temperature gradient is sufficiently large, and the temperature distribution is perturbed. Large and thick air plume structures emerge right above the interface. Comparing to flow characteristics in the water layer, the Rayleigh number for the air layer is significantly smaller and exhibit a more stable pattern of Benard convection cells. Similarly, the contours for u and v velocity components clearly reflect the movement of air plumes and fluid motions within the Bénard cells. At later instances, the evolution of the cells settles down, as shown in Figure 36. Although the size of the cell in the water layer changes, the number of cells in each layer converges. With the same aspect ratio for each layer, this is expected to have a matching in the number of cells. The wave number is calculated

$$\alpha = \frac{\pi}{L} N d$$

where N is number of cells, d and L are the depth and width of each fluid layer. Here we have the wave number 3.14 for each layer at t = 300 s.

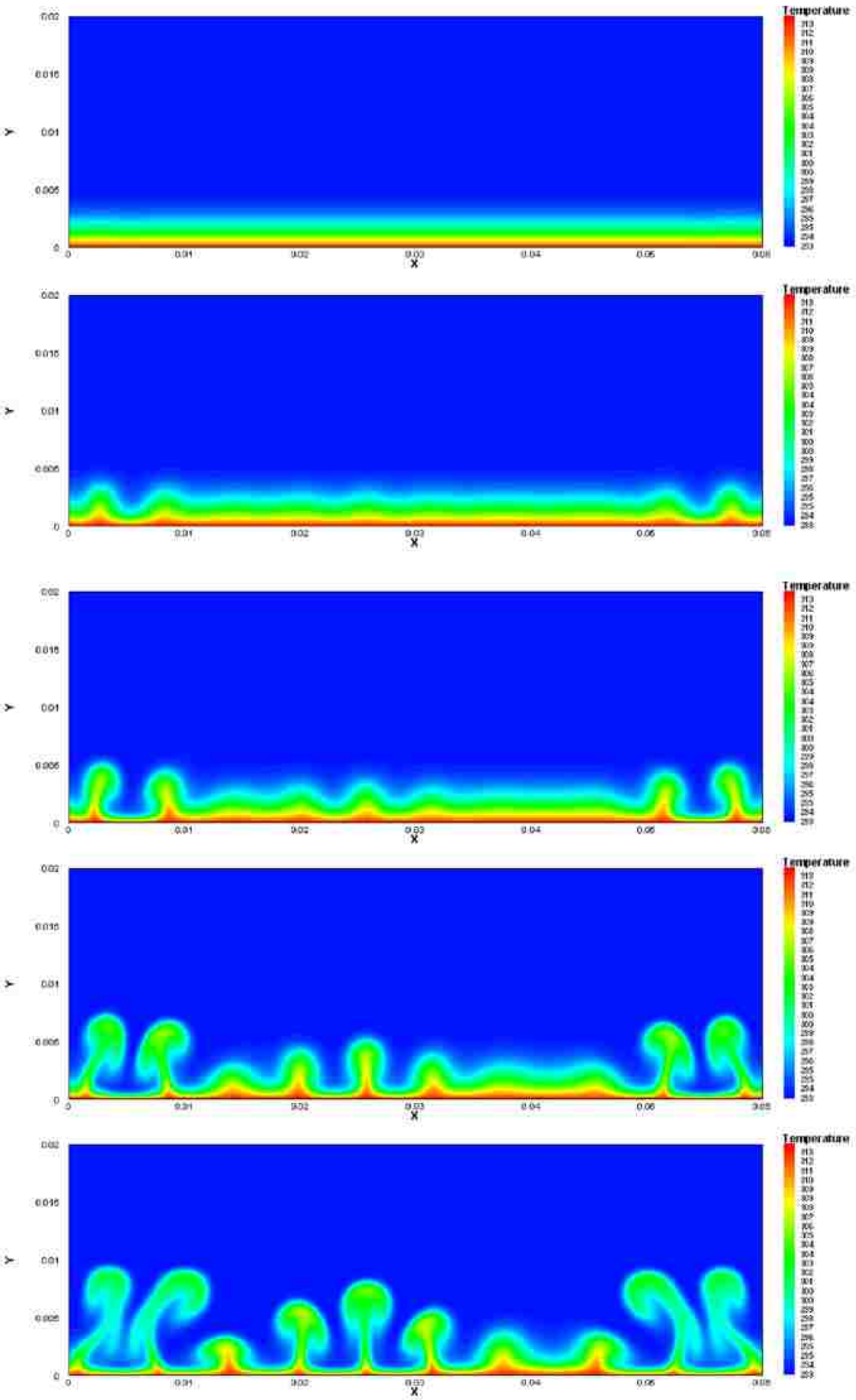

(a)

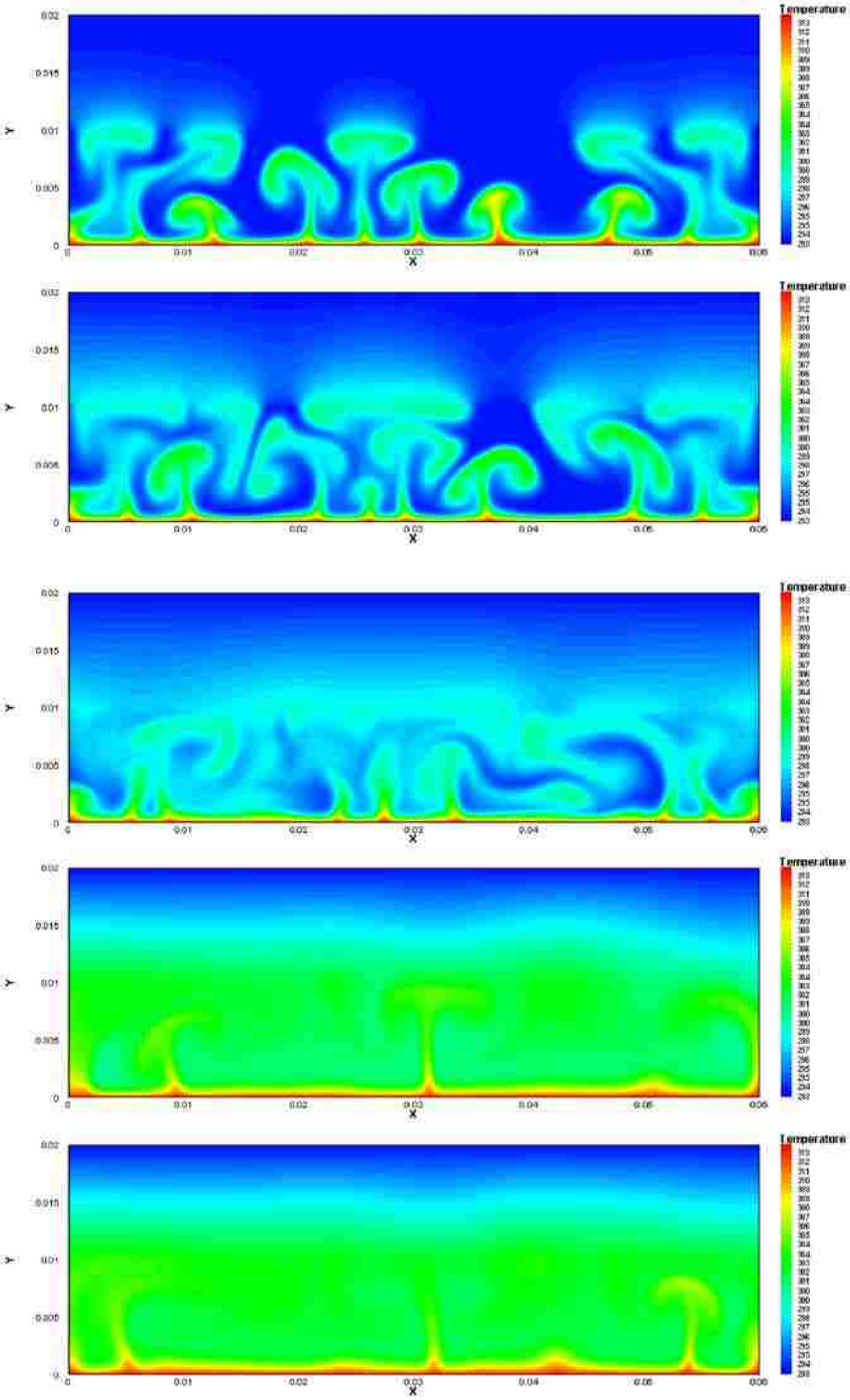

(b)

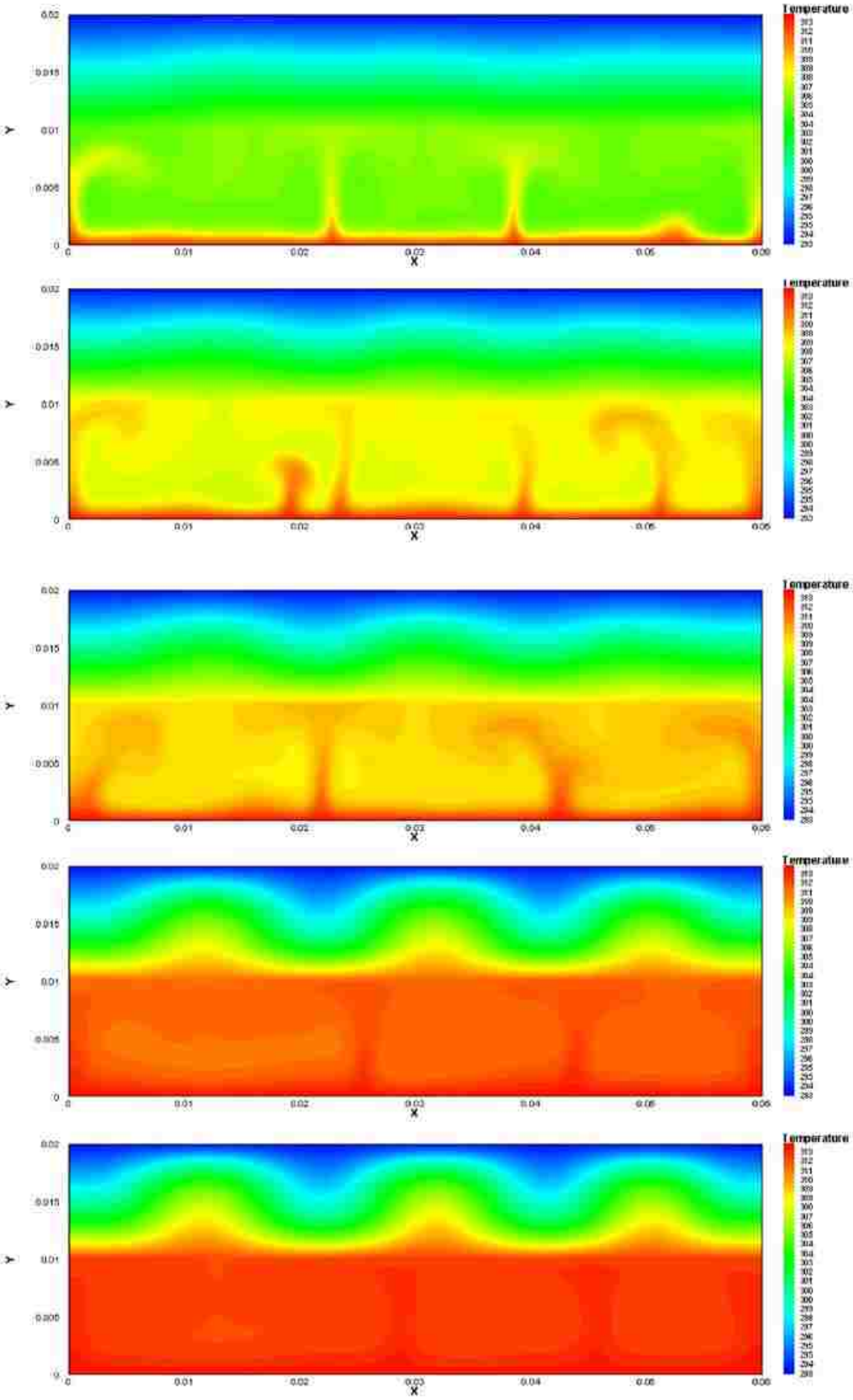

(c)

Figure 33 Isotherms for air-water system at various time. (a) t = 12, 13, 16, 17, 18 second; (b) t = 19, 20, 22, 45, 50 second; t = 75, 110, 130, 220, 300 second.

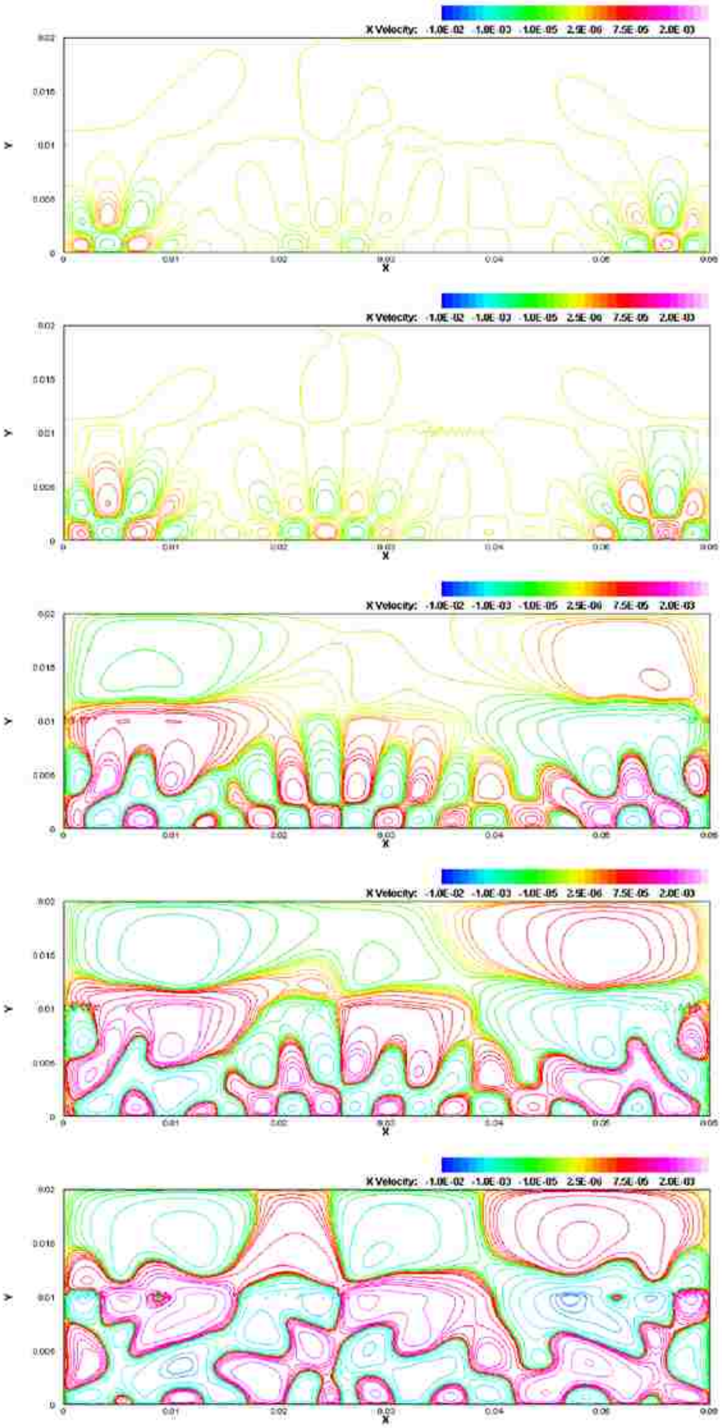
X Velocity: -1.0E-02 -1.0E-03 -1.0E-05 2.5E-06 7.5E-05 2.0E-03
Y
X
0
0.005
0.01
0.015
0.02
0.01
0.02
0.03
0.04
0.05
0.06

(a)

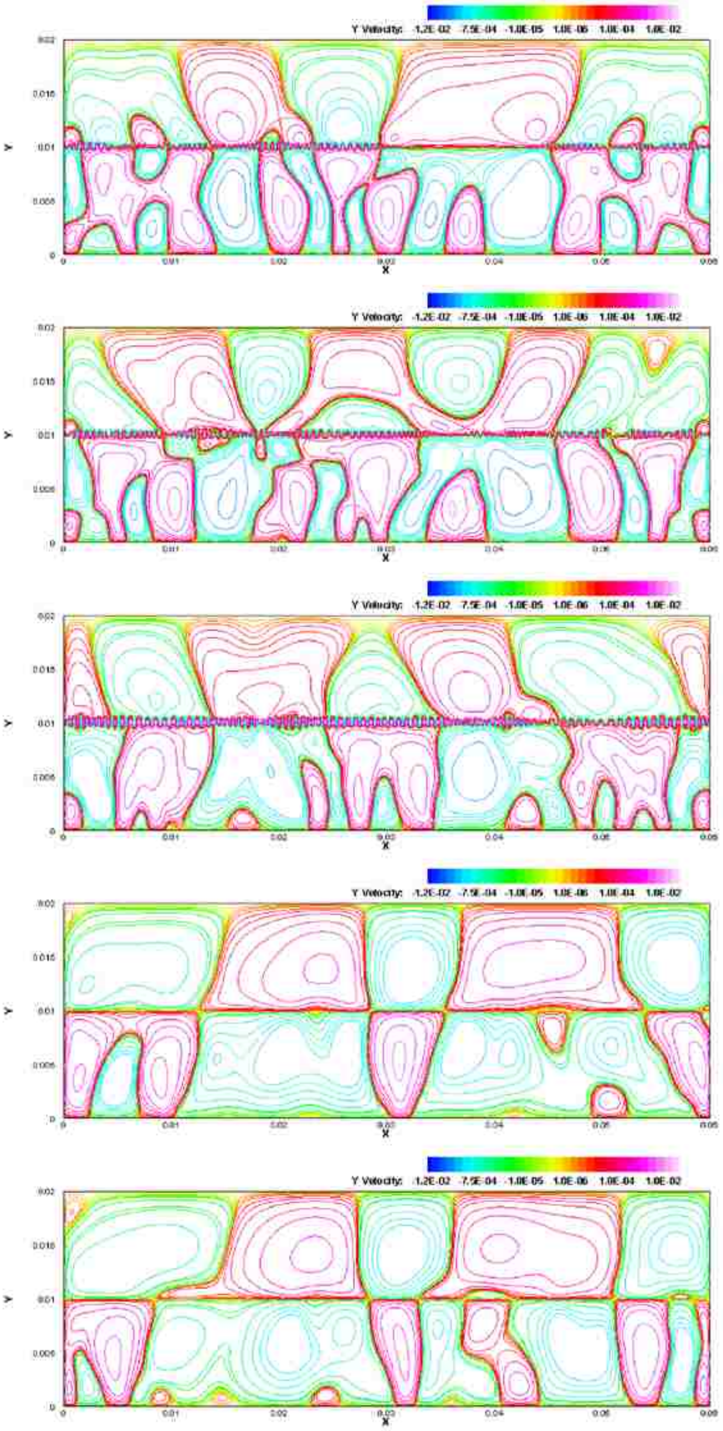
Y Velocity: -1.2E-02 -7.5E-04 -1.0E-05 1.0E-06 1.0E-04 1.0E-02
Y
0.02
0.015
0.01
0.005
0
X
0
0.01
0.02
0.03
0.04
0.05
0.06

(b)

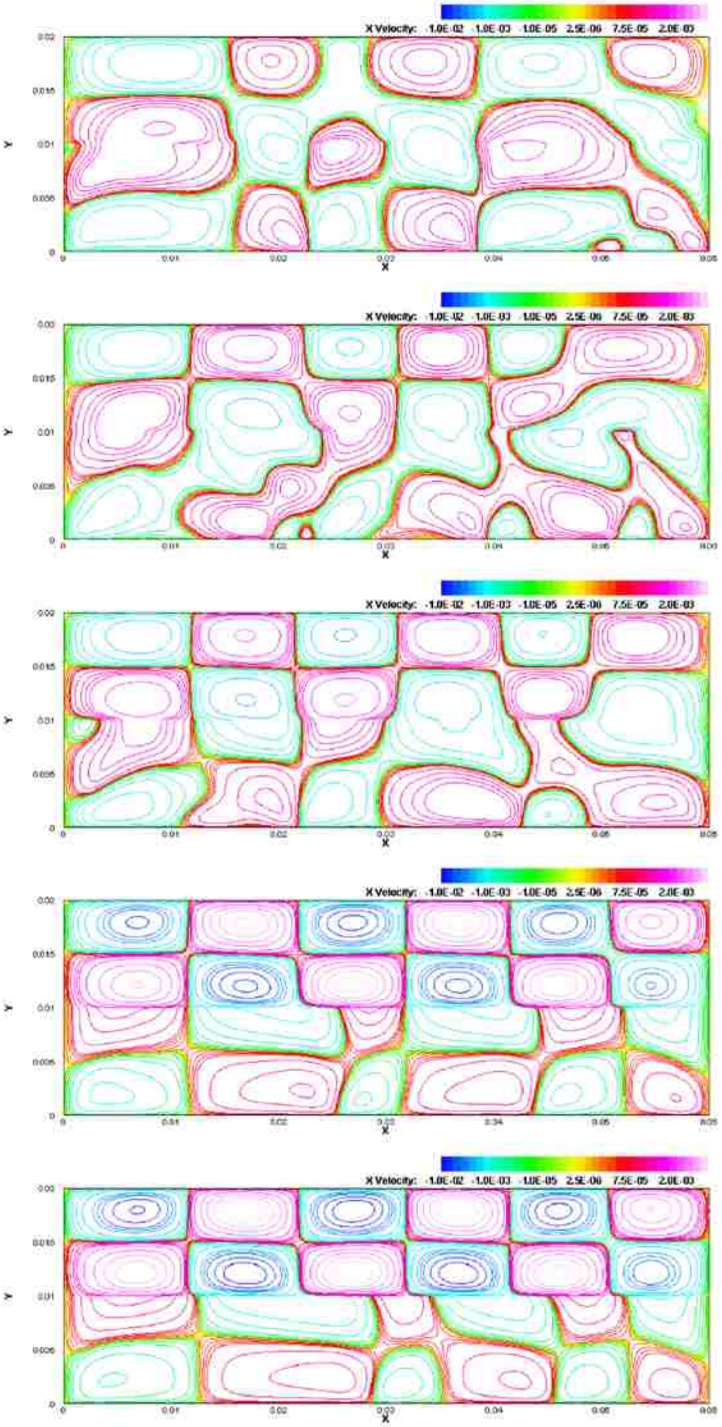

(c)

Figure 34 x-component of velocity contour for air-water system at various time. (a) t = 12, 13, 16, 17, 18 second; (b) t = 19, 20, 22, 45, 50 second; t = 75, 110, 130, 220, 300 second.

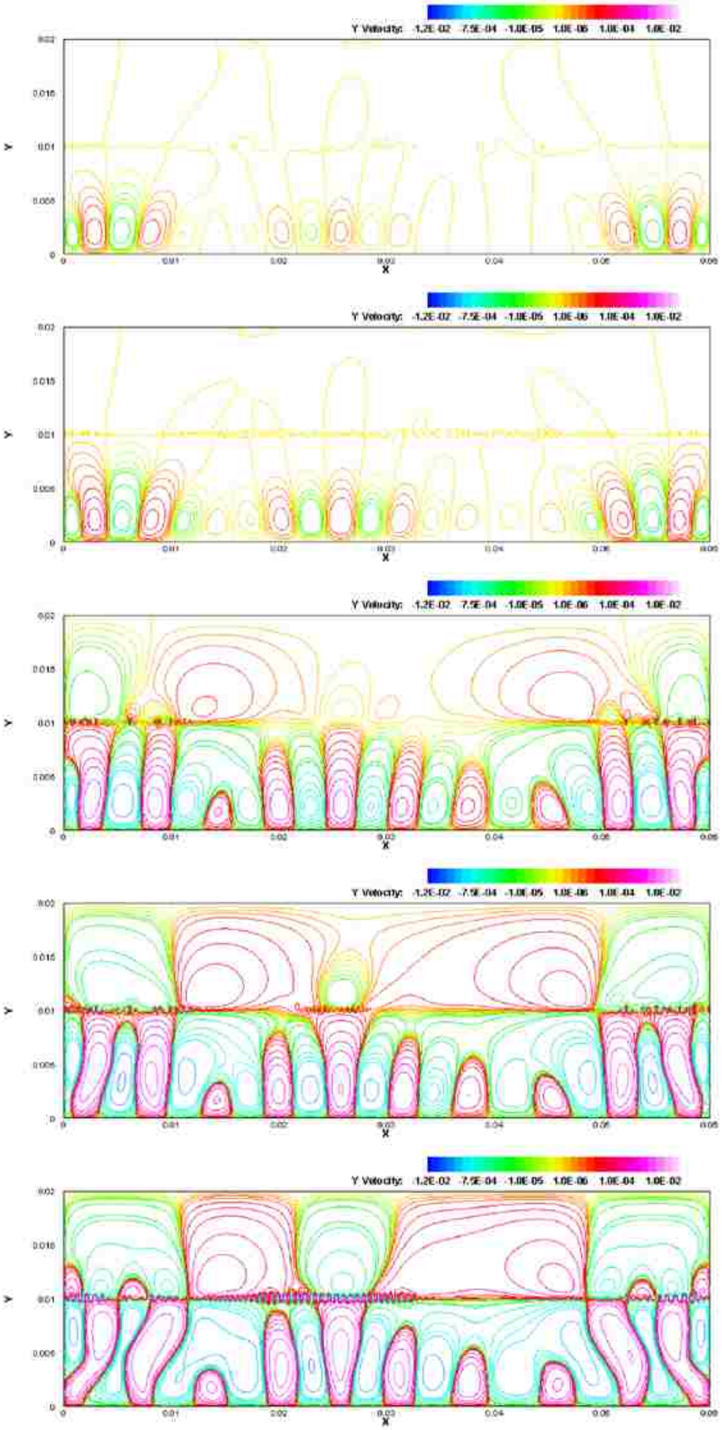
Y Velocity: -1.2E-02 -7.5E-04 -1.0E-05 1.0E-06 1.0E-04 1.0E-02
Y
0.02
0.015
0.01
0.005
0
X
0
0.01
0.02
0.03
0.04
0.05
0.06

(a)

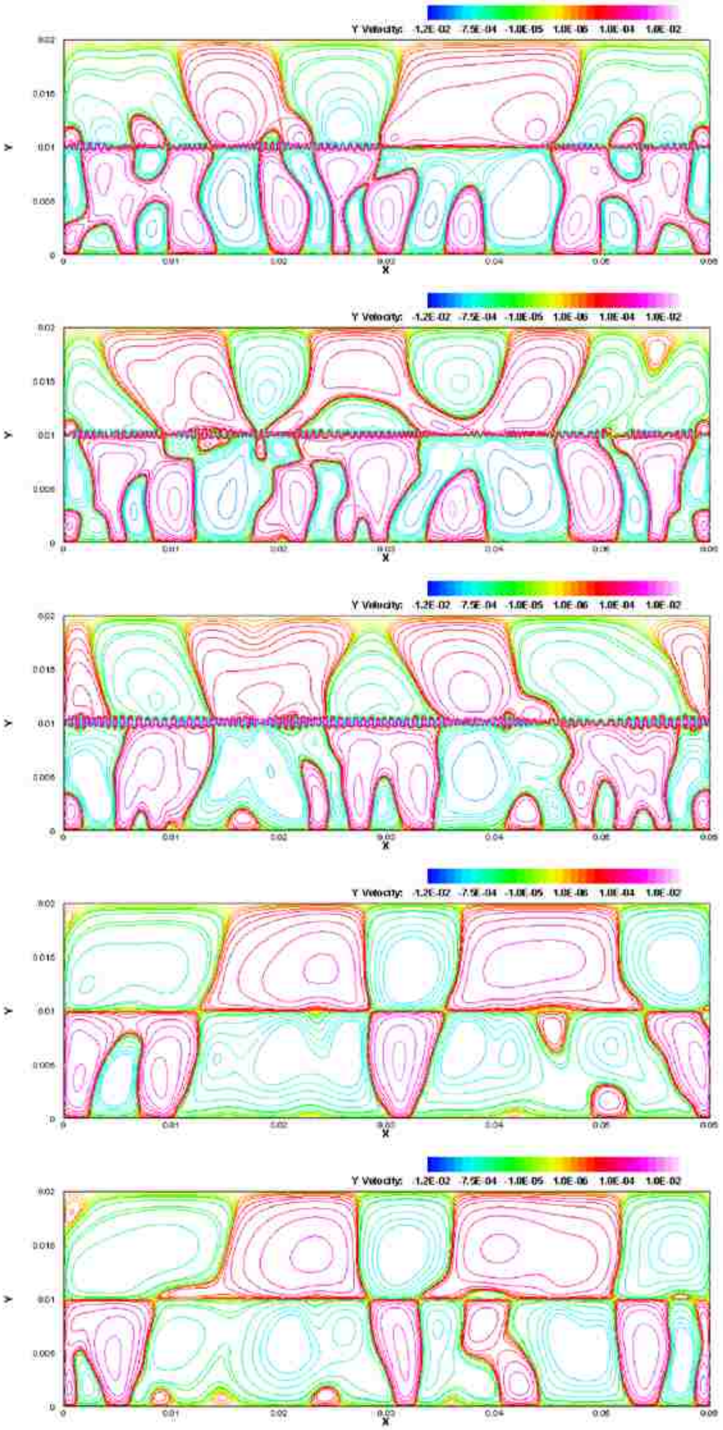
Y Velocity: -1.2E-02 -7.5E-04 -1.0E-05 1.0E-06 1.0E-04 1.0E-02
Y
0
0.005
0.01
0.015
0.02
X
0
0.01
0.02
0.03
0.04
0.05
0.06

(b)

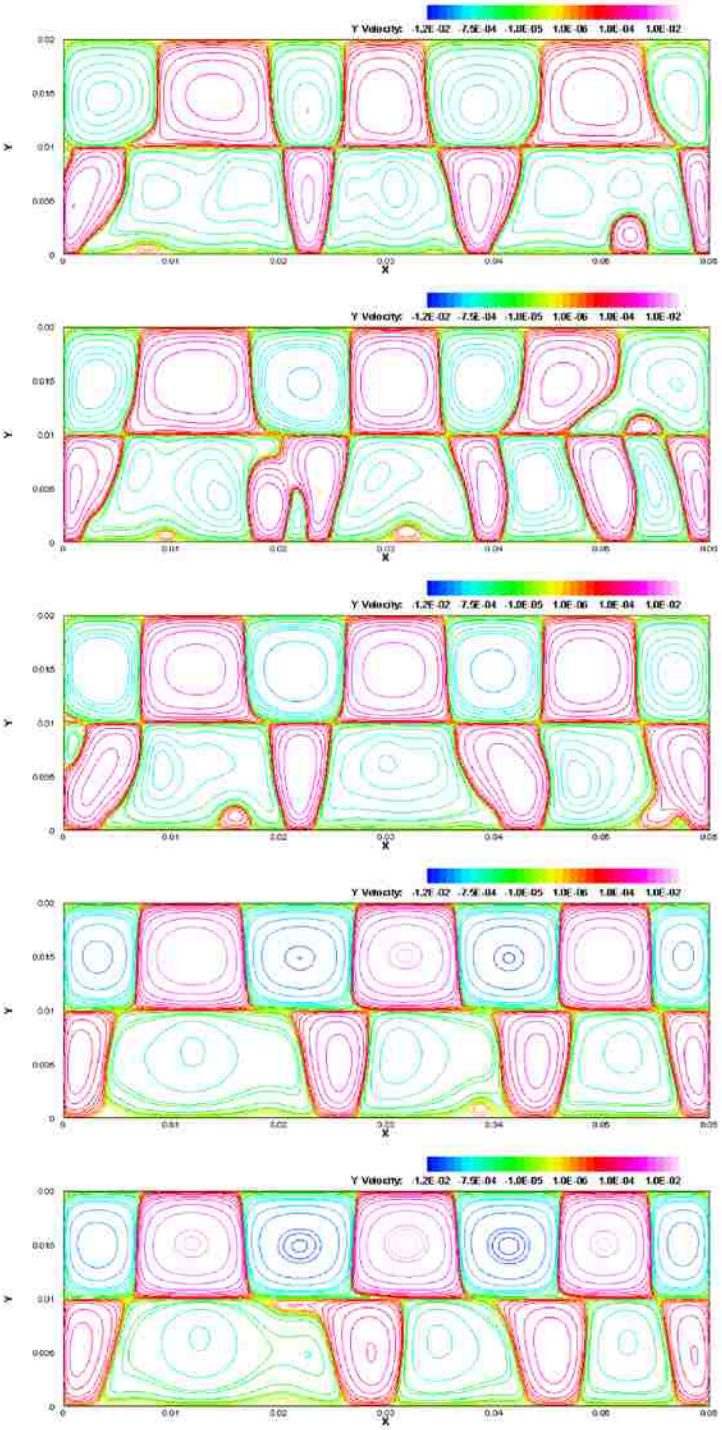

(c)

Figure 35 y-component of velocity contour for air-water system at various time. (a) t = 12, 13, 16, 17, 18 second; (b) t = 19, 20, 22, 45, 50 second; t = 75, 110, 130, 220, 300 second.

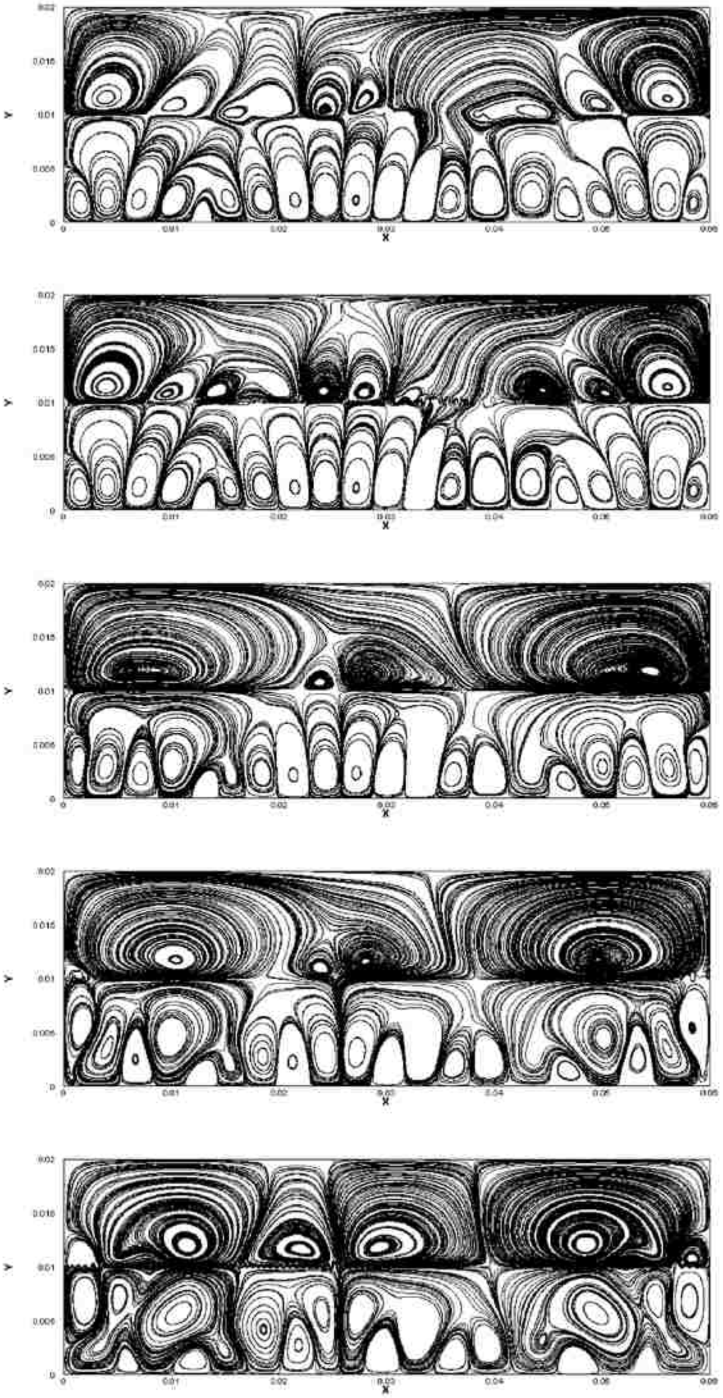

(a)

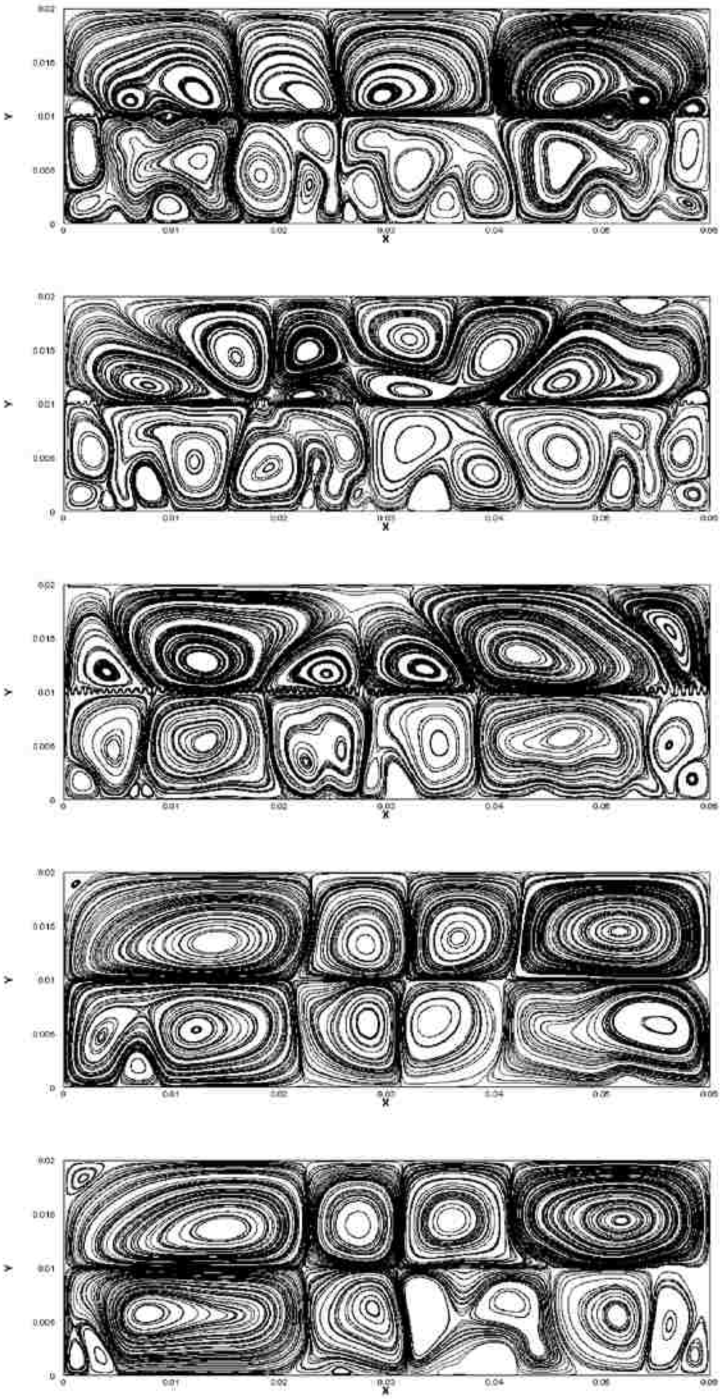

(b)

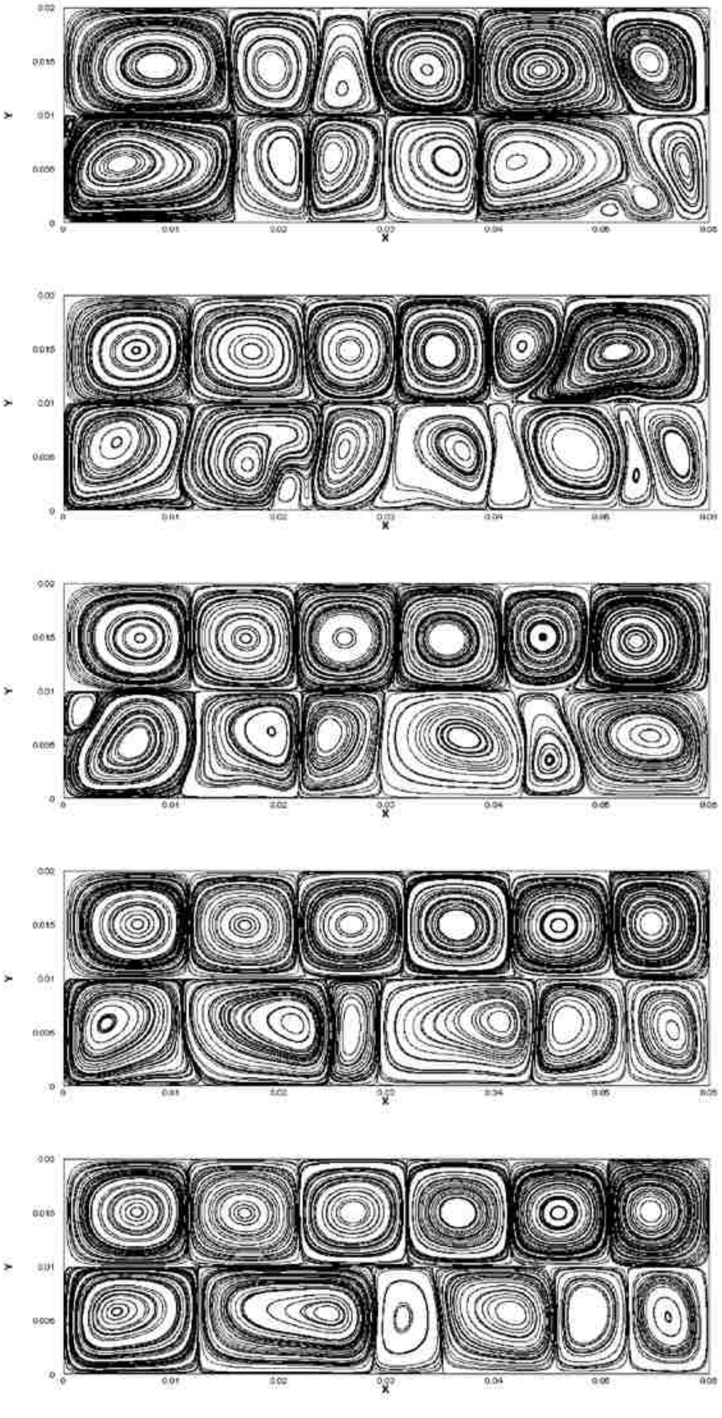

(c)

Figure 36 Streamlines for air-water system at various time. (a) t = 12, 13, 16, 17, 18 second; (b) t = 19, 20, 22, 45, 50 second; t = 75, 110, 130, 220, 300 second.

4.4.3 Oil-Water system

When air is replaced by a much denser fluid, like oil, the density ratio is significantly reduced. The potential for the numerical instability is alleviated. The flow dynamics are predicted by the numerical simulation with the parameters listed in Table 7.

Table 7 Material properties fro oil-water system.

Fluid	$\rho(kg/m^3)$	μ	g	$d(m)$	Ra	$L(m)$
1	800	0.2	9.8	0.01	4190	0.06
2	998.2	1.002e-3		0.01	290877	

The fluid domain is configured the same as the air-water system with the same dimensions, and the same boundary conditions are imposed. Compared to the light air layer, the denser oil layer applies larger level of hydrostatic pressure onto the water layer. Again, we start our evaluations about this numerical experiment from the bottom part, the water layer. The isotherm contours shown in Figure 37 indicate that the creation of the water plumes is delayed by about 7 seconds. Also, different dynamics of the plume structure are observed. When a plume is formed in the air-water system, it raised quickly up toward the interface and mixes with plumes arrived earlier. However, each single plume structure predicted in the oil-water system is much larger and wider. With the Boussinesq approximation, the density within the boundary of the plume is smaller than the surrounding fluids, due to its higher temperature. The motion of the plume can be treated as a gas bubble rising a heavy fluid. The larger the plume structure, the larger the curvature will be. With a larger curvature, the structure is more easily to be bent and flatten by the diffusion term. As observed in the isotherms, the plumes merge quickly and form new structures spreading and as a result the surrounding fluid is heated more efficiently. From the view of the molecular dynamics, with the presence of an external pressure on the fluids, the molecules are bonded more closely, and the path for energy exchange is shortened.

The oil layer in this setup has a much higher thermal conductivity than the air used in the previous study. When the interface gets heated, the thermal energy is transferred across the interface more efficiently. With the increased interface temperature, the Rayleigh number for the oil increases and its competition against the thermal diffusion effect is gradually reflected by the perturbed temperature distribution in this layer. Although the calculated Rayleigh number for the oil layer almost doubles the value in the air layer, the thermal conductivity for oil is 5 times higher than air. By comparing the isotherms between *Figure 33* and Figure 37, it is easily seen that the buoyancy effect is struggling to overcome the viscous effects for fluid motion to onset, and thermal diffusion distributes the thermal energy evenly in the oil layer.

By inspecting streamlines shown in Figure 38, the overall dynamics in the Bénard cells for the oil-water system do not differ too much from the air-water system. Initially smaller cells are formed in the water layer and being pushed back and forth in the horizontal direction. Later, the cells group into a larger regular ones as the Rayleigh number gradually decreases. On the contrary, the larger cells in the oil layer indicate the redistribution of the flow by the thermal diffusion effect. However, with the increase of temperature at the interface, the larger cells are split into smaller ones, due to the increase influence of buoyancy effect. The wave number for each layer is calculated, 2.62 for the oil layer and 3.14 for the water layer.

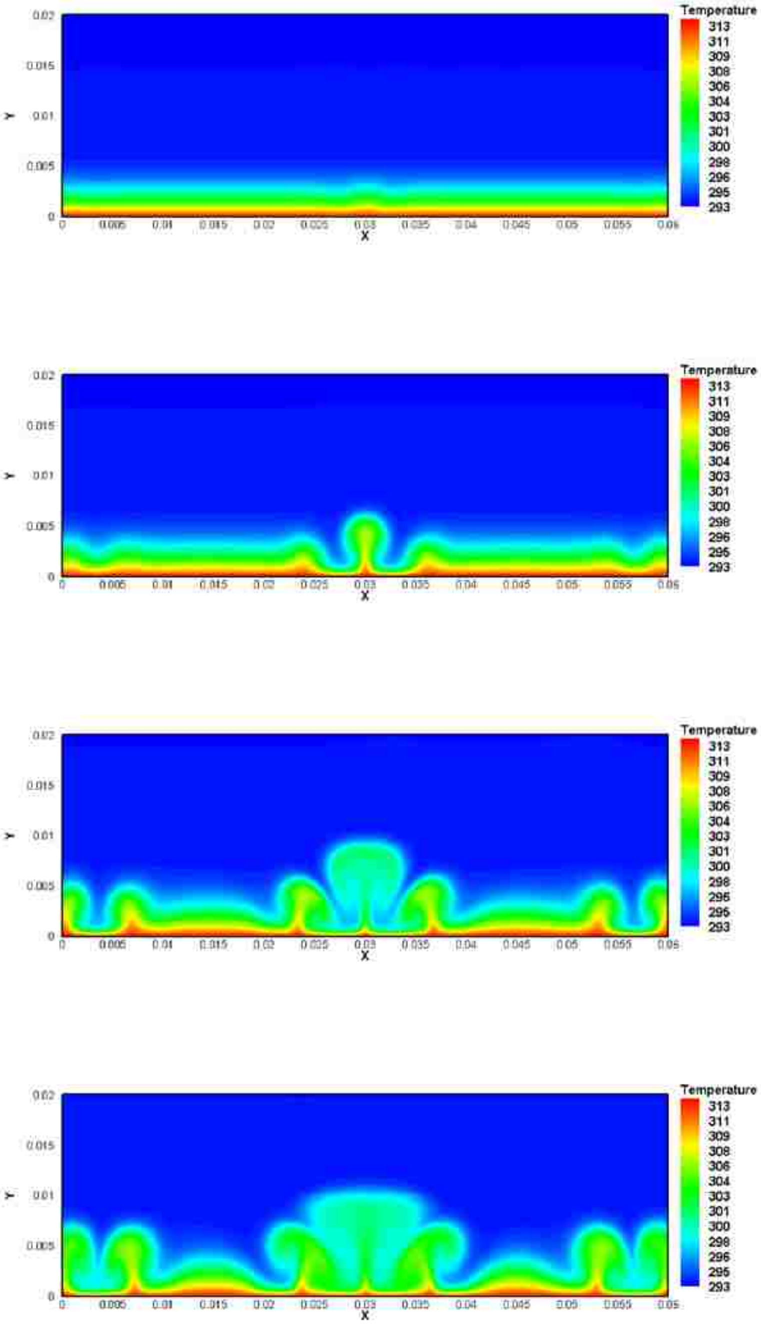
Temperature
313
311
309
308
306
304
303
301
300
298
296
295
293
Y
0
0.005
0.01
0.015
0.02
X
0
0.005
0.01
0.015
0.02
0.025
0.03
0.035
0.04
0.045
0.05
0.055
0.06

(a)

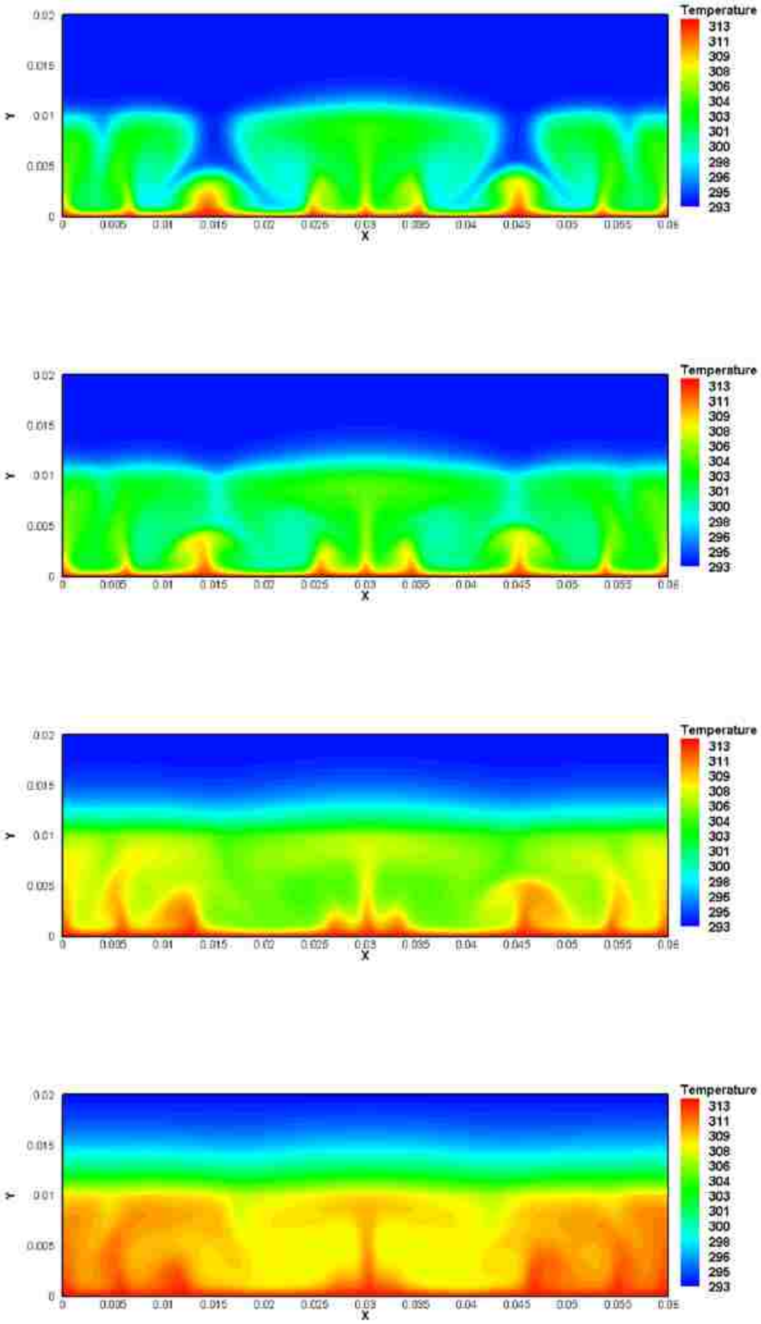
Temperature
313
311
309
308
306
304
303
301
300
298
296
295
293
Y
0
0.005
0.01
0.015
0.02
X
0
0.005
0.01
0.015
0.02
0.025
0.03
0.035
0.04
0.045
0.05
0.055
0.06

(b)

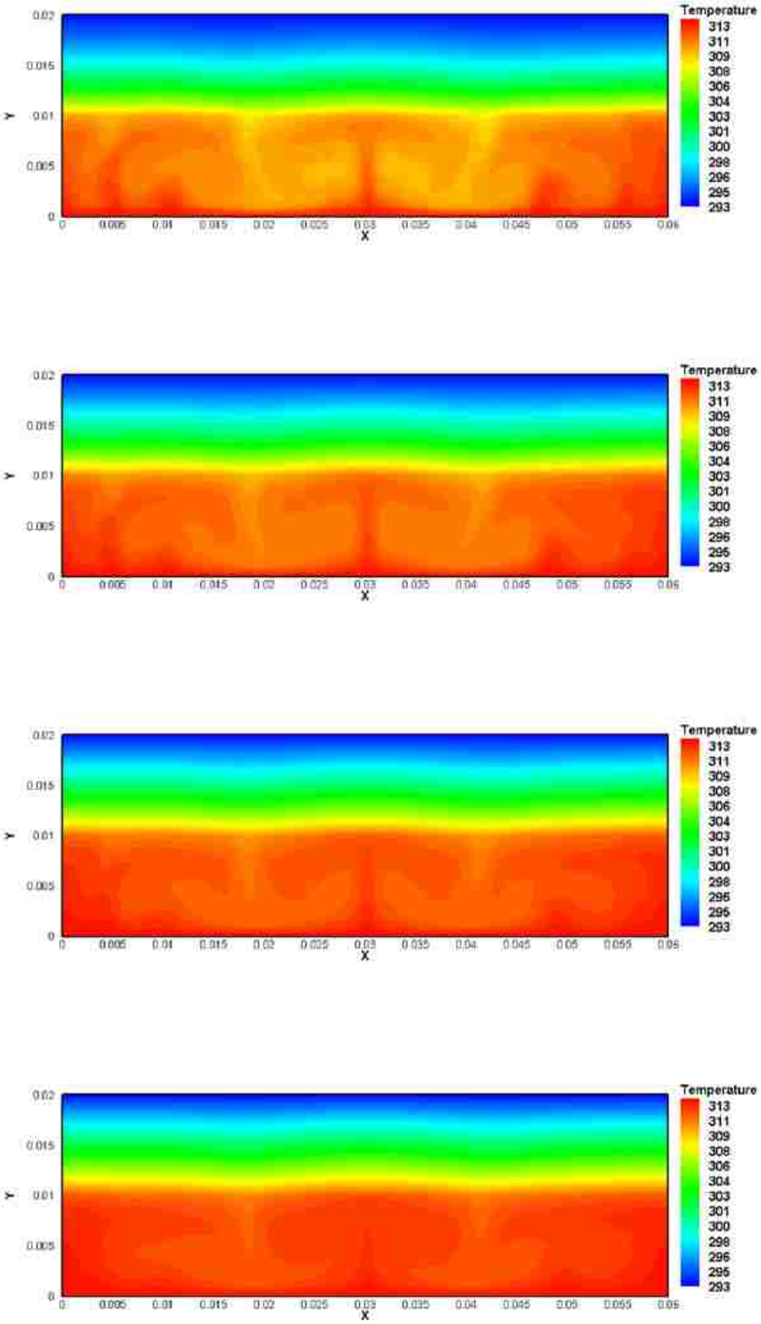

(c)

Figure 37 Isotherms for oil-water system at various time. (a) t = 20, 25, 30, 35 second; (b) t = 50, 60, 100, 150 second; (c) t = 200, 250, 300, 380 second.

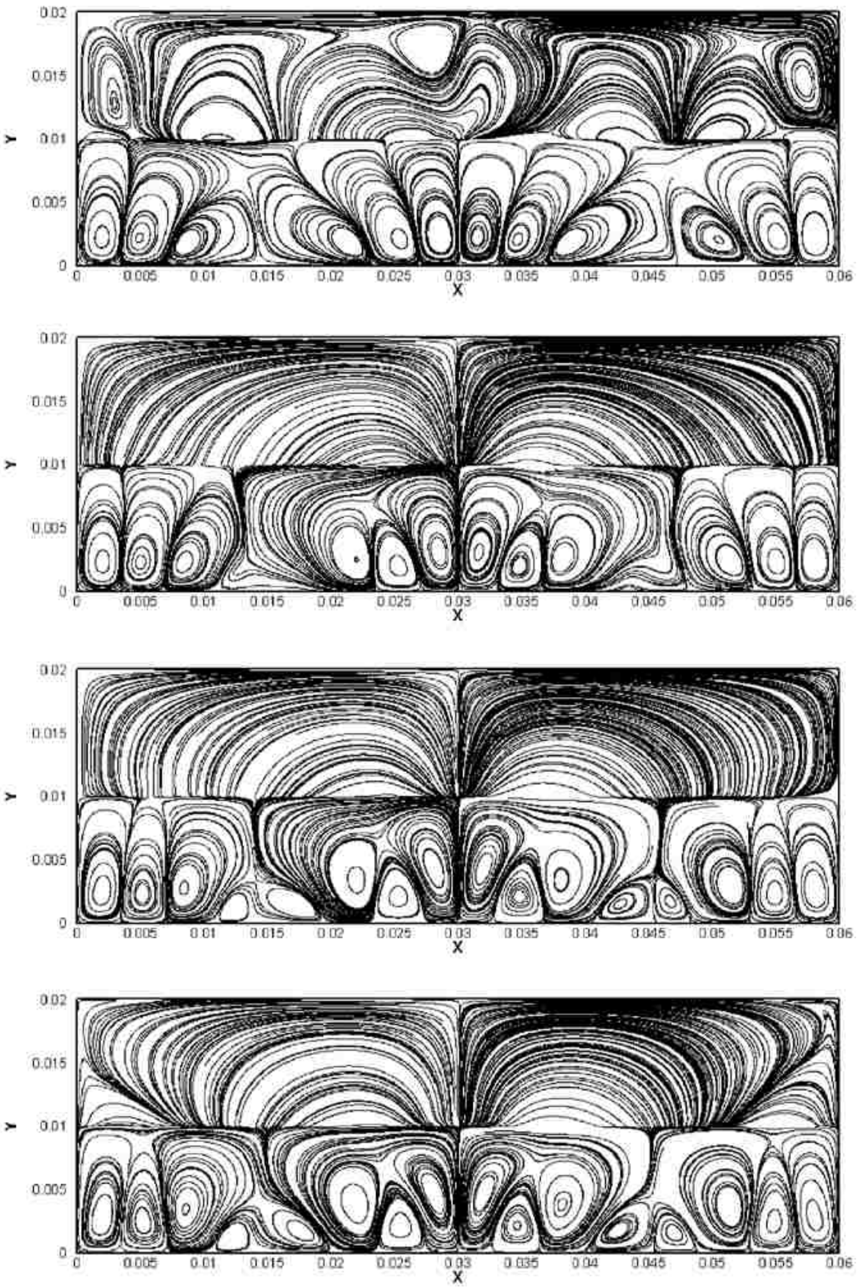

0.02
0.015
Y
0.01
0.005
0
0
0.005
0.01
0.015
0.02
0.025
0.03
0.035
0.04
0.045
0.05
0.055
0.06
X

(a)

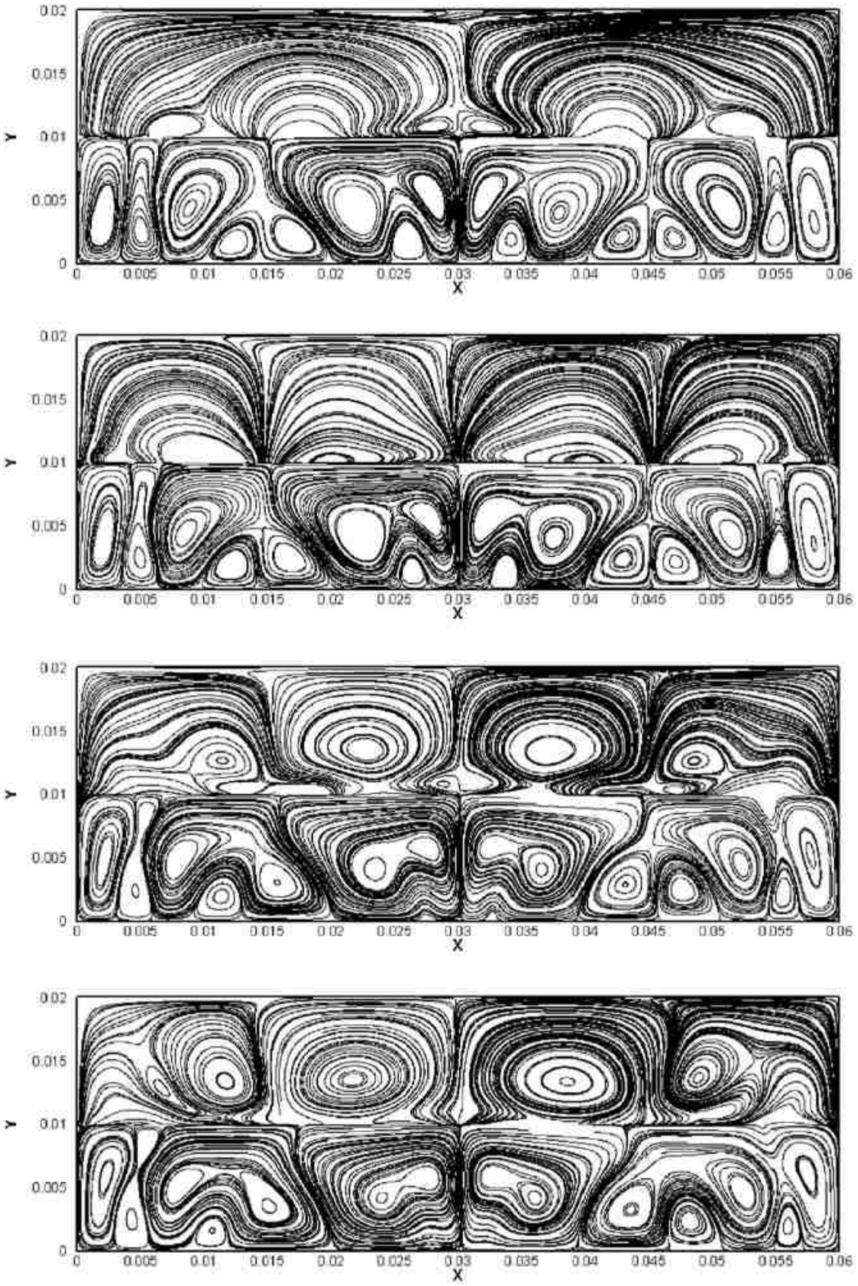
0.02
0.015
Y
0.01
0.005
0
0
0.005
0.01
0.015
0.02
0.025
0.03
0.035
0.04
0.045
0.05
0.055
0.06
X

(b)

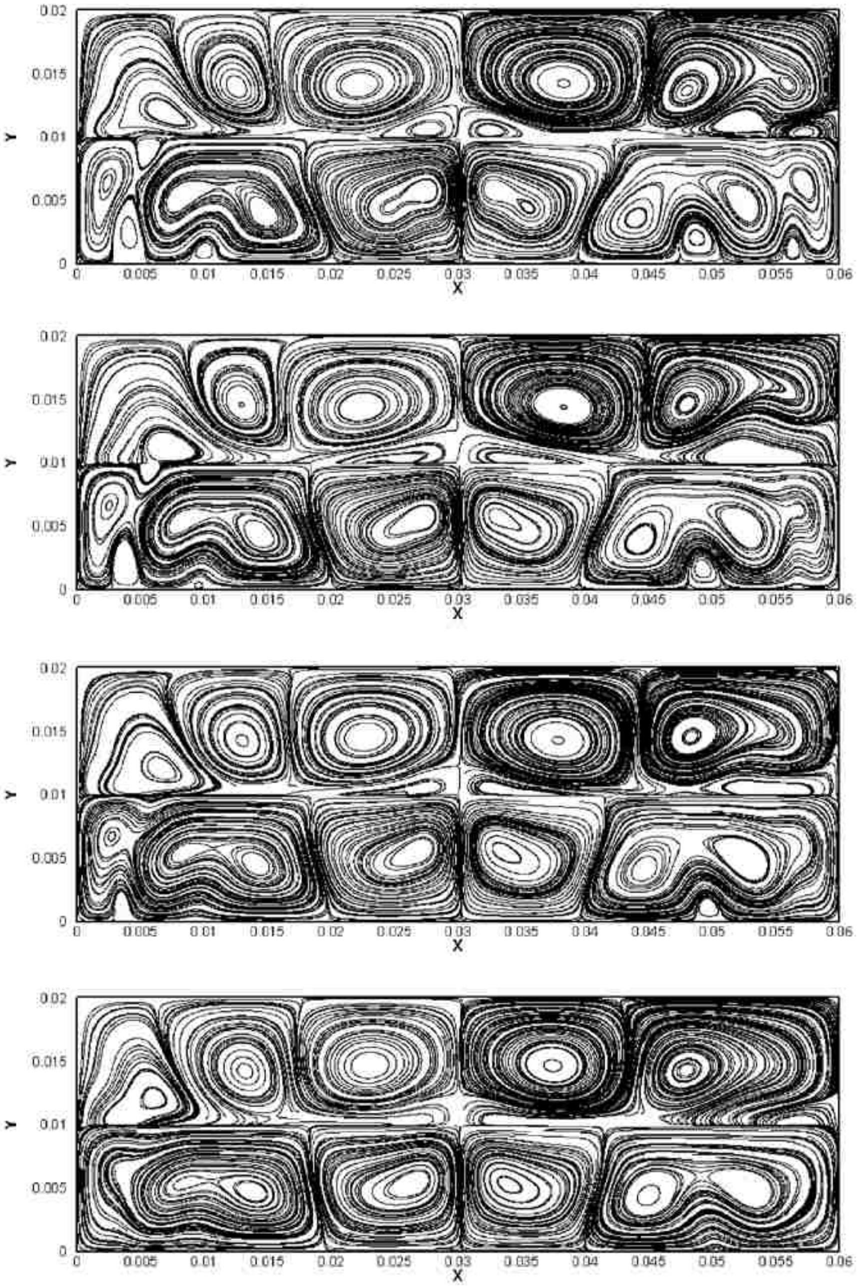

(c)

Figure 38 Streamlines for oil-water system at various time. (a) t = 20, 25, 30, 35 second; (b) t = 50, 60, 100, 150 second; (c) t = 200, 250, 300, 380 second.

4.4.4 Liquid metal (Gallium) and air

The advancement in manufacturing precision allows more transistors to be put into the chips. However, with dramatically increased energy density in the small packages the removal of dissipated heat becomes a challenge. The heat transfer problems in electronic devices are becoming so severe that they may slow, or even limit, the development of the entire chip and system design. Several investigators have developed methods to reduce heat generation in the dies. One of the approach is to quickly dissipate the heat and bring the package to a low temperature while it is in operation. Various high performance thermal compounds have been developed to transfer the dissipated heat from CPU/GPU to the heat sink. Among the choices, liquid metals, like Gallium, received tremendous interests in recent years. Figure 39 shows the solid gallium and the crystallization of gallium from melt. Thin layer of solid Gallium is applied onto the top of the component. Above 303 K, Gallium is melted and a gap is left between the liquid metal and heatsink. A double layer Rayleigh-Bénard convection system is formed when the gap is filled by air. Here we study a 2D system with slightly larger dimensions and the parameters used for the 2D two phase liquid metal-air Rayleigh-Bénard system are listed in

Table 8. The density, thermal conductivity and viscosity data for Gallium at liquid state is given in Refs [41–43].

Table 8 Material properties fro air-gallium system.

Fluid	$\rho(kg/m^3)$	μ	g	$d(m)$	Ra	$L(m)$
1	1.225	1.789e-5	9.8	0.01	2205	0.06
2	6095	1.369e-3		0.01	8165	

Figure 39 Metal Gallium. (a) Brittle solid gallium; (b) Crystallization of gallium from melt.

The whole domain is initialized with constant temperature at 313 K, above the melting point of Gallium. The bottom plate is kept at 333 K and the top plate is at 313K. Figure 40 shows contours of temperature, x-component of the velocity, and y-component of the velocity at t = 4, 5, 8, 12, 15, 18 seconds. For the bottom layer, fluid temperature rises evenly in the lateral direction. Initially, the Rayleigh number is 8165 for the liquid gallium. The heat is transferred at a higher rate in the gallium transfers large brings up the interface temperature within a short period of time. Rapid increase of interface temperature quickly reduces the Rayleigh number below the critical value for the bottom layer. Hence, only conduction is observed in this layer. The x- and y-component of the velocity illustrate that the flow structure in the Benard cells is smeared out by the thermal diffusion effects. Contrary to what is found in the bottom layer, at t = 5, the Rayleigh number increases to 1654 for the air layer. Clear ascending and descending flows are found from contours of y-component of the velocity, which is generated by the Boussinesq term. And the x-component of the velocity exemplifies the effect of the thermal diffusion. With the decomposed velocity, the driven mechanism of this flow pattern and the competition between the thermal diffusion and buoyancy induced convection are well explained. With the simulation going forward, for the air layer, the Rayleigh number continues to increase and the system starts to get disturbed by large bulk of fluids with higher temperature. The streamline plot in Figure 41 shows the evolution the convection cells. Large cells are formed at earlier time step and break into smaller ones with the increase of Rayleigh number. Away from the lateral walls, the cells are more orthogonal and wall effect is depicted by the compressed cells besides the walls.

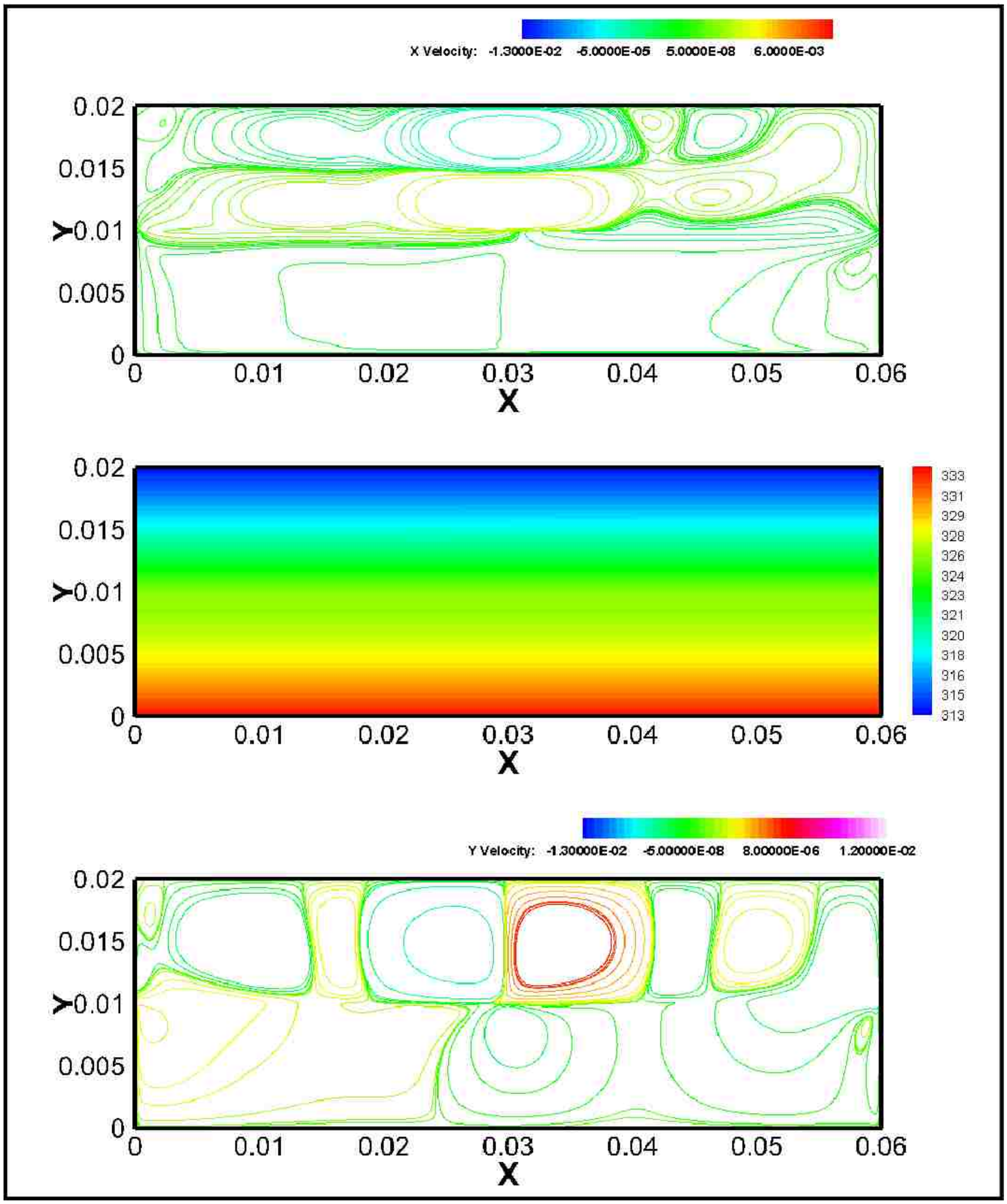
X Velocity: -1.3000E-02 -5.0000E-05 5.0000E-08 6.0000E-03
0.02
0.015
Y 0.01
0.005
0
0 0.01 0.02 0.03 0.04 0.05 0.06
X
333
331
329
328
326
324
323
321
320
318
316
315
313
Y Velocity: -1.30000E-02 -5.00000E-08 8.00000E-06 1.20000E-02

(a)

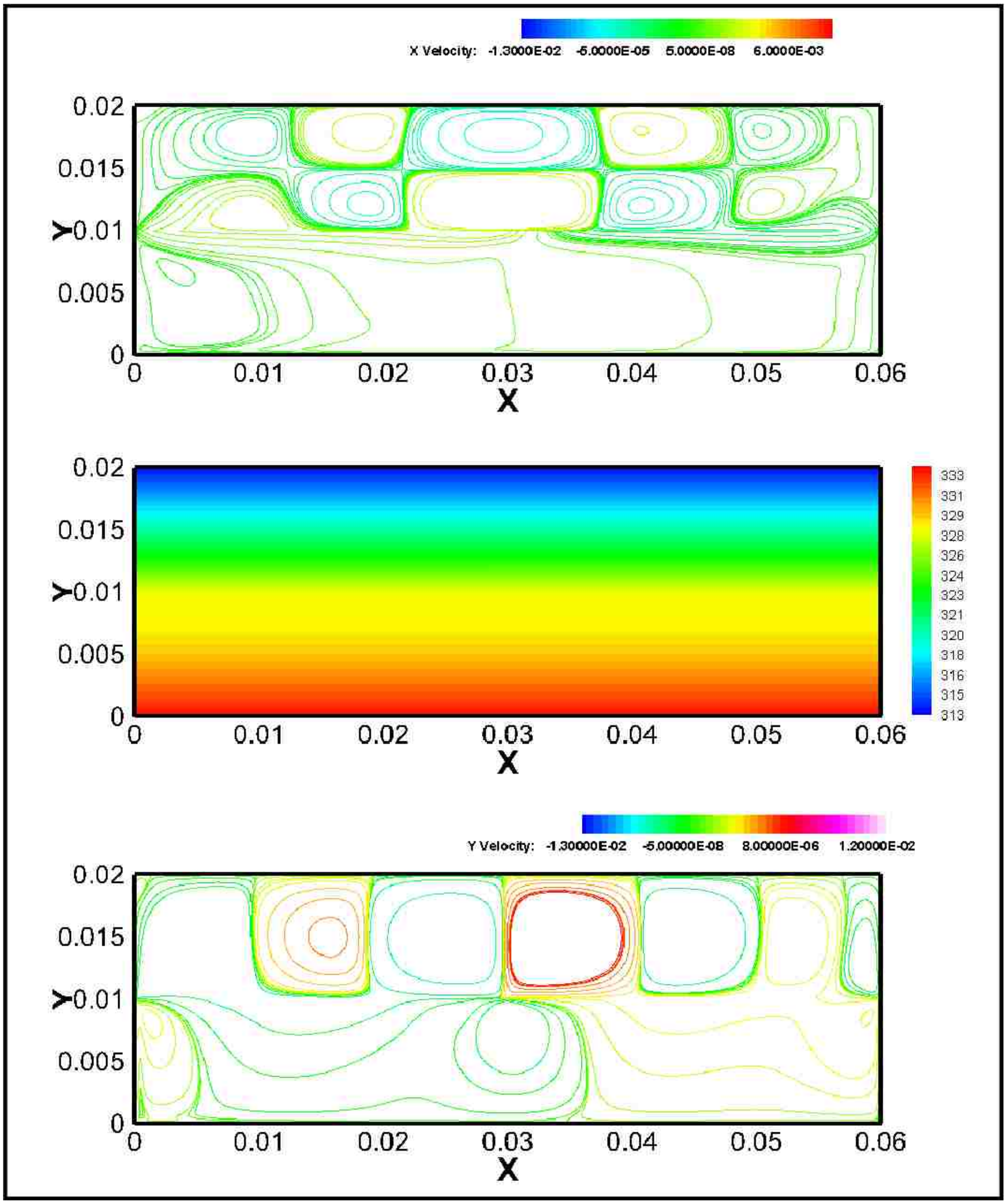
X Velocity: -1.3000E-02 -5.0000E-05 5.0000E-08 6.0000E-03
Y
X
0.02
0.015
0.01
0.005
0
0.01
0.02
0.03
0.04
0.05
0.06
333
331
329
328
326
324
323
321
320
318
316
315
313
Y Velocity: -1.30000E-02 -5.00000E-08 8.00000E-06 1.20000E-02

(b)

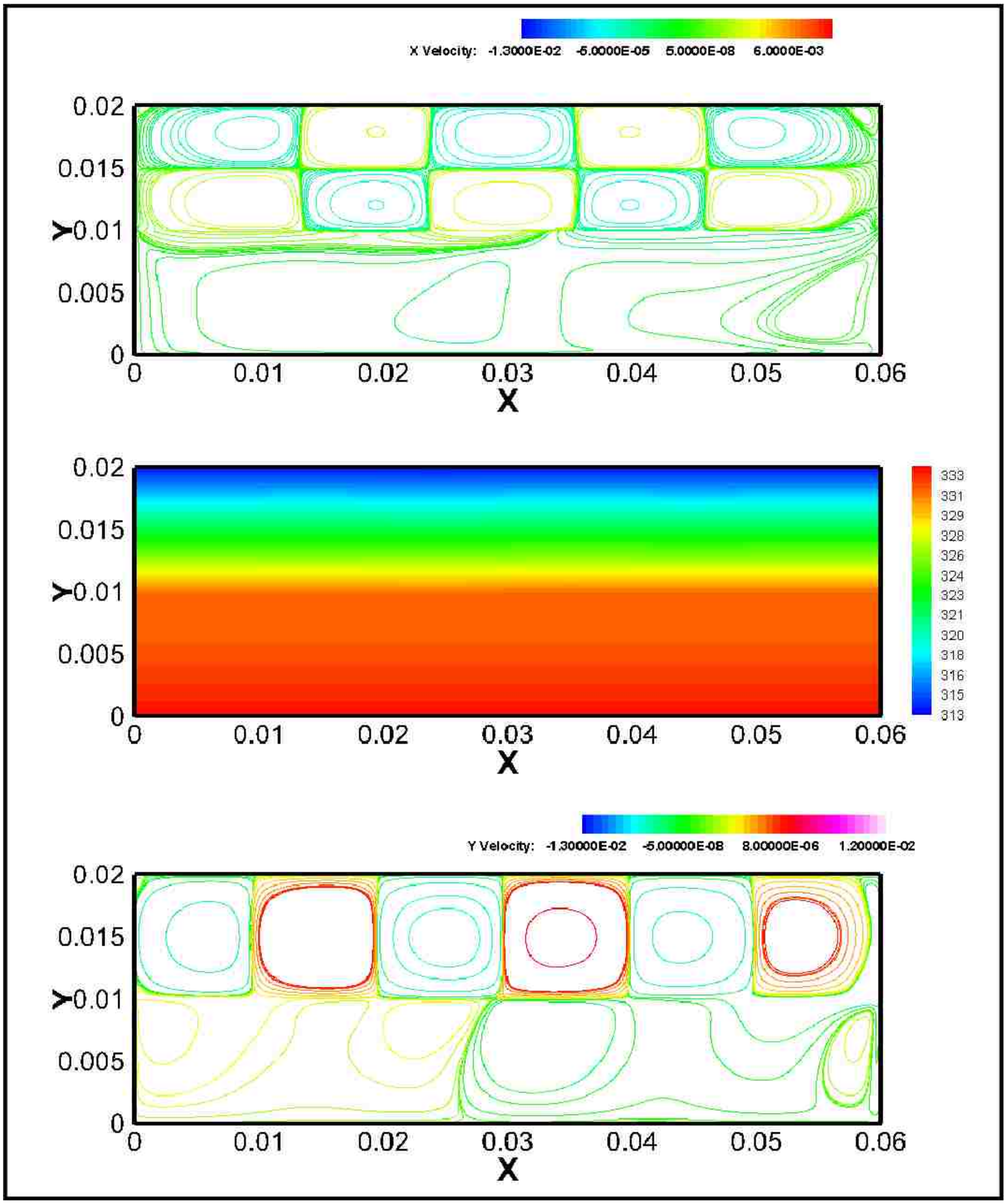

X Velocity: -1.3000E-02 -5.0000E-05 5.0000E-08 6.0000E-03
0.02
0.015
Y 0.01
0.005
0
0 0.01 0.02 0.03 0.04 0.05 0.06
X
333
331
329
328
326
324
323
321
320
318
316
315
313
Y Velocity: -1.30000E-02 -5.00000E-08 8.00000E-06 1.20000E-02

(c)

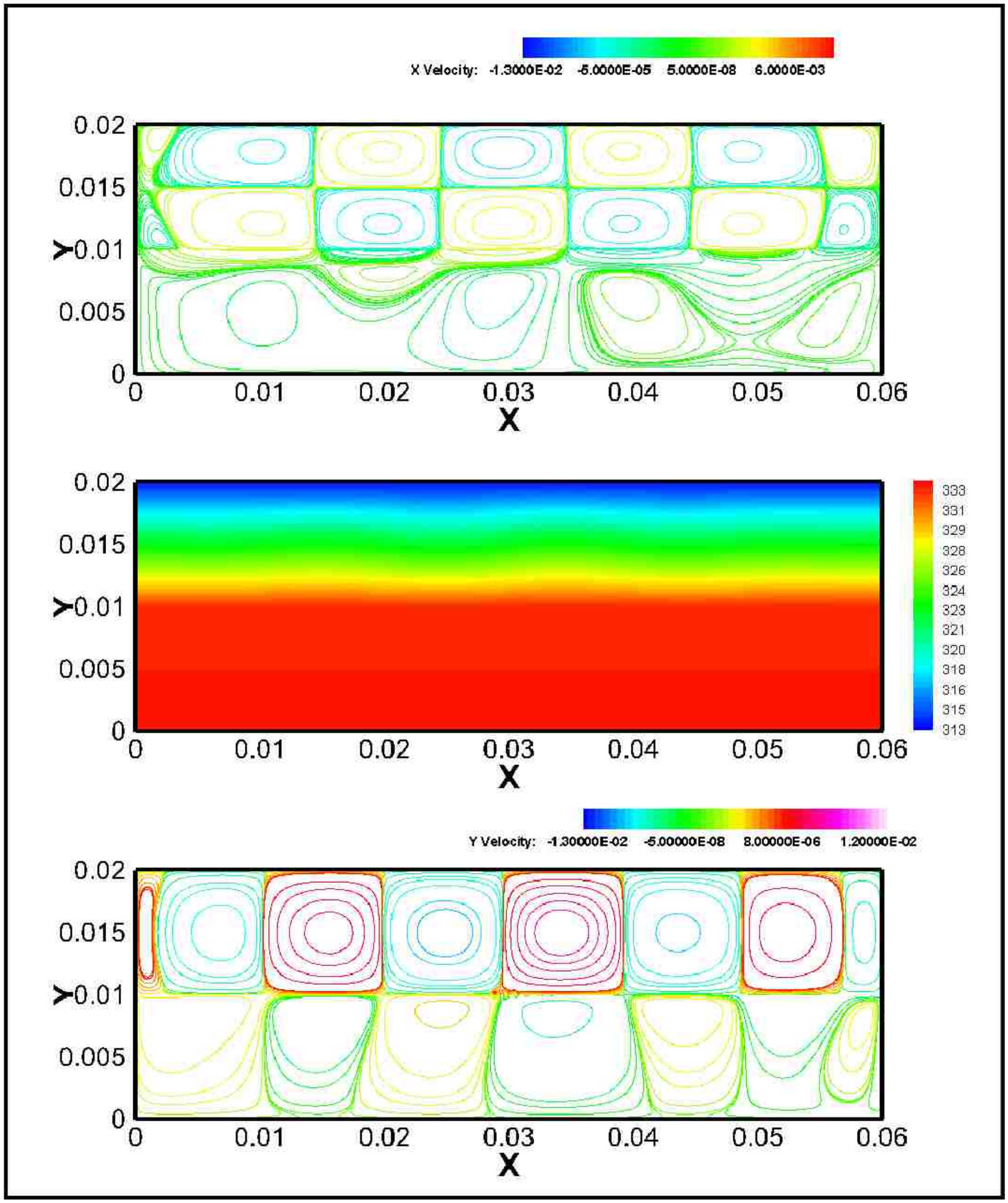
X Velocity: -1.3000E-02 -5.0000E-05 5.0000E-08 6.0000E-03
0.02
0.015
Y
0.01
0.005
0
0
0.01
0.02
0.03
0.04
0.05
0.06
X
333
331
329
328
326
324
323
321
320
318
316
315
313
Y Velocity: -1.30000E-02 -5.00000E-08 8.00000E-06 1.20000E-02

(d)

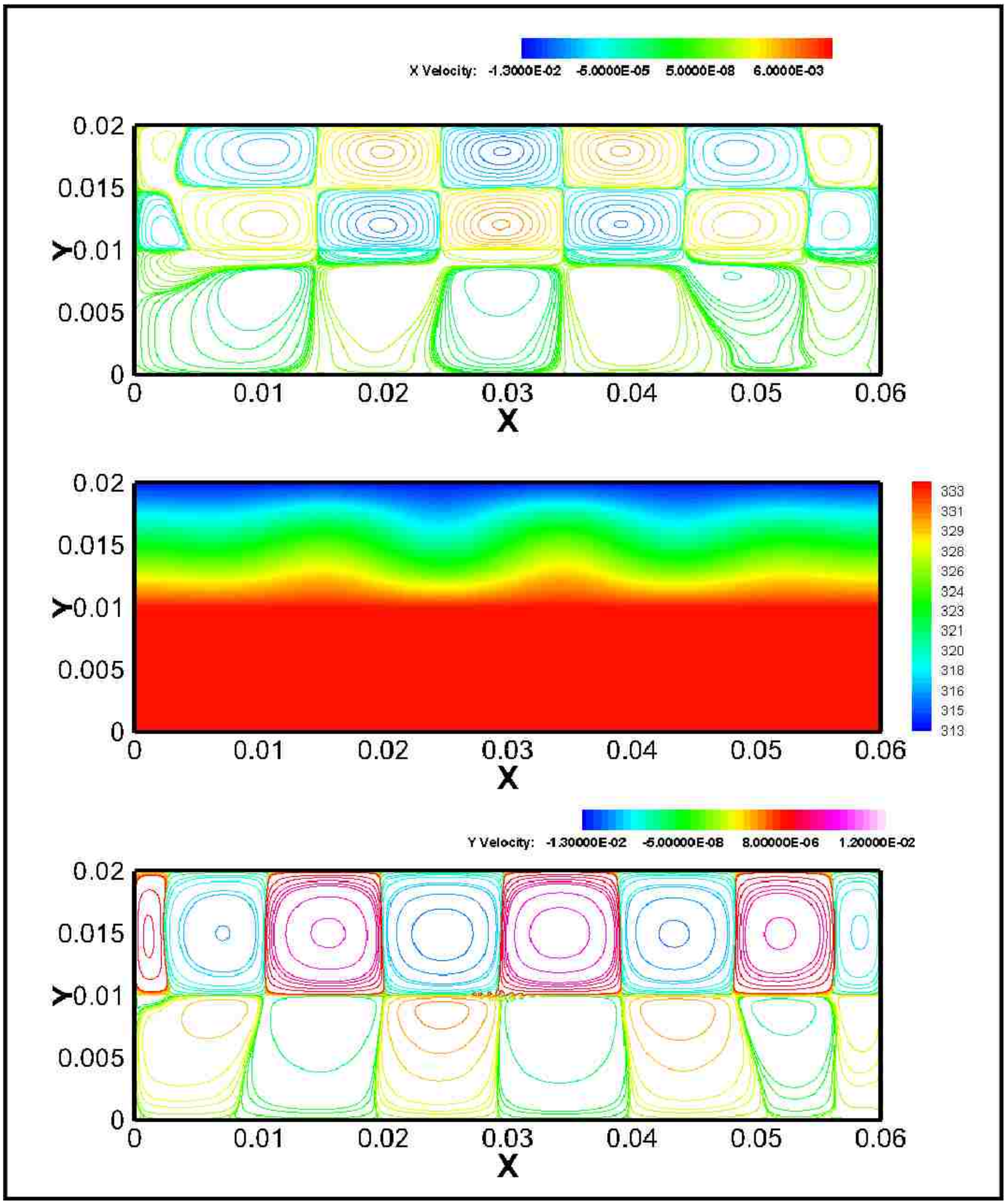
X Velocity: -1.3000E-02 -5.0000E-05 5.0000E-08 6.0000E-03
0.02
0.015
Y 0.01
0.005
0
0 0.01 0.02 0.03 0.04 0.05 0.06
X
333
331
329
328
326
324
323
321
320
318
316
315
313
Y Velocity: -1.30000E-02 -5.00000E-08 8.00000E-06 1.20000E-02

(e)

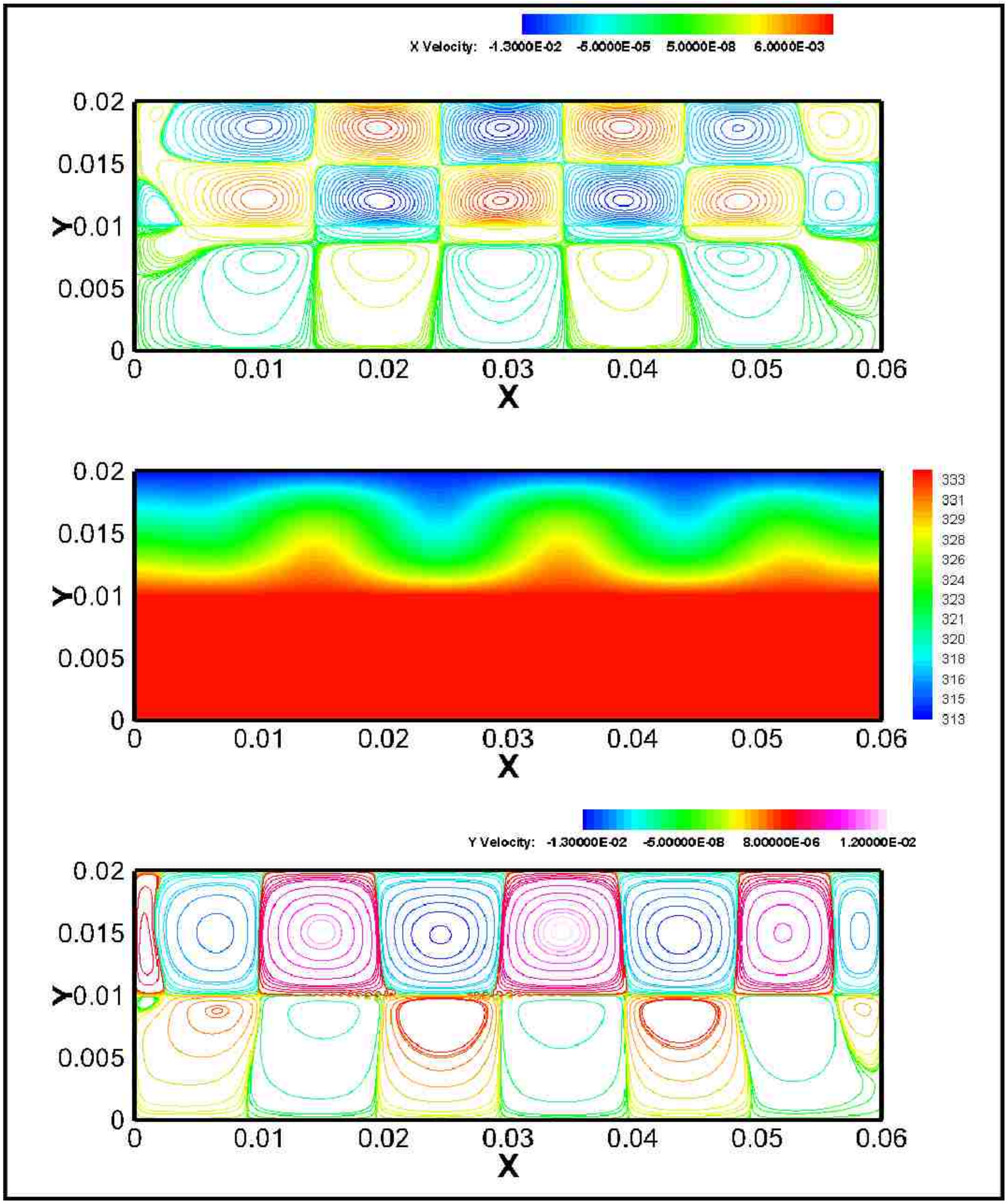

(f)

Figure 40 Contours of Gallium-Air system for u, T and v at various instances. (a) t = 4 s; (b) t = 5 s; (c) t = 8 s; t = 12 s; t = 15 s; t = 18 s.

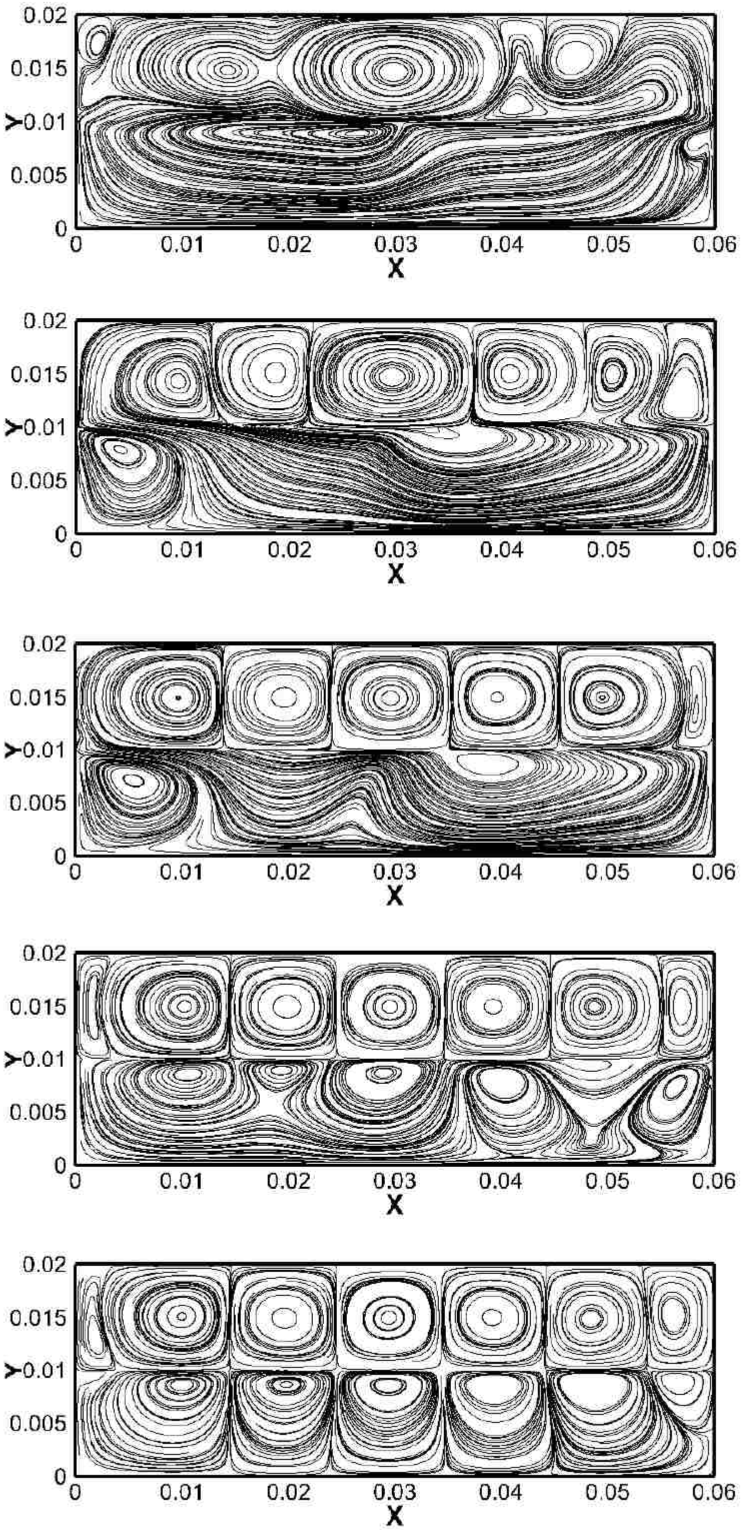

Figure 41 Streamlines of Gallium-Air system at various instances. (a) t = 4 s; (b) t = 5 s; (c) t = 8 s; t = 12 s; t = 15 s; t = 18 s.

Temperature at the interface increases with time. In the meantime, the Rayleigh number also changes accordingly for each layer of fluids. In the previous discussion, we can treat this binary system as two separate Rayleigh-Bénard convection layer with rigid-free boundary and being stitched by the immiscible interface. The linear stability analysis for the single layer rigid free system indicates that the system will break the equilibrium above the critical value. Here we calculated the Rayleigh number and wave number at various time units for each case and plotted the data on the stability diagram obtained by linear stability analysis for rigid-free boundary condition.

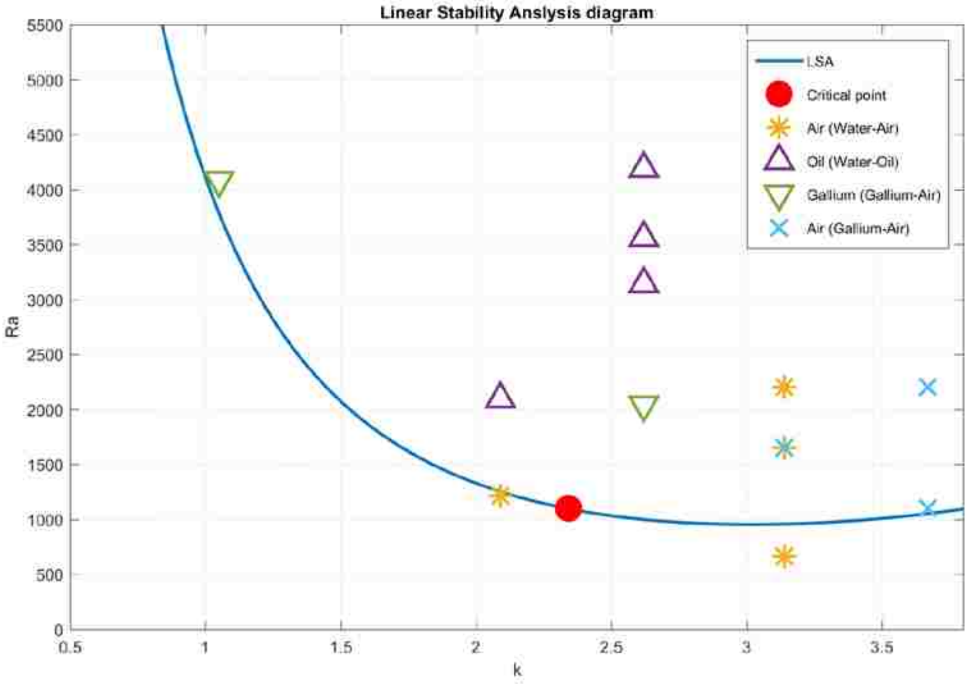

Figure 42 Stability diagram for the rigid-free Rayleigh-Bénard convection.

4.5 Three-dimensional result

Results of two-dimensional simulations presented in the previous section clearly show the capability of our level set method algorithm to characterize flow structures of multiphase fluids. With the results presented and analyses conducted, the mechanism responsible for flow phenomena are well explained. Results presented in the last section for the Rayleigh-Bénard convections illustrate that the presence of lateral walls strongly influence the dynamics in these systems. It will be even more interesting to consider three dimensional domain that has rigid side walls. The wall effects on the Rayleigh-Bénard problem in three-dimensional geometries will be reflected by the changes in flow structures and dynamics. In theory, the extension into a 3^{rd} direction is easy and intuitive. However, the cost on the computational work is expanded exponentially, which directly lengthens the simulations significantly. The 3D schematic of the system is shown in Figure 43.

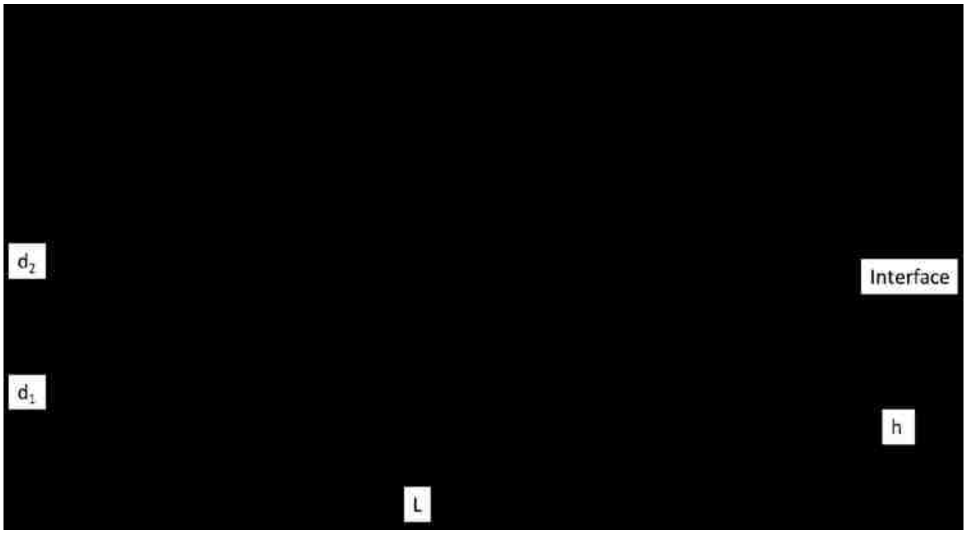

Figure 43 Schematic for two-layer 3D Rayleigh Bénard convection in a three dimensional geometry.

Recall the setups in the 2D air-water system, the prescribed thickness gives the Rayleigh number for the water layer up to 29087, whose magnitude is relatively large compared to the air layer. For the first set of simulations in a three dimensional geometry, the depth of the water layer is set to a value such that the Rayleigh number is 4393 which is comparable with Rayleigh number of the air layer. The parameters used in these simulations are listed in Table 9.

Table 9 Material properties fro 3D air-water system.

Fluid	$\rho(kg/m^3)$	μ	g	$d(m)$	h	$L(m)$	Ra
1	1.225	1.789e-5	9.8	0.01	0.0125	0.06	2205
2	998.2	0.001003		0.0025	0.0125		4393

The 3D domain is initialized with constant temperature 303 K. The top and the bottom boundaries are set to constant temperature, 323 K and 303 K, respectively. Other walls of the domain are insulated. With the extension into the third dimensional space, the characteristics of the flow are no longer planar. Figure 44 and Figure 45 depict the isosurfaces temperature field. The center cross section of XY plane is rendered by the isotherms. Although isotherms illustrate the general trend of the temperature distribution, some 3D plume structures are not projected on the 2D contour. The four temperature isosurfaces, at T = 312 K, 315K, 318K and 321K, represent the formation of the 3D plume structures very well. At t = 11 s, a group of swells are found in the near wall region. The temperature field starts to get perturbed by the buoyancy effect. Away from the wall in x-direction, light ripples also show up on the same isosurface, T = 312 K. As time progresses, these structures continue to expand in every direction. When the rippled surface reach the adiabatic wall in z-direction, it is being flattened. At t = 18 s, non-uniform 3D plume structures are clearly observed. The isotherms at the center cross section can only capture those long-stripped plume structures. If the plume is more circular and resides away from the center plane, it will not be found in the 2D isotherm contour. Different behaviors are shown in the plume development. The long-stripped ones are more self-constrained and grow simultaneously in height, length and width. The scattered circular plumes quickly group and merge together, and they exhibit more irregular structures compared to those of the long-stripped ones. At later instances, it is shown that the newly merged structures align in a skewed direction to the axis (see Figure 45).

The Bénard convection cells also show the non-uniformity of the flow. If the dimension in the z-direction is infinitely long, the streamlines should follow the 2D pattern and superpose layer by layer. For our system, the finite distance between the walls in z-direction severely distorts the streamlines. From Figure 46, the streamlines are tilted following the direction of the skewed plume structures. When approaching to the walls, the streams are rectified and become parallel to the wall. For the air layer, the planar dimensions and Rayleigh number (2205) are the same with the setup in 2D studies. Hence, it is presumably to observe the similar characteristics in the Bénard cells. Figure 46 depicts six rolls of convection cells similar as in the two dimensional Rayleigh Bénard problem of the fluid system. This implies that the side walls would only affect the orientation of the cells for limited wave number. The streamline distribution in the water layer is more chaotic. Twenty four rolls of small Bénard cells are observed at a stable state and the number of rolls in the layers is proportional to the depth ratio of the geometry.

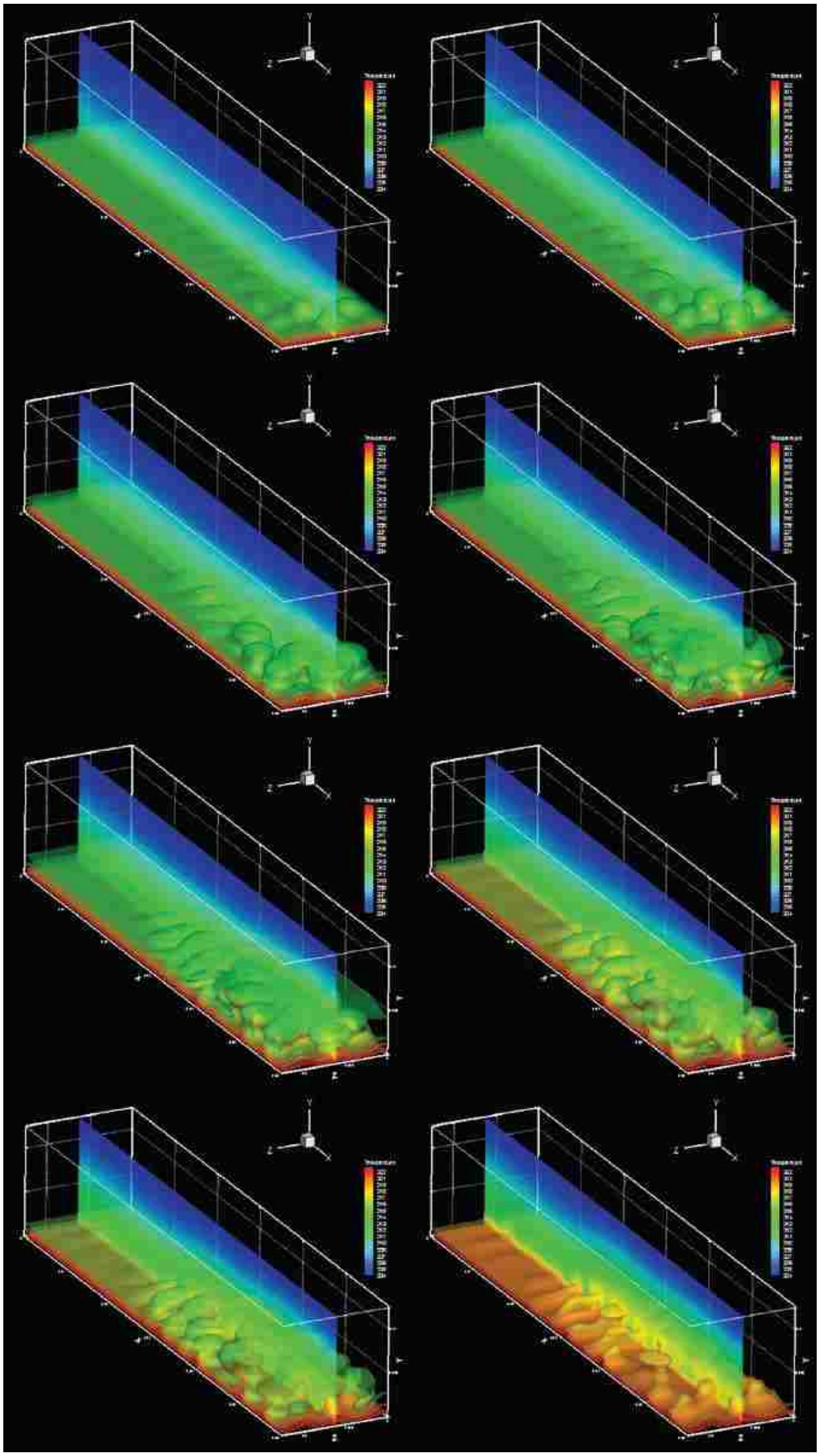

Figure 44 Temperature isosurfaces for 3D air-water system at t = 11, 12, 13, 14, 15, 16, 17, 18 second.

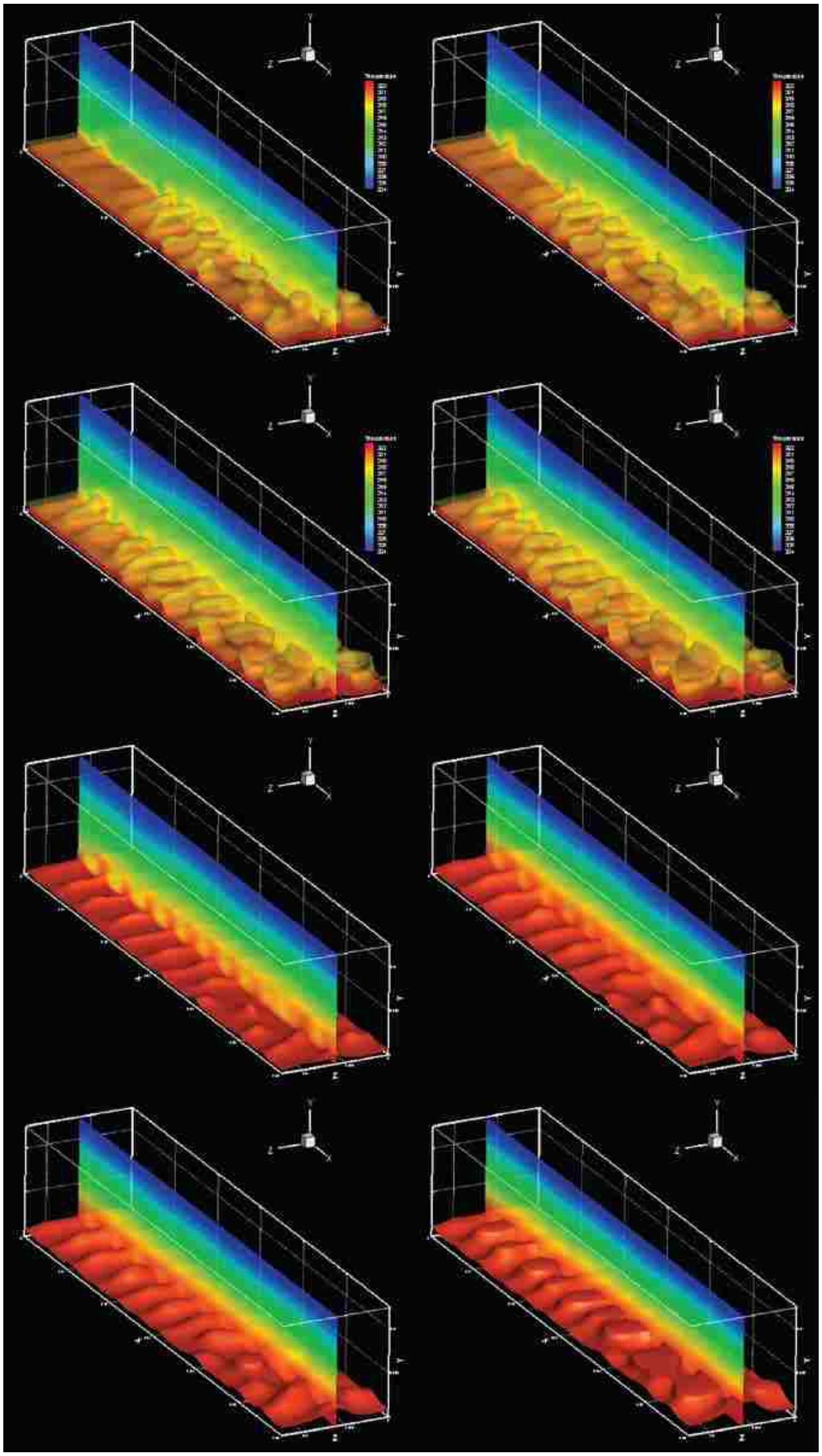

Figure 45 Temperature isosurfaces for 3D air-water system at t =19, 20, 22, 23, 24, 30, 33, 37 second.

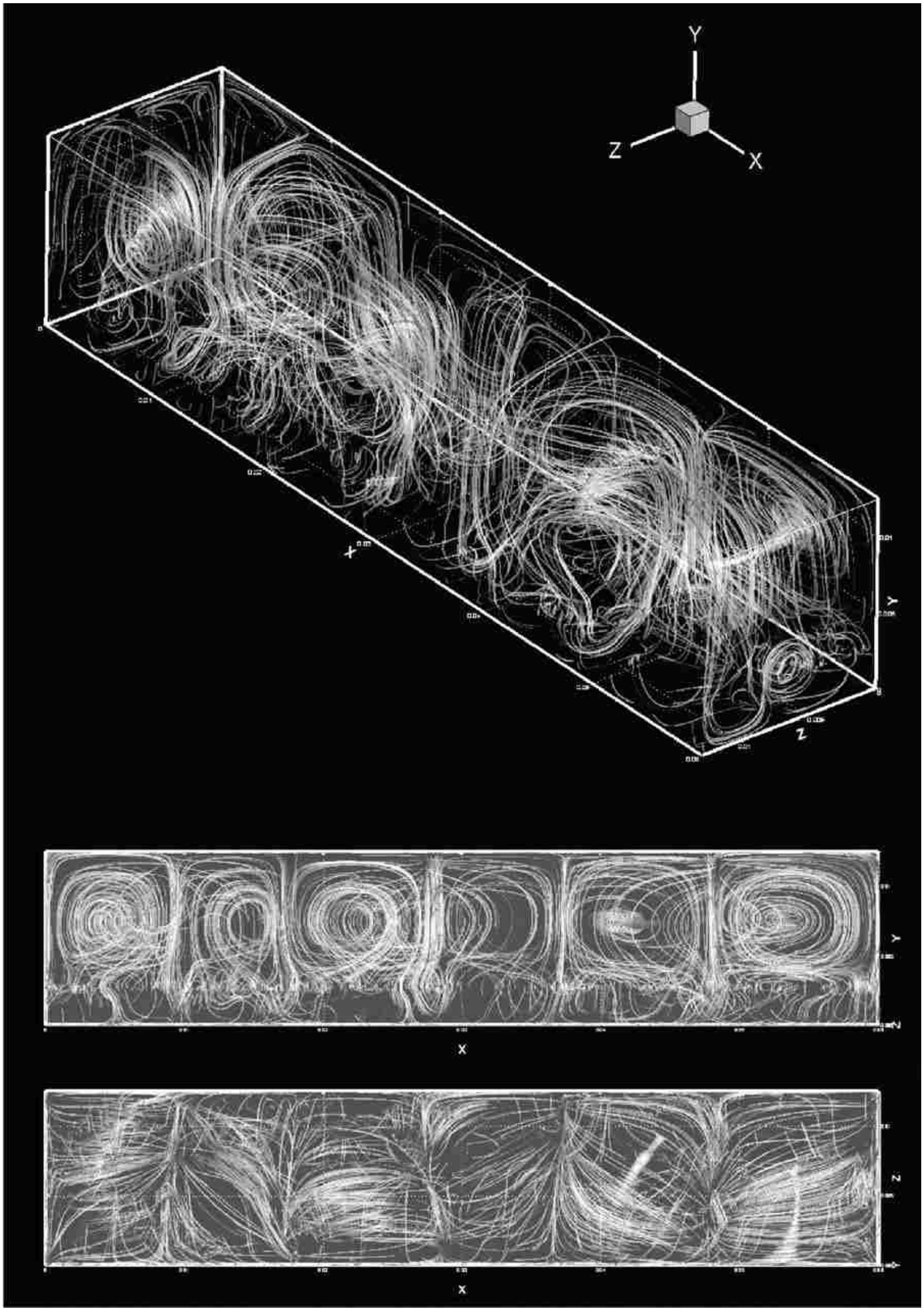

Figure 46 3D streamlines for air-water system at t = 37 second.

Results in a three dimensional geometry illustrates that the narrow wall in the z-direction has strong influence on the convection cells. The streamlines are much tilted and non-uniform plume structures are observed. It is interesting to see the influence from the two sets of lateral walls when they are equally spaced. The physical and geometric parameters for the equally spaced 3D lateral walls are listed in Table 10.

Table 10 Material properties fro air-water system with equal spaced lateral walls

Fluid	$\rho(kg/m^3)$	μ	g	$d(m)$	h	$L(m)$	Ra
1	1.225	1.789e-5	9.8	0.01	0.06	0.06	2205
2	998.2	0.001003		0.01	0.06		290877

The same boundary conditions as in the previous geometry are applied. The isosurfaces shown in Figure 47 exhibits a more uniform formation of the plume structures at early times. As the simulation progresses, small perturbations quickly lead to a non- uniformity in the water layer. The wall effects from the equal spaced lateral boundaries compete to align and guide the flow in its own direction. Here, the wall effects acting on the flow should be equal and we find that the plume structures align in the diagonal direction, as shown in Figure 48. The diagonal alignment of Bénard cells is revealed by instantaneous streamlines depicted in Figure 49. Although the cells are aligned differently, the number of Bénard cells remain the same at the same Rayleigh number. The number of cells was six in each direction within the air-layer.

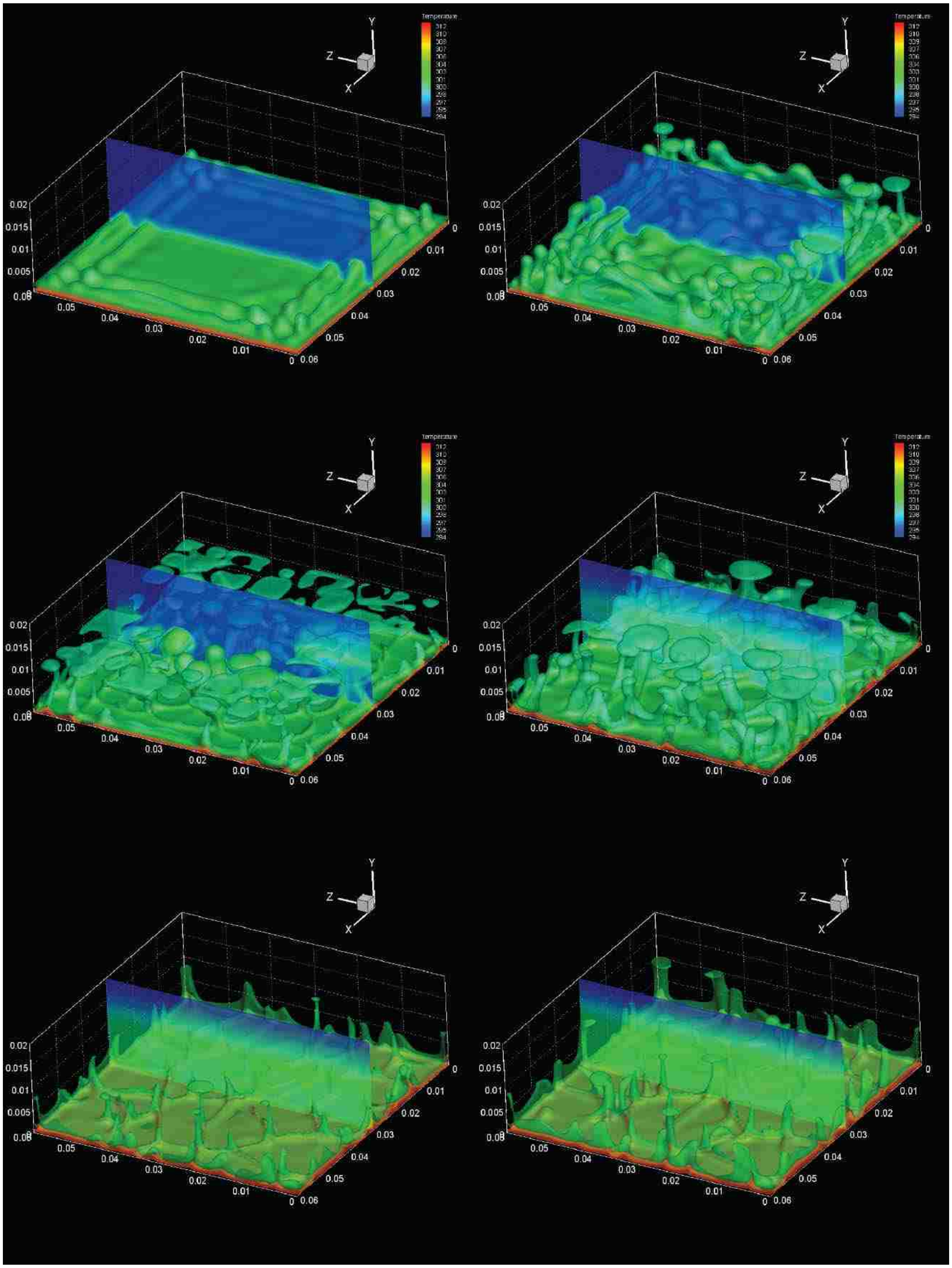

Figure 47 Temperature isosurfaces for 3D air-water system at t = 15, 16, 18, 27, 32, 36 second.

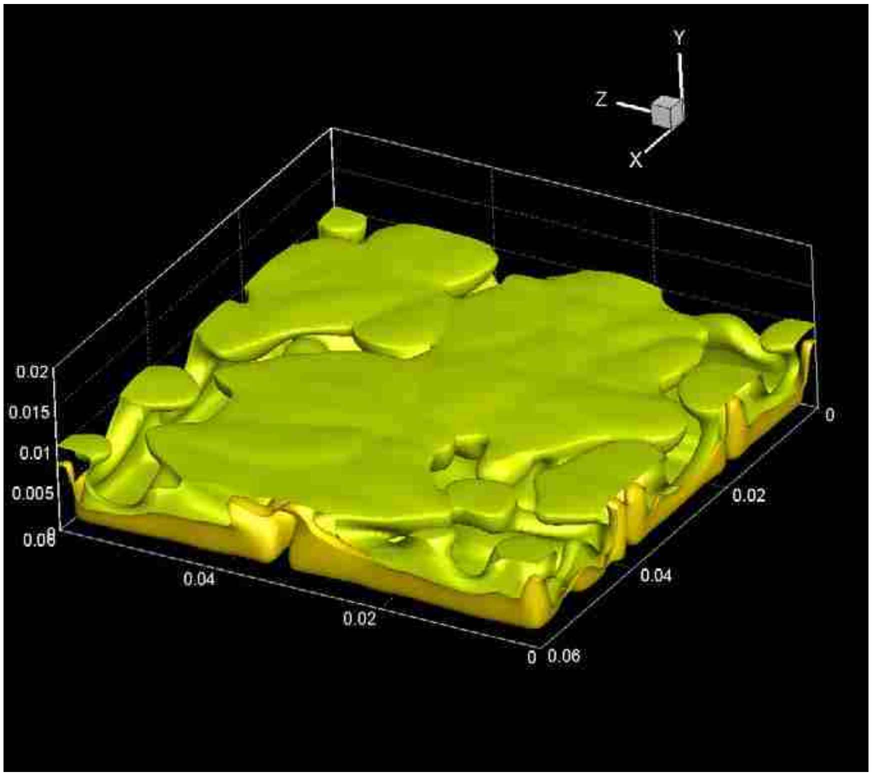

Figure 48 Temperature isosurfaces for 3D air-water system at t = 83 second.

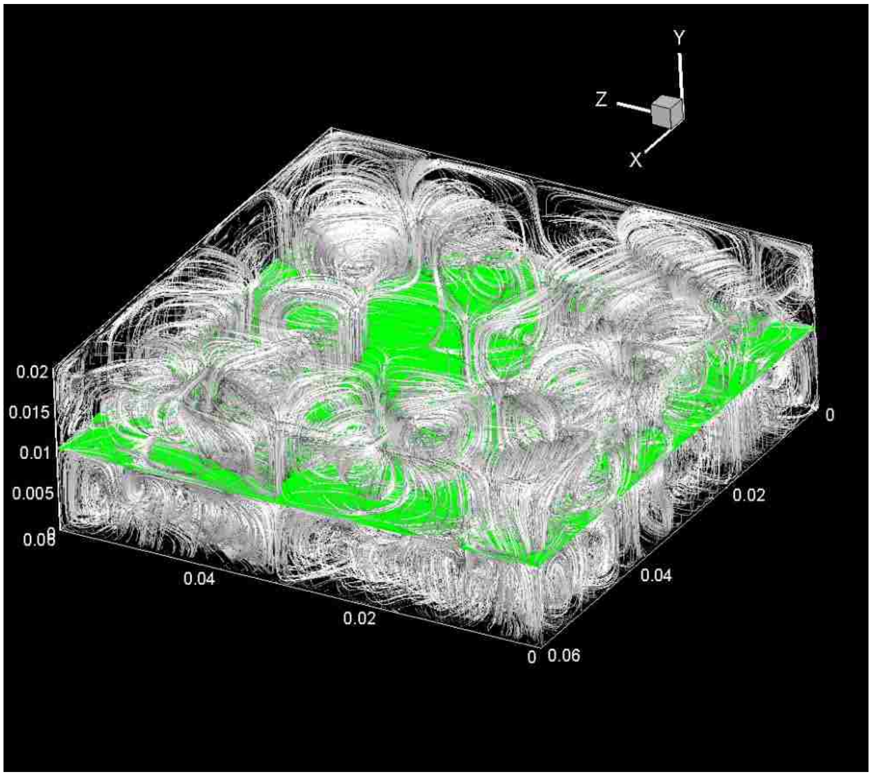

Figure 49 3D instantaneous streamlines for air-water system at t = 83 second

Chapter 5

Conclusion

We introduced the 5th order WENO Level Set Direct Numerical Simulation solver in this work to accurately predict the flow behavior of multiple incompressible fluids. The tracking of the interface is accomplished without to find the front explicitly. The numerical diffusion is controlled within a finite constant thickness $O(h)$. The smoothness of the level set function is guaranteed by reinitialization throughout the solving process. This algorithm is coded with staggered spatial discretization, which reduced the odd-even decoupling problem in traditional collocated method. 4th order Runge-Kutta method is also used to help stabilize the time stepping process. The implicit interface tracking technique handles the merging and breaking-up easily and no added method is required to make this happen. The surface tension is incorporated as a source term by using the CSF model and can be easy to compute. The validation of this method is carried out by comparing the result obtained from ANSYS Fluent in simulating a rising gas bubble. And good agreements are found between our method and Fluent quantitively and qualitatively. The movement and mechanism for 2D bubbles, drops and multiple bubble-merging are studied by using the method presented in this work. The method is further extended to simulate a binary Rayleigh-Bénard convecting system by coupling the energy equation. Multiple numerical experiments are carried out in two and three-dimensional geometries. The classic plume structures are captured in two-dimensional and three dimensional geometries. The dynamics and flow behavior of the binary Rayleigh-Bénard convecting system are discussed. The 2D results are also compared with linear stability analysis and shows the system would go unstable for any wave number as along as the Rayleigh number exceeded the critical value. The competition between the buoyancy and thermal diffusion effects is clearly depicted by the 2D results. The 2D Bénard cells are skewed and compressed when the cells approach the lateral walls. With the geometry expanded into the third direction, the plume structure started with a thin neck and expanded spanwisely in all directions at a later time. The raised 3D plume structures quickly entangled and merged together under the effect of thermal diffusion. The presence of orthogonal lateral walls in three dimensional geometry shows the rivalry of the wall effects from the diagonal aligned cells.

5.1 Future work

Numerical study on Marangoni Bénard convection under microgravity

The surface tension effect was not included in simulating the binary Rayleigh-Bénard convecting system. Under normal gravity, the magnitude of Marangoni force is negligible. However, the surface tension force may severely affect the interface or even dominate the flow with reduced gravitational forces under the micro gravity environment. Couple of recent experiments performed under the micro gravity environment show many interesting flow behavior. An experiment on a wickless heat pipe operated under the microgravity shows a fluid sustained by high Marangoni stress will condense rather than vaporize along the surface at 160 K which is about the boiling point [44]. Although many experiments have been performed and observed some unusual transport phenomenon, little numerical works are out there for the binary system or a multi-component system with more than two phases or components. One likely reason for not many numerical studies exist may be due to the complication of the interfacial characteristics. For the two layer Rayleigh-Bénard system, the interface is widely spanned initially. A small disturbance on the interface will lead to steep changes in curvature, which could cause serious numerical instabilities. A finer mesh may be utilized to alleviate the problem. However, the characteristics of multiphase Rayleigh-Bénard or Marangoni-Bénard convection indicates the chaotic dynamics are distributed across the whole domain and a global refinement of mesh might be necessary. The current SOR Poisson solver works fine with the present mesh resolution. However, the convergence will be slowed exponentially with the mesh elements increase in 3D. It is imperative to adapt a more efficient Poisson solver, like parallel SOR[45], which utilize a black/red ordering method to avoid the self-recursion, or flexible preconditioned conjugate gradients method [46–48]. The level set method may couple with the VOF method to reduce the bandwidth on the mass conservation [49,50]. It is expected that a method would be more accurate if more information were obtained from the simulation with a reasonable numerical stability and acceptable computational cost.

Reference

[1] Bénard, H., 1901, “Les Tourbillons Cellulaires Dans Une Nappe Liquide. - M{é}thodes Optiques D’observation et D’enregistrement,” J. Phys. Theor. Appl., **10**(1), pp. 254–266.

[2] Rayleigh, Lord, 1916, “On Convection Currents in a Horizontal Layer of Fluid, When the Higher Temperature Is on the under Side,” Philos. Mag. Ser. 6, **32**(192), pp. 529–546.

[3] Noh, W. F., and Woodward, P., 1976, “SLIC (Simple Line Interface Calculation),” *Proceedings of the Fifth International Conference on Numerical Methods in Fluid Dynamics*, A.I. van de Vooren, and P.J. Zandbergen, eds., Springer Berlin Heidelberg, Berlin, Heidelberg, pp. 330–340.

[4] Hirt, C. W., and Nichols, B. D., 1981, “Volume of Fluid (VOF) Method for the Dynamics of Free Boundaries,” J. Comput. Phys., **39**(1), pp. 201–225.

[5] Unverdi, S. O., and Tryggvason, G., 1992, “A Front-Tracking Method for Viscous, Incompressible, Multi-Fluid Flows,” J. Comput. Phys., **100**(1), pp. 25–37.

[6] Osher, S., and Sethian, J. A., 1988, “Fronts Propagating with Curvature-Dependent Speed: Algorithms Based on Hamilton-Jacobi Formulations,” J. Comput. Phys., **79**(1), pp. 12–49.

[7] Pearson, J. R. A., 1958, “On Convection Cells Induced by Surface Tension,” J. Fluid Mech., **4**(5), pp. 489–500.

[8] Cerisier, P., Jamond, C., Pantaloni, J., and Charmet, J.C., 1984, “Déformation de La Surface Libre En Convection de Bénard-Marangoni,” J. Phys. Fr., **45**(3), pp. 405–411.

[9] Zhong, J.-Q., Funfschilling, D., and Ahlers, G., 2009, “Enhanced Heat Transport by Turbulent Two-Phase Rayleigh-Bénard Convection,” Phys. Rev. Lett., **102**(12), p. 124501.

[10] ORESTA, P., FORNARELLI, F., and PROSPERETTI, A., 2014, “Multiphase Rayleigh-Bénard Convection,” Mech. Eng. Rev., **1**(1), p. FE0003-FE0003.

[11] Haghshenas, A., and Rahimian, M. H., 2015, “Simulation of Two-Phase Rayleigh-Benard Problem Using Lattice Boltzmann Method,” IARJSET, **2**(10), pp. 1–6.

[12] Fontana, É., Mancusi, E., Souza, A. A. U. De, and Souza, S. M. A. G. U., 2016, “Linear Stability Analysis and CFD Simulation of Double-Layer Rayleigh-Benard Convection,” Brazilian J. Chem. Eng., **33**(3), pp. 607–616.

[13] Chorin, A. J., 1967, “A Numerical Method for Solving Incompressible Viscous Flow Problems,” J. Comput. Phys., **2**(1), pp. 12–26.

[14] Sussman, M., Smereka, P., and Osher, S., 1994, “A Level Set Approach for Computing Solutions to Incompressible Two-Phase Flow,” J. Comput. Phys., **114**(1), pp. 146–159.

[15] Brackbill, J. ., Kothe, D. ., and Zemach, C., 1992, “A Continuum Method for Modeling Surface Tension,” J. Comput. Phys., **100**(2), pp. 335–354.

[16] Chang, Y. C., Hou, T. Y., Merriman, B., and Osher, S., 1996, “A Level Set Formulation of Eulerian Interface Capturing Methods for Incompressible Fluid Flows,” J. Comput. Phys., **124**(2), pp. 449–464.

[17] Hartmann, D., Meinke, M., and Schröder, W., 2010, “The Constrained Reinitialization Equation for Level Set Methods,” J. Comput. Phys., **229**(5), pp. 1514–1535.

[18] Zhao, H.-K., Chan, T., Merriman, B., and Osher, S., 1996, “A Variational Level Set Approach to Multiphase Motion,” J. Comput. Phys., **127**(1), pp. 179–195.

[19] Adalsteinsson, D., and Sethian, J. A., 1995, “A Fast Level Set Method for Propagating Interfaces,” J. Comput. Phys., **118**(2), pp. 269–277.

[20] Shu, C.-W., 1997, “Essentially Non-Oscillatory and Weighted Essentially Non-Oscillatory Schemes for Hyperbolic Conservation Laws,” ICASE Rep., (97–65), pp. 1–78.

[21] Jiang, G.-S., and Peng, D., 2000, “Weighted ENO Schemes for Hamilton--Jacobi Equations,” SIAM J. Sci. Comput., **21**(6), pp. 2126–2143.

[22] Shu, C., 2003, “High-Order Finite Difference and Finite Volume WENO Schemes and Discontinuous Galerkin Methods for CFD,” Int. J. Comut. Fluid Dyn., **17**(2), pp. 107–118.

[23] Lafaurie, B., Nardone, C., Scardovelli, R., Zaleski, S., and Zanetti, G., 1994, “Modelling Merging and Fragmentation in Multiphase Flows with SURFER,” J. Comput. Phys., **113**(1), pp. 134–147.

[24] Scardovelli, R., and Zaleski, S., 1999, “Direct Numerical Simulation of Free-Surface and Interfacial Flow,” Annu. Rev. Fluid Mech., **31**, pp. 567–603.

[25] Harvie, D. J. E., Davidson, M. R., and Rudman, M., 2006, “An Analysis of Parasitic Current Generation in Volume of Fluid Simulations,” Appl. Math. Model., **30**(10), pp. 1056–1066.

[26] Vincent, S., and Caltagirone, J., 2004, “Test-Case No 10: Parasitic Currents

Induced by Surface Tension (PC),” Multiph. Sci. …, **0**(10), pp. 2–7.

[27] Meland, R., Gran, I. R., Olsen, R., and Munkejord, S. T., 2007, “Reduction of Parasitic Currents in Level-Set Calculations with a Consistent Discretization of the Surface-Tension Force for the CSF Model,” 16th Australas. Fluid Mech. Conf., (December), pp. 862–865.

[28] Renardy, Y., and Renardy, M., 2002, “PROST: A Parabolic Reconstruction of Surface Tension for the Volume-of-Fluid Method,” J. Comput. Phys., **183**(2), pp. 400–421.

[29] Meier, M., Yadigaroglu, G., and Smith, B. L., 2002, “A Novel Technique for Including Surface Tension in PLIC-VOF Methods,” Eur. J. Mech. B/Fluids, **21**(1), pp. 61–73.

[30] Jamet, D., Torres, D., and Brackbill, J. U., 2002, “On the Theory and Computation of Surface Tension: The Elimination of Parasitic Currents through Energy Conservation in the Second-Gradient Method,” J. Comput. Phys., **182**, pp. 262–276.

[31] Lörstad, D., and Fuchs, L., 2004, “High-Order Surface Tension VOF-Model for 3D Bubble Flows with High Density Ratio,” J. Comput. Phys., **200**(1), pp. 153–176.

[32] Pellew, A., and Southwell, R. V., 1940, “On Maintained Convective Motion in a Fluid Heated from below,” Proc. R. Soc. A Math. Phys. Eng. Sci., **176**(966), pp. 312–343.

[33] Gumerman, R. J., and Homsy, G. M., 1974, “Convective Instabilities in Concurrent Two Phase Flow: Part I. Linear Stability,” AIChE J., **20**(5), pp. 981–988.

[34] Richter, F. M., and Johnson, C. E., 1974, “Stability of a Chemically Layered Mantle,” J. Geophys. Res., **79**(11), pp. 1635–1639.

[35] Cserepes, L., and Rabinowicz, M., 1985, “Gravity and Convection in a Two-Layer Mantle,” Earth Planet. Sci. Lett., **76**(1–2), pp. 193–207.

[36] Busse, F. H., 1981, “On the Aspect Ratios of Two-Layer Mantle Convection,” Phys. Earth Planet. Inter., **24**(4), pp. 320–324.

[37] Andereck, C. D., Colovas, P. W., Degen, M. M., and Renardy, Y. Y., 1998, “Instabilities in Two Layer Rayleigh–Bénard Convection: Overview and Outlook,” Int. J. Eng. Sci., **36**(12–14), pp. 1451–1470.

[38] Luijkx, J. M., Platten, J. K., and Legros, J. C., 1982, “Precise Measurements of the Wavelength at the Onset of Rayleigh-Benard Convection in a Long Rectangular

Duct," Int. J. Heat Mass Transf., **25**(8), pp. 1252–1254.

[39] Cross, M. C., Hohenberg, P. C., and Safran, S. A., 1982, "Wave Number Selection in Rayleigh-Bénard Convection: A Numerical Study," Phys. D Nonlinear Phenom., **5**(1), pp. 75–82.

[40] Mukutmoni, D., and Yang, K. T., 1992, "Wavenumber Selection for Rayleigh—Bénard Convection in a Small Aspect Ratio Box," Int. J. Heat Mass Transf., **35**(9), pp. 2145–2159.

[41] Duggin, M. J., 1969, "The Thermal Conductivity of Liquid Gallium," Phys. Lett. A, **29**(8), pp. 470–471.

[42] Spells, K. E., 1936, "The Determination of the Viscosity of Liquid Gallium over an Extended Nrange of Temperature," Proc. Phys. Soc., **48**(2), pp. 299–311.

[43] Assael, M. J., Armyra, I. J., Brillo, J., Stankus, S. V., Wu, J., and Wakeham, W. A., 2012, "Reference Data for the Density and Viscosity of Liquid Cadmium, Cobalt, Gallium, Indium, Mercury, Silicon, Thallium, and Zinc," J. Phys. Chem. Ref. Data, **41**(3), p. 33101.

[44] Kundan, A., Nguyen, T. T. T., Plawsky, J. L., Wayner, P. C., Chao, D. F., and Sicker, R. J., 2017, "Condensation on Highly Superheated Surfaces: Unstable Thin Films in a Wickless Heat Pipe," Phys. Rev. Lett., **118**(9), p. 94501.

[45] Evans, D. J., 1984, "Parallel S.O.R. Iterative Methods," Parallel Comput., **1**(1), pp. 3–18.

[46] Notay, Y., 2000, "Flexible Conjugate Gradients," SIAM J. Sci. Comput., **22**(4), pp. 1444–1460.

[47] Bridson, R., and Greif, C., 2006, "A Multipreconditioned Conjugate Gradient Algorithm," SIAM J. Matrix Anal. Appl., **27**(4), pp. 1056–1068.

[48] Davey, K., and Ward, M. J., 2000, "A Successive Preconditioned Conjugate Gradient Method for the Minimization of Quadratic and Nonlinear Functions," Appl. Numer. Math., **35**(2), pp. 129–156.

[49] Yamamoto, T., Okano, Y., and Dost, S., 2017, "Validation of the S-CLSVOF Method with the Density-Scaled Balanced Continuum Surface Force Model in Multiphase Systems Coupled with Thermocapillary Flows," Int. J. Numer. Methods Fluids, **83**(3), pp. 223–244.

[50] Griebel, M., and Klitz, M., 2017, "CLSVOF as a Fast and Mass-Conserving Extension of the Level-Set Method for the Simulation of Two-Phase Flow Problems," Numer. Heat Transf. Part B Fundam., **71**(1), pp. 1–36.

VITA

Haolin Ma was born on Saturday, June 21, 1986 in Qingzhou, Shandong, The People's Republic of China. His father is Jianwei Ma and mother Dongying Ma. Haolin attended the No. 1 High School of Qingzhou wehre his passion for math and science got excited. He played trombone and was the leader of the school's marching band. He graduated from high school in May of 2004.

Haolin enrolled at Shandong University of Technology (SDUT) in September of 2005 and received his Bachelor of Science in Mechanical Engineering degree in July 2009 with a 3.5 grade point average. He was active with his department's English debate team and led the team to the championship of 1st SDUT English Debate Contest. Haolin was granted the university thesis award by his research on design and control of parallel robots. In August 2009, he participated the 6th Shandong Province Students Electromechanical Product Innovation Design Competition and received the first prize.

In August 2010, Haolin enrolled at Lehigh University in Bethlehem, Pennsylvania. There, he met his advisor Dr. Alparslan Oztekin and worked on multiple research projects, including Mechano-Biologically Informed Molecular Models of Flow Sensitive Biopolymers, Portable Micro-Hydroturbine Power System and Novel Heat Exchanger Design and Analysis. He was awarded a Master of Science in Mechanical Engineering degree in January 2013 with a 3.68 grade point average. Haolin started working on his dissertation research on Level set method in multiphase flow in 2015 and successfully defended his dissertation and graduated with the degree of Doctor of Philosophy in Mechanical Engineering in May 2017.